Motion Sensitivity in Center-Surround Receptive Fields of Primate Retinal Ganglion Cells

Todd R Appleby

A dissertation

submitted in partial fulfillment of the

requirements for the degree of

Doctor of Philosophy

University of Washington

2024

Reading Committee:

Michael B Manookin, Co-Chair

Fred Rieke, Co-Chair

Greg Horwitz

John Tuthill

Program Authorized to Offer Degree:

Neuroscience

University of Washington

Abstract

Motion Sensitivity in Center-Surround Receptive Fields of Primate Retinal Ganglion Cells

Todd R Appleby

Co-chairs of the Supervisory Committee:

Michael B Manookin
Department of Ophthalmology

Fred Rieke
Department of Physiology and Biophysics

Primate visual perception is built on the 20-25 parallel pathways in the retina that carry information of the visual world to the rest of the brain. Each parallel pathway is represented by a unique type of primate retinal ganglion cell, the outputs of which are formed by a collection of upstream retinal circuits. While each primate retinal ganglion cell type maintains its own unique function, all retinal ganglion cells share a common receptive field structure: an excitatory center enveloped by a suppressive surround. The center-surround receptive field functions to enhance spatial structures likes edges, and in some ganglion cell types contributes to the encoding of color and temporally modulated inputs. Visual motion is well studied across many cortical and subcortical regions of the primate visual system, but our knowledge of how visual motion affects encoding properties of retinal ganglion cells is limited. This thesis aims to characterize visual motion sensitivity in a subset of primate retinal ganglion cell types from the perspective of the classical center-surround receptive field. Our results fall along two major themes. First, that the receptive field centers of

some ganglion cell types are far more sensitive to motion of approaching objects than receding objects (Chapter 2). Second, in some ganglion cell types, the presence of motion in the receptive field surround shifts the center-surround relationship from antagonistic to facilitatory (Chapter 3 and 4). Our work suggests that neural inputs to primate retinal ganglion cells are activated dynamically as visual contexts shift, particularly for contexts that involve visual motion. Overall, we demonstrate that the primate retina has the computational complexity required for motion sensitivity that was previously considered to be present only in the primate cortex.

Acknowledgements

Finishing a PhD means leaving a trail of strange problems that could not have been overcome without the help and support of many. First on the list is my family. I am incredibly lucky to have unconditional support from my parents, Mike and Sheryl, and brother, Scott. The PhD was easier knowing I'd always have my family in my corner. Also, I know my late grandmother wanted so badly to see me or my brother graduate, and while that did not happen, her support during the PhD was unwavering. I am grateful to have been able to share my experiences of grad school with her for as long as I did.

Thanks to everyone in the lab – you know who you are. I want to specifically thank Adree, Nori, and Shellee for their direct help on some of my projects. A big thanks to Michelle Gianmarco for her patience and willingness to help with access to the confocal microscope at SLU! Also, my advisors, Mike and Fred, have been an incredible pair from which to learn and grow as a scientist. I am grateful that they were so committed to working together with me throughout the last 7 years.

Shoutout to the 2017 and 2018 cohorts! I'd like to specifically reference Sneha, Su-Yee, Jordan, Lili, Alainna, Ellen, Nastacia, Kristen, and Sierra who I got a chance to know a little better than the others. Particularly Ellen and Su-Yee who I shared an office with for 6 years, and also Adree and Raveena who shared years with us in the office. Nobody mentions how critical it is to sit next to people you like during your PhD. I got lucky in that regard.

I'd also like to note my appreciation for those who reached out in real ways during the pandemic. That includes Adree, Alainna, and others. Important to note here are my European friends: Louisa, Emily, Tan, and Melanie. I couldn't have made it through the PhD without having friends outside of Seattle to whom I could whine about how things were going here!

Lastly, thanks to the professors who were integral in getting me to the PhD in the first place.

There are many to name, but specifically Ray Kesner, Keith Sillar, Ayako Yamaguchi, and Greg Schwartz. Ray Kesner's Brain, Behavior, and Society course at the University of Utah kick-started my interest in neuroscience. Keith Sillar kindled my interest in isolated neural circuits through the study of *Xenopus* motor neurons, and Ayako Yamaguchi taught me single cell patch electrophysiology so I could study *Xenopus* motor circuits in more depth. Ayako's willingness to teach me whole cell patch physiology is what ultimately propelled me to a spot in a great PhD program, and I can't thank her enough for it! Last, but certainly not least, is Greg Schwartz who introduced me to the retina and the wonderful world of ganglion cell typing, where I still reside, scientifically speaking, today! I've been incredibly lucky to have great mentors in my scientific career so far! Thank you all.

Contents

List of Figures

Chapter 1

Introduction

Photoreceptors transduce energy from photons that contain spatial, temporal, and spectral information about the visual world into electrochemical signals that are the basis of nearly all visual perception [1, 2]. Visual signals are passed from the photoreceptors through a mesh of converging and diverging retinal circuits [3], becoming increasingly abstracted from their original form. In the rhesus macaque monkey retina, the visual inputs of about 3.1 million cones [4] are sent through around 1.5 million axons [5] in the optic nerve of a single eye. Visual signals from more than 10 cones can converge before reaching the macaque retina's optic nerve [6], representing a pre-processing and consolidation of visual information into pathways necessary for cortical reconstruction of the visual world. Convergence of visual signals through the retina necessitates a reconciliation between the loss of visual fidelity and the maintenance of perceptual richness. The primate retina's answer to this problem lies in its $\sim$20 output pathways, each represented as a type of retinal ganglion cell (RGC), that transmit parallel streams of visual input from the neural circuits of the retina to the rest of the brain ([7, 8]). What aspects of the visual world are encoded in each retinal ganglion cell's output, and how does each ganglion cell pathway curate visual inputs in order to select its outputs? These are the overarching questions that motivate the work of this thesis.

For over 100 years, encoding properties of sensory neurons have been characterized by their receptive fields, which measure the extent over which sensory input is captured [9]. Retinal ganglion cell receptive fields are classically described over a spatial extent, where changes in light intensity

over a circumscribed area change the spiking output of the cell. Across species, retinal ganglion cell receptive fields share a ubiquitous structure where luminance contrast across a center region of space increases spiking output of the neuron, while matching contrast in an area surrounding the center suppresses spiking output. The antagonistic center-surround structure of retinal ganglion cell receptive fields was established early in the 1960s in primate [10–12], and even earlier in non-primate retina [13]. One proposed function of surround suppression is to emphasize spatial edges [14, 15], a critical part of identifying object boundaries in natural scenes.

In order for the surround suppression to emphasize edges, an RGC need only be sensitive to the relative distribution of light contrast across the center and surround. Alone, center-surround antagonism provides a framework for describing RGCs as edge detectors with preferred spatial scales across types. Experimental evidence suggests that this is not the case. Primate RGC receptive field centers are sensitive to spatial contrast without input from the receptive field surround [16, 17]. Moreover, the surround plays a role in tuning sensitivity of the receptive field center to contrast [18]. Therefore, the center-surround receptive field structure plays a role in spatial encoding, but that role is not limited to classical edge detection. Center-surround function, then, shifts as spatial stimuli become more complex.

Stimulus complexity is not limited to variations in black and white spatial contrast. Visual inputs also contain information about color, depth, and motion. In primate RGCs, center-surround receptive field function also extends to the color domain. A majority of midget ganglion cells are selectively activated by either green or red input into its receptive field center and are non-selective to color inputs to its surround, granting the cell chromatic opponency [19, 20]. In this case, the center dominates color functionality, whereas the surround is achromatic but still spatially antagonistic. It is unknown whether other RGC types have receptive field centers that are selectively activated by color or other visual inputs beyond spatial contrast. Moreover, the extent to which RGC receptive field surrounds show stimulus-specific sensitivity in primate retina is unknown.

Type-specific stimulus selectivity is informed by the larger visual function that each ganglion

cell effectuates, but tying low-level inputs from the retina to the complexity of visual perception is difficult–even for the best studied RGC types. Early studies of the relationship between RGC type and visual function relied on the overabundance of retinal outputs to the lateral geniculate nucleus (LGN), where primate RGC projections are separated by type into magnocellular and parvocellular layers [21]. Visual deficits in primates after lesion of magnocellular LGN include loss of most, but not all, motion perception and flicker perception, while parvocellular LGN lesions cause a loss of color vision, depth, and texture perception [22, 23]. Given the major deficits in motion perception when magnocellular pathways are lesioned, RGCs that project to magnocellular LGN may be more likely to carry motion information. How this bears out at the level of magnocellular- and parvocellular-projecting RGC receptive fields in terms of motion sensitivity is an ongoing area of study, and a central theme of this thesis.

Sensitivity of primate RGCs to motion has largely focused on the parasol RGC type, which projects to the magnocellular LGN [24]. The receptive field center of the parasol RGC has been found to be more sensitive to motion inputs than non-motion inputs [25], and population studies suggest that parasol RGCs respond with high temporal precision as an object moves from one parasol RGC receptive field to the next [26, 27]. The magnocellular pathway also contains projections from another RGC type: the smooth monostratified cell [28]. Motion sensitivity in smooth monostratified RGCs has not been shown. Recently, the broad thorny ganglion cell type, which projects to the koniocellular LGN, an area situated between the parvo- and magnocellular LGN regions, has been found to be particularly sensitive to motion stimuli presented simultaneously to its receptive field center and surround [29, 30]. The role of the center-surround receptive field in motion sensitivity in these cell types, or others, is unclear. Moreover, the breadth of motion sensitivity in the receptive field center across RGC types, and whether the receptive field surround is sensitive to motion in any RGC type, is also unknown.

In terms of the classical center-surround receptive field, any stimulus encoded by the surround modulates the encoding of receptive field center input. Therefore, sensitivity to motion by the

surround is not necessarily linked to motion encoding, but rather motion modulates the RGC's output–which may or may not contain motion information. Conversely, an RGC's receptive field surround could be non-selective for motion, but the RGC could still encode motion through motion sensitivity of the receptive field center. Therefore, questions about the role of the classical center-surround in motion processing are two pronged. One, does the RGC encode motion in its output? This is a central question of **Chapter 2**, which characterizes receptive field center sensitivity in a subset of RGCs to observer-induced motion. **Chapter 3** explores selectivity of specific motion types by RGCs through an interaction of receptive field center and surround. Second, how does a motion-sensitive surround affect signal integration in the receptive field center? **Chapter 3** also looks at receptive field surround sensitivity to motion in a subset of primate RGCs, and tests how surround motion sensitivity affects RGC output. Finally, **Chapter 4** details how the midget RGC's receptive field surround affects input sensitivity of the center in the context of eye movements.

1.1 Retinal architecture

1.1.1 Structure of the RGC Center-Surround Receptive Field

The RGC receptive fields that transform visual inputs into spiking outputs rely on a relatively simple organization of perpendicularly oriented neural circuits. Phototransduction in the photoreceptors begins a vertical relay of visual signals through the excitatory bipolar cells to the ganglion cells, where action potentials (spikes) are generated and ultimately propagated down axons through the optic nerve. Lateral to the receptive field's vertical circuitry lies a set of inhibitory interneurons that shape the spiking outputs of ganglion cells. These inhibitory neurons come in two broad types: horizontal cells and amacrine cells. Horizontal cells act at the photoreceptor-to-bipolar cell synapse, while the amacrine cells work in the inner layers of the retina, most commonly at the level of the ganglion cell and associated pre-synaptic circuitry [31–33]. The columnar and lateral

arrangement of retinal circuitry creates a radial receptive field, where excitation at the RGC corresponds to a center locus of photoreceptors and inhibition corresponds to a surrounding field of photoreceptors.

The spatial extent of an RGC's dendrites describes the diameter over which the receptive field center extends. Dendritic extent is RGC-type specific, but also grows as a function of distance from the fovea [7]. Indeed, much of conscious perception corresponds to visual input from the fovea, a small area in the temporal region of the retina with tightly packed ganglion cells [34]. Recordings in this thesis are made from peripheral RGCs, whose receptive fields are wider than their foveal counterparts and receive a higher number of converging inputs from upstream circuits [10, 6]. Each retinal neuron type evenly tiles space, from the fovea to the far periphery, allowing complete coverage of visual input across the eye to each retinal cell type regardless of receptive field size [35].

Connectivity in the retina, and in the nervous system at large, is not limited to classical chemical transmission where a synaptic cleft forms between a projecting neuron's axonal bouton and a receiving neuron's dendrite. Neurons can also directly link via gap junctions, which are close connections between adjacent cell bodies. Gap junctional connections are created by combinations of the protein connexin, which form hemichannels from each neuron that join together into a gap junctional pore [36]. Gap junctional connections between neurons are made up of many pores, ultimately allowing the quick spread of visual signals as electrical current between neurons [37]. Anatomical evidence of electrical coupling between bipolar cells exists in primate retina [38–40]. Electrical coupling of neurons by gap junctions in the primate retina has been suggested to increase the size of the bipolar cell receptive field by lateral spread of visual input [41]. Evidence suggests that visual signals through bipolar gap junctions may enhance the spread of spatio-temporally correlated stimuli, increasing RGC spiking output to stimuli like motion, which contain strong space-time correlations [42, 25]. Gap junctional spread of signals between ganglion cells, particularly the parasol types, has also been suggested via an intermediary amacrine cell [43, 44].

1.1.2 Bipolar cells

The retinal bipolar cells constitute the only connection between the outer layer of the retina, the domain of the photoreceptors and horizontal cells, with the inner retina, where amacrine and ganglion cells reside. In primate, there are $\sim$12 types of bipolar cell that respond to either Onset or Offset of light [45, 46]. Each primate retinal bipolar cell has its own center-surround receptive field structure [41]. While direct recordings from primate bipolar cells are scarce, non-primate bipolar cell pathways have been characterized by the specific spatial, temporal, and spectral properties of the visual input that they project to amacrine and ganglion cells [47, 48]. Between RGC pathways, spatial density and cell-type input of bipolar cells contributes to pathway specialization. For example, bipolar cell input to the On smooth monostratified cell is more spatially hetereogenous across the cell's dendrites than in the On parasol, but the On parasol receives inputs from a more diverse set of bipolar cell types [49].

Bipolar cell outputs are highly rectified. Rectification limits signal transfer to changes in light contrast that match the bipolar cell's On or Off type, though the extent of rectification changes between On and Off types and depends on ambient light level [50–52]. Rectified signal transfer from bipolar cells causes ganglion cells to receive uni-polar input relative to stimulus contrast. Consequently, a ganglion cell receiving input from only On bipolar cells (an On-type ganglion cell) will spike if half of the ganglion cell receptive field's spatial extent is covered by an increase in light contrast, while the other half is covered by a corresponding decrease. A spatially linear ganglion cell presented with the same visual pattern would have the signals from the two halves subtracted, resulting in no spiking output. Non-linear spatial summation has been well established in both primate and non-primate retinal ganglion cells. The scale of each summed nonlinear unit within the receptive field center often matches the width of bipolar cell receptive fields, while the strength of nonlinear summation across ganglion cell types changes based on the extent of bipolar cell rectification [28, 53–55, 17].

1.1.3 Amacrine cells

Amacrine cells are a diverse set of retinal interneurons, broadly separated into narrow- and wide-field types according to the spatial extent of their processes (reviewed in [33]). Inhibition from amacrine cells is received by both ganglion cells and bipolar cells, often described as post-synaptic (at the level of the ganglion cell) or pre-synaptic (at the level of the bipolar cell) inhibition. Amacrine cells do not send their processes to the optic nerve, however some types of amacrine cells project axon-like processes across large extents (>4mm) of the retina [56, 57].

Molecular and morphological characterizations of amacrine cells in primate suggest anywhere from 25 to 35 unique types [58, 8]. Each retinal ganglion cell circuit receives its own unique cocktail of amacrine cell type connectivity, indicating that amacrine cells likely play a large role in shaping functional outputs in each retinal ganglion cell pathway [59–61]. Functional characterizations of primate amacrine cells are very limited. Still, two types of primate amacrine cells have been shown to be potentially motion sensitive, though it is unknown how motion sensitive amacrine cells might contribute to motion encoding in RGCs [62, 63].

An example of functional amacrine cell diversity is seen in salamander retina, where two wide-field amacrine cells are selectively activated by two very different stimuli. A GABAergic wide-field amacrine cell encodes mean luminance and affects surround size of RGCs [64]. The stimulus that produces effective signaling of a glycinergic wide field poly-axonal amacrine type is dramatically different. Effective inhibition by this amacrine type requires spatio-temporal contrasts apparent in moving stimuli, and the inhibition generated by motion shows differing suppressive effects between ganglion cell types [65]. In another salamander retina example, gap-junctioned somas of a single type reside across the dendritic extent of a corresponding RGC, creating motion sensitivity in the amacrine cell population that is transferred through inhibitory neurotransmitters to the RGC [66, 67].

The circuit motifs that govern amacrine cell function are often described by their site of action.

Feedforward inhibition is characterized by input from a bipolar cell to both an amacrine cell and ganglion cell, where the amacrine cell supplies inhibition to the same ganglion cell. This type of inhibition can modulate the temporal dynamics of the ganglion cell output, including those involved in sensitivity to approaching objects [68, 69]. Feedback inhibition supplies inhibition to the bipolar cell (or another amacrine cell). Feedback and feedforward motifs work together to maintain sensitivity of the retinal circuitry involved in nighttime vision [70]. Crossover inhibition supplies inhibition from the On pathway to the Off, and vice versa. This type of inhibition has many functions, including altering the linearity of a ganglion cell's input-output relationship and changing the temporal patterning of RGC output [71, 16]. Serial inhibition puts multiple amacrine cells in sequence, ultimately causing a decrease in inhibition either at the ganglion cell or the bipolar cell. Functional consequences include increased sensitivity across background luminance levels and increased effective inhibition for motion-sensitive cells in mouse ([72, 73]).

1.2 Adaptation in the Retina

The visual inputs encoded by RGC pathways are not monolithic in terms of the qualities that describe those inputs. For example, an edge enhanced by a center-surround receptive field may be brilliantly illuminated or barely perceptible, subtly different than the mean luminance of a background or highly variable, textured, and/or presented at discreet time points across short or wide intervals. As a tangible example, consider the moon. Lunar irradiance shifts around 3 fold from a lunar phase of 10 degrees to 60 degrees, changing the intensity of light reflecting off the world over the span of 5 days [74]. Imagine a retinal pathway equipped with complex circuitry designed to extract relative object depths, but this machinery reaches complete saturation in terms of its output with just a two-fold shift in the moon's brightness. (i.e. $\sim$4 days of a 2 week lunar cycle). This limited operating range might say something interesting about a visual species from an ethological perspective, but for most diurnal species (or even nocturnal, in this case), a moonlight-particular

pathway is incredibly inefficient.

In actuality, RGCs adapt to their time-varying inputs. Classical adaptation refers to an inverse relationship between the strength of the input and sensory neuron sensitivity, where the dynamic operating range of a neuron is shifted to avoid saturation to widely varying inputs [75]. Operating range of a sensory neuron refers to the relationship between intensity or strength of input and magnitude of the output response. Adaptation changes this input-output relationship, but does not necessarily shift the nature of the selected inputs encoded by a visual pathway. Adaptation in a sensory neuron is often characterized best by a change in gain where the slope of the input-output relationship changes, increasing or decreasing output to a given amount of input. Sensory neurons can also change their output threshold, adjusting the amount of input required to begin generating an output. Gain and threshold changes are used throughout the nervous system to ensure efficiency of information transfer [76].

Critical to the function of adaptation are the timescales over which input-output functions shift. Rapid shifts in stimulus statistics require a fast rate of adaptation in order to avoid immediate saturation. Rapid shifts in input intensity are common in a visual scene, like when an observer moves their gaze from the ground to the sky. However, adaptational mechanisms can also shift sensitivity over a longer term, to tune an input-output relationship for a new visual context (like a change in environment, from an open field to a dense forest). Indeed, contrast adaptation in the retina occurs on fast (<100ms) and slow (several seconds) timescales, across bipolar cells, ganglion cells, and amacrine cells [77–81]. Moreover, sometimes adaptation timescales themselves can adapt to the frequency with which input statistics change [82].

The retinal circuitry responsible for adaptation to the contrast distribution and mean luminance in a visual scene have been reasonably well characterized–particularly in non-primate retina. Fast contrast adaptation prevents saturation after a rapid shift in contrast variance, and can occur in as little as 10ms [77–79]. Retinal ganglion cells contain an intrinsic mechanism for adaptation of spike generation through sodium-channel inactivation, induced by changing the variance of

injected current with and without sodium channels blocked [78]. Isolation of specific mechanisms in non-ganglion cell retinal neurons has been done via recording a ganglion cell's synaptic current inputs. In this way, excitatory and inhibitory input to the ganglion cell have been shown to adapt, indicating potential adaptation mechanisms within both bipolar cells and amacrine cells [77–79]. Notably, the outer retina seems to play a larger role in mean luminance adaptation than contrast adaptation, though evidence for contrast adaptation in excitatory inputs to salamander bipolar cells has been shown [77, 78, 83].

Fast and slow contrast adaptation occur simultaneously. The duration of slow adaptation runs anywhere from 4 to 20 seconds [84, 72]. Slow contrast adaptation generally occurs following a change from high to low contrast, where sensitivity to low contrast inputs takes time to recover from the high contrast regime. This type of adaptation dulls the output of RGCs by putting them in a hyperpolarized state that, in guinea pig, lasted 6.2 seconds on average ([80]). The mechanism of recovery following adaptation to a high contrast stimulus has been attributed to bipolar cell output, as determined by an increase in adaptation magnitude when the spatial scale of the input stimulus matches the size of the bipolar cell receptive field ([80]). Onset of high variance contrast can also cause adaptation at longer timescales, although reported duration varies between 1 and several seconds [77, 78, 80].

In the primate retina, contrast adaptation has been found in the dominant inputs to the magnocellular pathway, the On and Off parasol cells [85–87]. Contrast adaptation in the parasol cell is best elicited following a high temporal frequency grating [85, 88]. The mechanism for contrast adaptation in parasol ganglion cells seems to be located in the cell's receptive field surround ([88]). Curiously, the On and Off midget ganglion cell of the parvocelluar pathway show little to no adaptation to a moving grating of high contrast [85, 87], but both midget and parasol cells show adaptation to noise stimuli delivered to their receptive field centers [89]. **Chapter 3** and **Chapter 4** of this thesis tests the ability of primate RGC surrounds to induce adaptation during motion and other spatio-temporally modulated stimuli.

1.2.1 Neural Sensitization

Adaptation maintains RGC sensitivity after a shift in the visual input from low to high contrast. However, the hyperpolarization period following the shift renders the cell insensitive to subtle contrasts [80]. Separate from adapting RGCs are sensitizing RGCs, which have been found in mouse, rabbit, zebrafish, and salamander retina [90, 91]. Sensitizing RGCs show an opposite reaction to strong stimulus input where they increase their output rather than decrease it like in classically adapting cells. As a consequence, sensitizing RGCs are still able to respond to subtle contrasts following a change from high to low contrast conditions [90, 92, 91]. Together, pairs of adapting and sensitizing like-type RGCs transmit information from visual scenes more reliably than RGCs that only adapt [90].

A sensitization mechanism has been found in salamander RGC receptive field surrounds, where a decrease in tonic inhibition is required to elicit sensitization [92, 93]. The center receptive field can show classical adaptation even when the surround sensitizes [92]. No such sensitization mechanism has been insofar found in the primate retina. Sensitization of primate RGC output via stimulation of the receptive field surround is explored in depth in **Chapter3** and **Chapter 4**.

1.3 Modeling the RGC Receptive Field & Its Outputs

Retinal neurons encode visual scenes into spike trains transmitted through the optic nerve, with stable and repeatable stimulus-to-response transformations. These transformations can be described mathematically, in part by using linear algebra to compare matrices of visual inputs and response outputs, like contrast and spike rate, while also utilizing exponential, rectifying, or other more complex functions to represent nonlinear steps in the transformation. Mathematical operations like these provide a way of modeling the relationship between visual stimuli and neuronal responses, giving a framework for investigating mechanisms of neural circuits when live experimentation is

difficult or impractical.

In each chapter of this thesis, receptive field models are used to describe mechanisms by which visual motion affects neural output of an RGC type. The models that best capture the dynamics of moving inputs depend on the nature of the inputs. For example, the motion in the receptive field surround might be best represented by a dynamic modulation of bipolar cell input to the receptive field center. Alternatively, motion sensitivity by the receptive field center alone will require interactions between bipolar cells, amacrine cells via crossover inhibition, or dendrites of a ganglion cell over space and time. Choosing the appropriate model is dependent on stimuli used and question asked. An ideal model is generalizable enough to capture multi-modal visual inputs, while also capturing an element of biological structure that re-creates RGC output, ultimately describing a novel and meaningful role for biological mechanisms in visual encoding. The strengths and weaknesses of models commonly used in visual neuroscience are outlined below.

1.3.1 Classical Models - Difference of Gaussians

In simplest form, an On or Off RGC receptive field can be modeled as its two dimensional extent, where stimulus pixels located within that extent are weighed against their contrast values and ultimately summed into a model output. A model such as this extracts information about the polarity of the input (positive or negative relative to a mean light level, on average) and the size of the input, but nothing else. And yet this simple model is a classical sensory neuron motif, often represented mathematically by subtracting a pair of two dimensional gaussians of inverted polarity [94–96].

The difference of gaussians (DoG) model is attractive in part because the model requires only a few parameters (a shared mean and separate values for standard deviation and amplitude) that are easily measured experimentally. Modeled in two dimensions (length and width), the surround gaussian, larger in standard deviation and smaller in amplitude, in effect circumscribes the center similar to the center-surround structure of an RGC receptive field. The opposite sign of the DoG's

surround gaussian relative to the center gaussian applies inhibition to the center, suppressing model output. Depending on the properties of the input stimulus, the surround's inhibitory actions on the center can be reasonably modeled by the DoG as a linear process [10, 97, 53]. However, in reality, the receptive field surround's effect on signal integration and output of the receptive field center is often not linear, as demonstrated by Kuffler's early recordings in the frog retina [13, 53].

The DoG's inability to capture nonlinear receptive field components is a major shortcoming for modeling RGC receptive fields. Nonlinearities in the retinal circuitry appear at many levels, and they are key in curating the unique outputs of an RGC pathway [98]. Bipolar cell rectification and nonlinear input-output structure are two pivotal nonlinearities not captured by a DoG model. Moreover, the ganglion cell itself has built-in nonlinearities that don't change across cell types: a spike rate that can't reach below 0 and an upper bounded spike rate informed by the spiking refractory period (1 to 2 ms). Ultimately, beyond a general center-surround receptive field shape, the DoG model offers minimal representation of the neural circuits mechanisms that makeup an RGC pathway.

1.3.2 Classical Models - Linear/Nonlinear

The linear-nonlinear (LN) model is comprised of a linear front end followed by an output nonlinearity [99]. The output nonlinearity of an RGC is generally half-wave rectified, with the non-rectified wave modeled well by a sigmoid (that is, a curve with threshold and saturation points). The linear portion of the LN model consists of a Gaussian representation representation of the receptive field's spatial extent and a temporal filter, generated by the kinetics of an RGC's output response to a stimulus. LN models can be used with On-Off RGCs when spatial and temporal components of both pathways are the same, as the output nonlinearity can map positive and negative activation values of its temporal filter.

The temporal element of the LN model is helpful for modeling adaptation states [78, 79, 100]. However, a single adaptation state changes the filter and/or the nonlinearity [78, 79], so the predic-

tive power of the LN model is reduced when a stimulus with a wide range of statistics is used. Still, in terms of describing how the kinetics or input-output properties change when RGCs adapt, the LN model is a useful tool [89]. Moreover, multiple LN models can be added in series to model the timescale of adaptation across different cell types [90]. **Chapters 3 and 4** use LN models to compare how static and non-static inputs to the receptive field surround affect input-output properties of RGCs.

So far, the models described integrate stimuli linearly over space. Predicting outputs to scenes with an abundance of spatial contrast is problematic for an LN model with a single temporal filter and output nonlinearity [17, 101]. Adding multiple spatial subunits that match the receptive field properties (in space and time) of rectified bipolar cells increases predictive power to naturalistic (i.e. spatially heterogeneous) inputs [102, 17]. Interestingly, adding subunits across the center and surround with appropriate temporal filters for each bipolar cell and amacrine cell subunit is enough to generate motion sensitivity based on comparisons of object speed as it passes through the center and surround of a salamander RGC [66].

Chapter 2 of this thesis investigates RGC sensitivity to dilating motion in the receptive field center alone. Bipolar cells do not have any known intrinsic motion sensitivity in the primate retina. However, when their outputs become correlated via gap junctions, they can contribute to motion sensitivity [42, 25]. Crossover inhibition can also be generated from stimulation of the receptive field center. Crossover inhibition does play a role in temporal processing of spatially heterogeneous inputs to primate RGCs [16], though no clear role in motion sensitivity has been shown.

1.4 Motion in the Primate Visual System

Characterization of motion sensitivity in the primate retina has largely been focused on the suitability of a population of On and Off parasols to encode moving visual inputs. In these studies, the temporal precision of parasol RGC population responses to moving stimuli make them well-suited

to encode the speed and direction of motion [26, 27]. A more recent study suggests that each parasol RGC, as a function of its excitatory presynaptic input, is motion sensitive across a range of speeds, though direction tuning has not been shown [25].

Beyond the primate retina, motion encoding by primate cortical neurons is well documented. Areas of primate cortex that contain visual motion sensitive neurons include the superior colliculus [103–105], middle temporal area of extrastriate cortex (area MT) [106], area V1 [107–109], and inferior pulvinar [110]. Moreover, magnocellular LGN has been suggested as a primary input pathway to motion areas described in the dorsal stream (largely V1 and area MT) of the primate visual system [111–114].

RGCs in primate retina project, even among single types, to combinations of these areas [115]. The On and Off parasol ganglion cells, for example, send direct projections to magnocellular LGN and superior colliculus [24, 116, 117, 28]. The information sent by an RGC to multiple areas of the primate brain must be low-level enough to suit functions across both brain areas. However, functional properties of, for example, V1 and superior colliculus, may overlap. In this case, the visual system may prefer RGC input containing motion information so as not to overlap motion computations across brain areas. The extent to which the primate visual system balances the complexity of its retinal inputs, from a single cell and population perspective, against the needs of each cortical and subcortical visual area is unknown. Some evidence of a mixed case is seen in the mouse visual system, where motion sensitivity arises de novo in many area V1 neurons, but a subpopulation of V1 neurons rely on motion sensitivity encoded directly by the retina [118].

Because motion processing in the primate retina must subserve the functions of the primate visual system at large, it's important to understand the types of motion encountered by the retina and the motion types encoded by downstream cortical areas. In the following subsections, I briefly outline each.

1.4.1 Eye Movements

The eyes of many species, including humans, are constantly moving during visual perception, including during periods of visual fixation [119]. Fixational eye movements are continuous, with low amplitude movement trajectories that are often described as a tremor, which in aggregate can drift the eye over 10s of microns (the length of several cone photoreceptor receptive fields) [120]. Classical studies suggest that fixational eye movements help keep the visual system from adapting out repetitive inputs [121, 122]. More recent work has shown that fixational eye movements play a role in humans' ability to discriminate high spatial frequency patterns [123, 120]. In turtle retina, fixational eye movements drive synchronous firing in RGCs, providing more robust estimates of visual input to the cortex [124]. How fixational eye movements might affect visual encoding by primate RGCs is currently unknown.

A separate type of eye movement is a saccade. Saccades are ballistic eye movements that move the eye around a visual scene between bouts of visual fixation. The fixational interval between saccadic eye movements can lie anywhere from 100 to 300 ms, though in some cases intervals can be longer or shorter [125]. Generally, saccades bring the fovea of the eye towards regions of interest in the visual scene, which can be driven consciously by goal-driven visual behavior.

In **Chapter 3** we test how ganglion cells respond to stimuli that have trajectories that mimic the tremor of fixational eye movements. **Chapter 4** looks at how saccadic eye movements affect encoding of natural scenes.

1.4.2 Object and Global Motion

As a primate moves through its environment, the visual world moves globally across the primate's retina. Compensatory eye movements help combat observer motion in terms of keeping the eyes tracked on a fixation point [126]. However, compensatory eye movements do not counteract the complex flow fields that are created by objects moving around the eye's foveating point during

observer-induced global motion. Indeed, when a primate walks forward without rotating its head or eye, a dilation of the visual world occurs. When translation and rotation by movement of the eye, head, and body simultaneously, optic flow vortexes and shears, creating complex percepts that can shift rapidly during naturalistic movement [127, 128]. The information contained within optic flow fields is important for survival of the animal. For example, the speed and trajectory information within optic flow patterns is used by primates in order to intercept and avoid objets [129, 130].

The primate visual system encodes many varieties of global motion across cortical and subcortical areas, including optic flow. Neurons in the medial temporal area (area MT) respond well to global motion translation in a particular direction [131]. Neurons in the dorsal region of the medial superior temporal (MST) area of primate cortex are selective for translating or vortexing motion across particular areas of the visual scene [132]. Area V3a also contains neurons sensitive to a combination of optic flow pattern and visual scene location [133]. Critical elements of optic flow are the expansion and outward movement of objects. **Chapter 2** compares responses of RGCs to stimuli that expand over time (approaching motion) to stimuli that recede, testing whether the primate retina shows sensitivity to stimuli that are similar to the dilating motion that occurs as primates move through their environment.

Object motion refers to any type of visual motion not generated by the observer. Object motion encoding is prevalent across the primate visual system. Classic studies in Area V1 show that neurons encode the direction of moving objects [134]. It is also critical for an animal to separate object motion from background motion. Many neurons in area MT of primate cortex encode the differential motion of an object in their receptive field center relative to background motion in their receptive field surround [131, 135, 136]. **Chapter 3** shows a primate RGC type with similar selectivity for differential motion between center and surround.

1.5 RGC Pathways in Primate and Non-Primate: What do we know?

A handful of primate RGC types have spatial, temporal, and chromatic characterizations, all within the framework of the classical antagonistic center-surround receptive field [115, 137]. On and Off parasol and On and Off midget RGCs are the most well studied of all primate RGCs, owing to their overwhelming representation in terms of density in the primate retina [117]. Both midget and parasol cells have high flicker fusion rates, with parasols increasing their temporal frequency sensitivity with retinal eccentricity [138]. Parasol RGCs have been found to be somewhat more spatially nonlinear than the midget [55]. The midget encodes red vs green color inputs, while the parasol is achromatic [22]. As previously mentioned, parasols have been implicated in motion perception, largely (but not completely) from a population encoding perspective [26, 27, 25].

Compared to the parasol and midget ganglion cell types, other RGC types are sparsely expressed. The next-most abundant RGC type, at about 8% of the overall primate RGC volume, are the small-bistratified type ([7]). The small bistratified type is a blue vs yellow color opponent RGC, with blue and yellow receptive field centers that are somewhat co-extensive ([139]). The small bistratified cells project to the koniocellular LGN ([117] [29]). Another blue vs yellow color opponent primate RGC is the more sparsely expressed large bistratified cell, which projects to koniocellular LGN and superior colliculus ([117] [29])). Receptive field and functional properties of this cell are yet to be determined.

Beyond the small bistratified cell, three distinct subtypes of the sparsely expressed RGC types have been physiologically characterized in terms of their receptive field structure. These are the broad thorny and On and Off smooth monostratified ganglion cells [55, 28, 30, 140]. The smooth monostratified ganglion cells show very spatially nonlinear receptive fields, particularly compared to parasols [55, 140]. Dendrites of On and Off smooth monostratified RGCs have active properties,

and their receptive field centers have spatially non-uniform spiking outputs and bipolar cell inputs [140, 49].

Broad thorny ganglion cells respond at both increments and decrements of contrast, making it an On-Off cell type, and both On and Off outputs are heavily suppressed by a distinctly strong receptive field surround [30]. The broad thorny ganglion cell shows interesting response properties during motion, where a moving full field plaid (that is, a simple texture that spans both center and surround) completely suppresses response output. Other cell types, including the Off parasol, respond well to this stimulus [30]. Broad thorny RGCs have uniquely slow linear filters and a high sensitivity to objects moving through their center field centers [30]. Motion sensitivity of the broad thorny and On smooth monostratified cells are explored in **Chapters 2 and 3**.

10-15 other RGC types exist, known by their distinct morphologies, but a majority of them have little to no physiological or functional description [24, 97, 117, 29].

Non-primate RGCs have well established pathways for direction selectivity, orientation selectivity, and object motion sensitivity, among other complex output pathways [32]. A notable pathway in the non-primate retina that ties together center-surround interaction with motion sensitivty are the object motion sensitive RGCs found in salamander, rabbit, and mouse [66, 141]. These cells use an amacrine-cell mediated mechanism to select for motion speed differences between center and surround [66, 67]. In **Chapter 3**, we test for center-surround interactions that promote object motion sensitivity using stimuli similar to those used to characterize non-primate object motion sensitive RGCs.

Chapter 2

Selectivity to approaching motion in retinal inputs to the dorsal visual pathway.

The study presented in this chapter has been published as: Todd R. Appleby and Michael B. Manookin (2020). Selectivity to approaching motion in retinal inputs to the dorsal visual pathway. *eLife* Feb 24:9:e51144

2.1 Summary

To efficiently navigate through the environment and avoid potential threats, an animal must quickly detect the motion of approaching objects. Current models of primate vision place the origins of this complex computation in the visual cortex. Here, we report that detection of approaching motion begins in the retina. Several ganglion cell types, the retinal output neurons, show selectivity to approaching motion. Synaptic current recordings from these cells further reveal that this preference for approaching motion arises in the interplay between presynaptic excitatory and inhibitory circuit elements. These findings demonstrate how excitatory and inhibitory circuits interact to mediate an ethologically relevant neural function. Moreover, the elementary computations that detect approaching motion begin early in the visual stream of primates

2.2 Introduction

As an object approaches, the image of that object becomes larger on the surface of an observer's retina. Many animals use these size changes to estimate whether and when an object will collide with the animal [142–144] and also to estimate the animal's own motion through the environment [145, 146]. Neurons with such selectivity for approaching motion have been found in the dorsal visual pathway of primates [147, 148, 109]. However, it is not known whether similar approach selectivity is found earlier in the visual pathway of primates.

Several ganglion cell types found in the retinas of humans and non-human primates project to the dorsal visual pathway, including parasol (magnocellular-projecting) cells [149]. These cells can detect small changes in the reflectance of an object relative to the background (i.e. contrast), and their high contrast sensitivity has resulted in the hypothesis that these cells contribute primarily to representations of object form [150, 151]. Less is known about how motion affects the response properties of these cells [26, 27, 25].

Here, we report that parasol and other ganglion cell types in the macaque monkey retina display a preference for approaching motion. We show that visual circuits downstream of parasol cells can detect approaching motion based solely on the spike output of these cells. We further study the synaptic basis for this computation using direct recordings and a computational model. In summary, the elementary computations for detecting approach are present in the retinal input to the dorsal visual pathway of primates.

2.3 Results

We recorded the spike responses of five ganglion cell types—broad thorny, On and Off smooth monostratified, and On and Off parasol ganglion cells—in an in vitro preparation of the macaque monkey retina to determine whether these cells showed preference for approaching or receding

motion. Cells were identified based on their characteristic cell body sizes and shapes under infrared illumination, their distinct light response properties, and dendritic morphologies [30, 152, 28, 140, 55]. We begin by demonstrating that these cells show strong selectivity for approaching textures.

2.3.1 Five primate ganglion cell types show preference for approaching textures

Humans and non-human primates use changes in spatial scale or object size in estimating the speed of approaching objects and their own motion through the environment [142–146]. Further, this selec- tivity for approaching motion is commonly thought to originate in the thalamus or visual cortex of primates [109], and a retinal origin for this type of motion sensitivity has not been considered.

To determine whether ganglion cells in the primate retina exhibited a preference for approaching motion, we recorded cellular responses to moving stochastic textures (see Materials and methods). The spatial scale of the textures changed as a function of time—increasing in scale to simulate approaching motion or decreasing in scale to simulate receding motion. Further, both stimulus clas- ses contained the same ranges of images scales—the receding motion stimuli were simply the time- reversed image sequences of the approaching stimuli (Figure 2.1B; [146, 109]) Further, we tested the same range of scale changes that have been shown to elicit percepts of approaching motion in humans [146].

As shown in Figure 1, approaching textures elicited larger spike responses than receding textures in parasol, smooth monostratified, and broad thorny (On-Off type) ganglion cells. A large bistratified ganglion cell–another type of On-Off cell—also showed increased spiking to approaching textures, but the bias to approaching motion was not as strong as that observed in the other cell types (Figure 2.1A, bottom). This finding indicated that preference for approaching motion was not a universal property of all primate ganglion cells, but was restricted to a subset of these cell

types.

We quantified the degree to which a cell preferred approaching or receding motion by calculating the difference between the spike responses to approaching (Rapproaching) and receding (Rreceding) motion divided by the sum of those responses, as described by Equation 2.1.

$$approach\ \ selectivity = \frac{R_{approaching} - R_{receding}}{R_{approaching} + R_{receding}} \tag{2.1}$$

Positive values indicate a preference for approaching motion and negative values for receding motion while values near zero indicate a lack of preference. Indeed, the approaching textures elicited higher spike rates in On- and Off-type parasol and smooth monostratified ganglion cells, resulting in significant approach selectivity values in all four cell types (Figure 2.1c; $p<7.8 \times 10^{-3}$; Wilcoxon signed rank test).

The smallest texture scales used in these experiments corresponded in size to the dendritic tree diameters of the diffuse bipolar cells that provide excitatory synaptic input to parasol and smooth monostratified ganglion cells in the mid-peripheral retina ($\sim$30–40 mm) [153, 154, 45, 46, 17]. However, to reliably contribute to vision, these mechanisms must operate across the broad range of spatial scales encountered in the natural environment [155, 156]. To ensure that approach selectivity was not restricted to a limited subset of texture scales (i.e. spatial frequencies), we repeated the texture experiments using four distinct scale ranges in the same cell. The smallest scales in the texture sequences ranged from the approximate width of diffuse bipolar cells (3.3 cycles/degree) to the approximate dendritic tree width of parasol ganglion cells in the mid-peripheral macaque retina (0.8 cycles/degree).

Varying the scale ranges of the texture sequences did not change the preference for approaching textures. Approach selectivity persisted in parasol and smooth monostratified cells across these stimulus conditions (parasol: n = 16 cells, $p<2.4 \times 10^{-4}$; smooth monostratified: n = 7 cells, $p<7.8 \times 10^{-4}$; Wilcoxon signed rank test). In fact, approach selectivity increased with increasing texture

scale (i.e. decreasing spatial frequency) in both parasol and smooth monostratified cells (Figure 2.2D). These results indicated that the mechanisms mediating approach selectivity in these . cells operate across awide range of spatial scales. Further, the texture stimuli contained similar statistical properties to the types of motion encountered during optical flow, indicating that signals from parasol and smooth monostratified cells could be utilized in detecting this type of motion.

2.3.2 Approach motion selectivity predicted from nonlinear subunits

Neurons in macaque visual cortex show a preference for approaching textures, which is thought to arise from the linear spatiotemporal receptive-field structure of these cells [109]. However, neural mechanisms operating much earlier in the visual pathway might also contribute to the observed preference for approaching motion.

We considered the excitatory synaptic output from retinal bipolar cells onto the dendrites of gan- glion cells as a strong candidate for contributing to this type of stimulus selectivity. The synaptic output of retinal bipolar cells is strongly rectified (nonlinear) [50, 157] and this rectification is critical for detecting certain types of visual motion [51, 67, 42, 25]. Thus, we used a combination of computational modeling and synaptic current recordings to determine whether bipolar cells contributed to approach selectivity in parasol and smooth monostratified cells.

We created subunit receptive-field models based on direct measurements of the spatiotemporal filtering properties and output nonlinearities of the diffuse bipolar cells that provide excitatory synaptic input to parasol and smooth monostratified ganglion cells in the macaque monkey retina. The spatial components of the model bipolar cell receptive fields were based on previous measurements of these cells [153, 154, 45, 17]. and the temporal filtering properties, electrical coupling, and output nonlinearities were based on our own direct measurements [25].

The receptive-field profile of ganglion cells was modeled as a difference-of-Gaussians in which the receptive-field center was opposed by a surround of opposite contrast polarity. This receptive-field profile set the weighting of subunit inputs to model ganglion cells. The sizes and strengths of

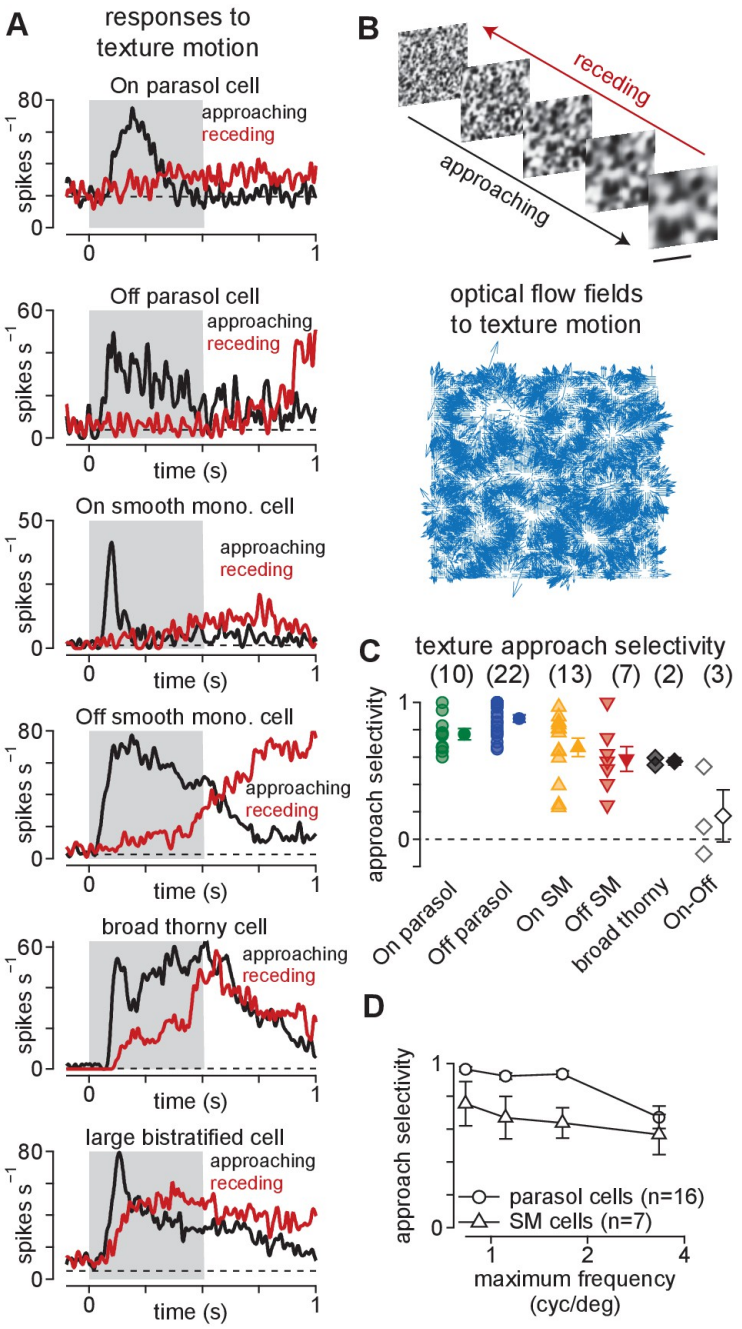

Figure 2.1: Ganglion cells exhibit a preference for approaching textures. (A) Responses of several ganglion cell types to receding (red) and approaching (black) Gaussian textures. Average spike rate is shown across 50–200 distinct randomly generated textures. The gray region indicates the period of motion. (B) Example of receding and approaching texture stimuli used in the experiments (top). Scale bar indicates 0.5 mm. Bottom, Optical flow fields computed from an example approaching texture movie. White areas show regions from which the texture expanded during the stimulus sequence. (C) Approach selectivity index values for cell types in (A) to the texture stimuli. Transparent shapes indicate individual cells. Opaque shapes and error bars indicate mean ± SEM. (D) Approach selectivity (y-axis) as a function of the initial spatial frequency (x-axis) in parasol (n = 16) and smooth monostratified ganglion cells (n = 7). Approach selectivity persisted at all spatial frequencies tested.

the center and surround regions of the receptive field were determined directly by measuring spike responses to sinusoidally modulated spots that varied in diameter (14–720 mm)—the relative sizes and strengths of center (w_c) and surround (w_s) regions of the receptive field were estimated from these response patterns (Figure 2.2B, C; see Materials and Methods).

Both center and surround regions were comprised of subunits and the surround provided lateral inhibition to the model ganglion cell with a temporal delay (see Materials and Methods). This delay occurs because surround inhibition typically arises via feedback from horizontal cells or amacrine cells and, thus, must traverse an extra synapse relative to the direct excitatory synaptic input from bipolar cells. We directly measured the surround delay by recording responses to spots presented over the receptive-field center or annuli presented in the surround. Spot or annulus contrast was drawn from a Gaussian distribution on each frame and the temporal filtering properties of center and surround regions were measured directly by cross-correlating the contrast trajectory of the stimulus with the cell's spike output (see Materials and Methods). The temporal delay between center and surround regions was determined from the difference in the time-to-peak of the temporal filters measured in the center and surround regions of the receptive field (Figure 2.2D, E). This delay was then incorporated into the model at the level of the surround subunits.

To determine whether the subunit models predicted the observed approach selectivity, we obtained the model outputs to moving textures. To simulate approaching or receding motion, the spatial frequency content (i.e. spatial scale) of the textures changed as a function of time [146, 109]. We compared two models that were identical except for the input-output function of the subunits—-in one case the function was linear and in the other it was nonlinear. The outputs of the linear subunit model were similar for both approaching and receding textures, resulting in a lack of approach selectivity ($p>0.4$ at all expansion rates; Figure 2.3A). However, the nonlinear subunit model showed a very different pattern—-approaching textures produced significantly larger outputs than receding textures for each expansion rate and this bias for approaching motion increased with increasing rate (Figure 2.3B). These modeling results suggest that the nonlinear output of

retinal bipolar cells may contribute to approach selectivity in some ganglion cell types.

These results are particularly important in the context of canonical models of motion sensitivity in primates. Previous studies posited that this type of approach selectivity arose in the cortex or thalamus [109]. Our physiological recordings, however, indicated that some primate ganglion cell types showed approach selectivity. Moreover, our modeling results indicated that approach sensitivity was predicted as a consequence of ganglion cells pooling across several nonlinear subunits. We will directly test the contribution of bipolar cells to approach motion selectivity later in this work, but first we examine whether retinorecipient brain regions could detect approaching motion from the outputs of parasol ganglion cells.

2.3.3 Circuit model predicts selectivity for approaching motion

Our physiological recordings indicated that individual parasol cells could distinguish between approaching or receding texture motion with a high degree of accuracy (Figure 1). We employed our computational models to gain insight into how accurately the direction of moving textures could be inferred by downstream neurons from the outputs of populations of On and Off parasol cells.

Each subclass of parasol ganglion cell (On or Off) forms a regularly spaced mosaic with neighboring cells of the same class, but the dendritic-field and receptive-field locations between On and Off types are uncorrelated [152, 139]. Thus, we randomly shifted the locations of the model On and Off cell mosaics relative to each other. We tested the model on 500 different textures moving at five different speeds (0.5–8 degrees s^{-1}). As with our direct recordings, the On and Off models showed larger responses for approaching textures relative to their receding counterparts (Figure 2.4B).

We tested linear and quadratic decoding models to estimate how accurately downstream neurons could distinguish between approaching and receding texture motion based on the outputs of the model On and Off parasol cells. The output of the linear decoding model was the scaled sum of the model parasol cell responses, and the quadratic model squared the outputs of these cells

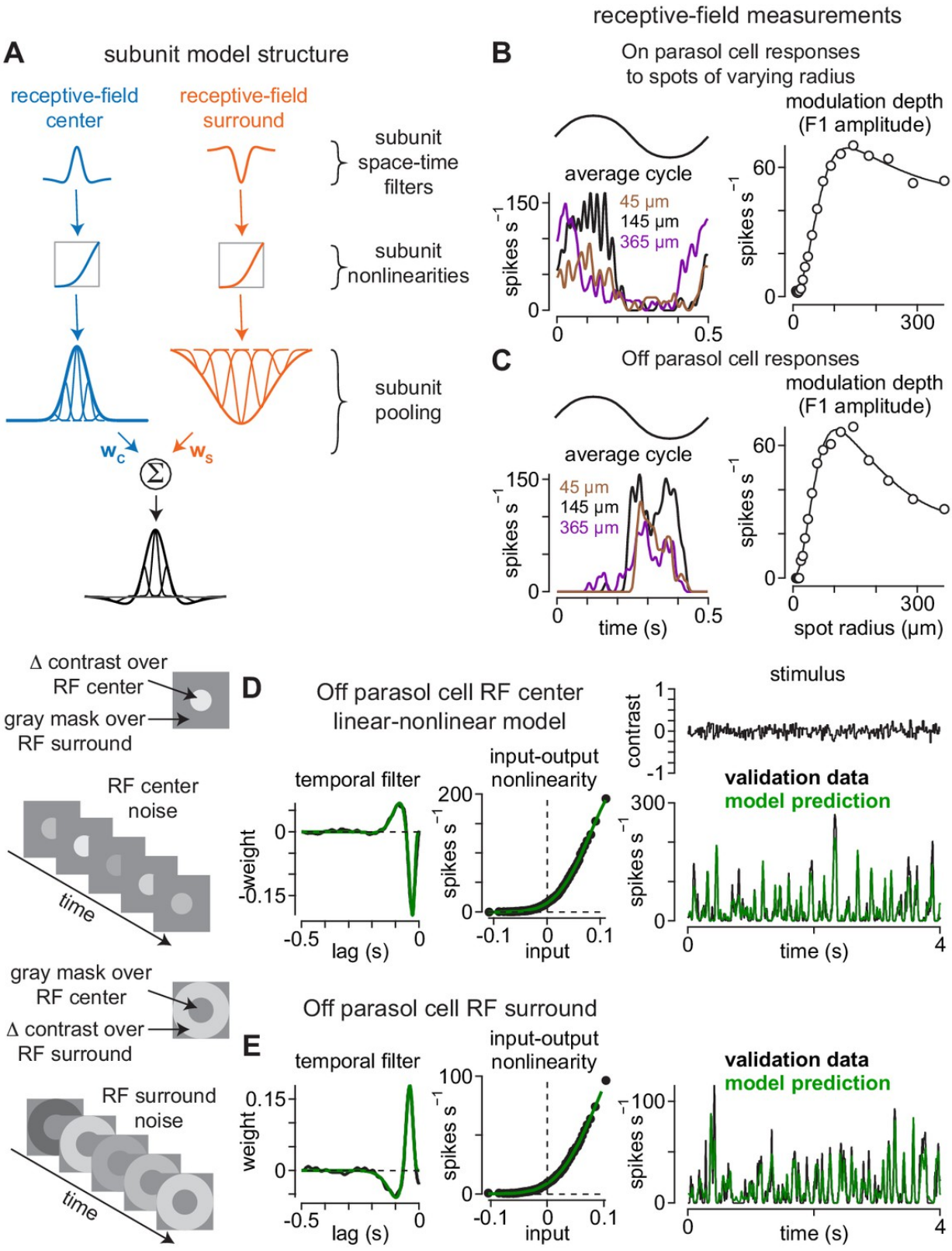
receptive-field measurements
A
subunit model structure
receptive-field center
receptive-field surround
subunit space-time filters
subunit nonlinearities
subunit pooling
w_c
w_s
Σ
B
On parasol cell responses to spots of varying radius
average cycle
45 µm
145 µm
365 µm
spikes s^{-1}
modulation depth (F1 amplitude)
C
Off parasol cell responses
time (s)
spot radius (µm)
Δ contrast over RF center
gray mask over RF surround
RF center noise
time
gray mask over RF center
Δ contrast over RF surround
RF surround noise
D
Off parasol cell RF center linear-nonlinear model
temporal filter
weight
lag (s)
input-output nonlinearity
input
stimulus
contrast
validation data
model prediction
E
Off parasol cell RF surround

Figure 2.2: Direct measurement of spatiotemporal receptive-field model parameters. (A) Model architecture. Center (left) and surround (right) regions of the receptive field were comprised of subunits. Subunits also exhibited center-surround receptive field structures based on published measurements. Following spatiotemporal filtering, signals were passed through a static input-output nonlinearity after which they were normalized and integrated at the level of model ganglion cells. (B) The sizes and weightings of center (w_c) and surround (w_s) inputs to the model ganglion cells in (A) were calculated by recording spike responses to spots presented over an On parasol ganglion cell's receptive field. Spot contrast (0.5) was modulated sinusiodally at 2 Hz and spot radius varied on each trial. The modulation depth (F1 amplitude) of the average cycle was largest at 145μ m (left) and fell off at smaller and larger radii (right). Solid line shows difference-of-Gaussians fit to the data (right). (C) Same as (B) for an Off parasol cell. (D–E) The temporal lag between center (D) and surround (E) regions of the receptive field was measured using a Gaussian flicker stimulus. On each frame, the contrast of either a spot (center condition) or annulus (surround condition) was drawn randomly from a Gaussian distribution with a mean of 0.0 and a standard deviation of 0.1. Temporal filters were determined by cross-correlating the cell's spike output with the stimulus sequence (left) and the temporal lag between center and surround was determined from the time-to-peak of these filters. Middle, Input-output nonlinearities were determined for the center and surround noise. Right, Unique contrast sequences were interleaved with repeated sequences. The repeated sequences were not used in computing the temporal filters, but were used to cross-validate the model. The average response to the repeated sequences (black) showed high correspondence to the model prediction (green).

prior to scaling and summation (see Materials and methods). We assessed the models' ability to distinguish between approaching and receding motion by calculating the Jensen-Shannon distance between the model outputs to these stimuli [158, 159]. This metric quantifies the degree of dissimilarity between the response distributions—values near zero indicate a high degree of similarity while values near one occur when the distributions are more distinct (see Materials and methods; Equation 17). Indeed, both decoding models showed Jensen-Shannon distance values $\geq$0.28 under all conditions and values near one at the higher speeds tested (Figure 2.4D, E). These results indicated that downstream circuits could accurately detect approaching motion with very simple processing of the inputs from On and Off parasol cells.

To determine whether decoding accuracy varied with the number of ganglion cell outputs, we calculated model performance while varying the number of On/Off output pairs (1–6 pairs). Pairings were established by calculating the nearest Euclidean distance between neighboring cells.

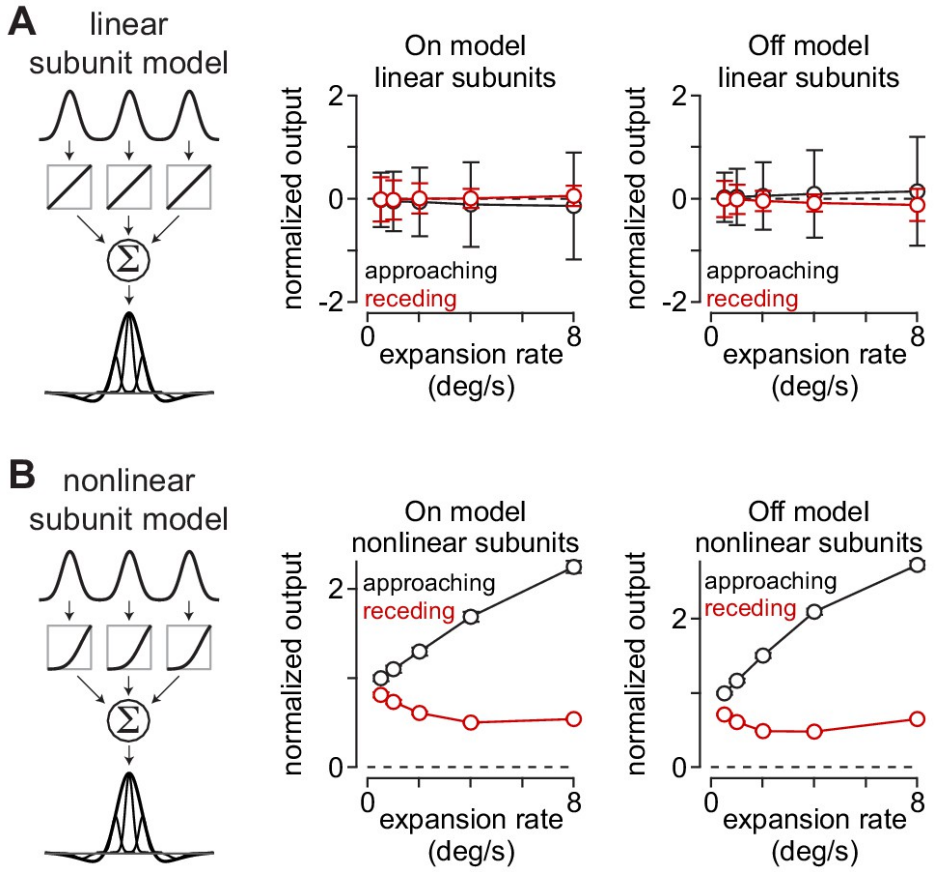

Figure 2.3: Approach selectivity to moving textures predicted from nonlinear receptive-field subunits. (A) Normalized outputs of linear subunit models to 500 textures that either approached or receded at five different rates. Approaching and receding motion was not distinguishable at any rate for either the On or the Off subunit models. (B) Outputs of models containing nonlinear subunits. Adding a nonlinearity at the model bipolar cell output produced selectivity for approaching textures at all expansion rates. Error bars indicate mean ± SEM

Increasing the number of model ganglion cell pairs providing input to the linear decoder produced a modest increase in performance (Figure 2.4D). The effect on the quadratic decoder was more varied—increasing the number of ganglion cells greatly improved performance at the slowest expansion rates, but the effects were inconsistent at faster expansion rates. These results are consistent with the premise that integrating over a larger number of retinal outputs improved performance in detecting approaching textures. However, model performance was high for single ganglion cell pairs, indicating that little integration or post-processing of the retinal output was

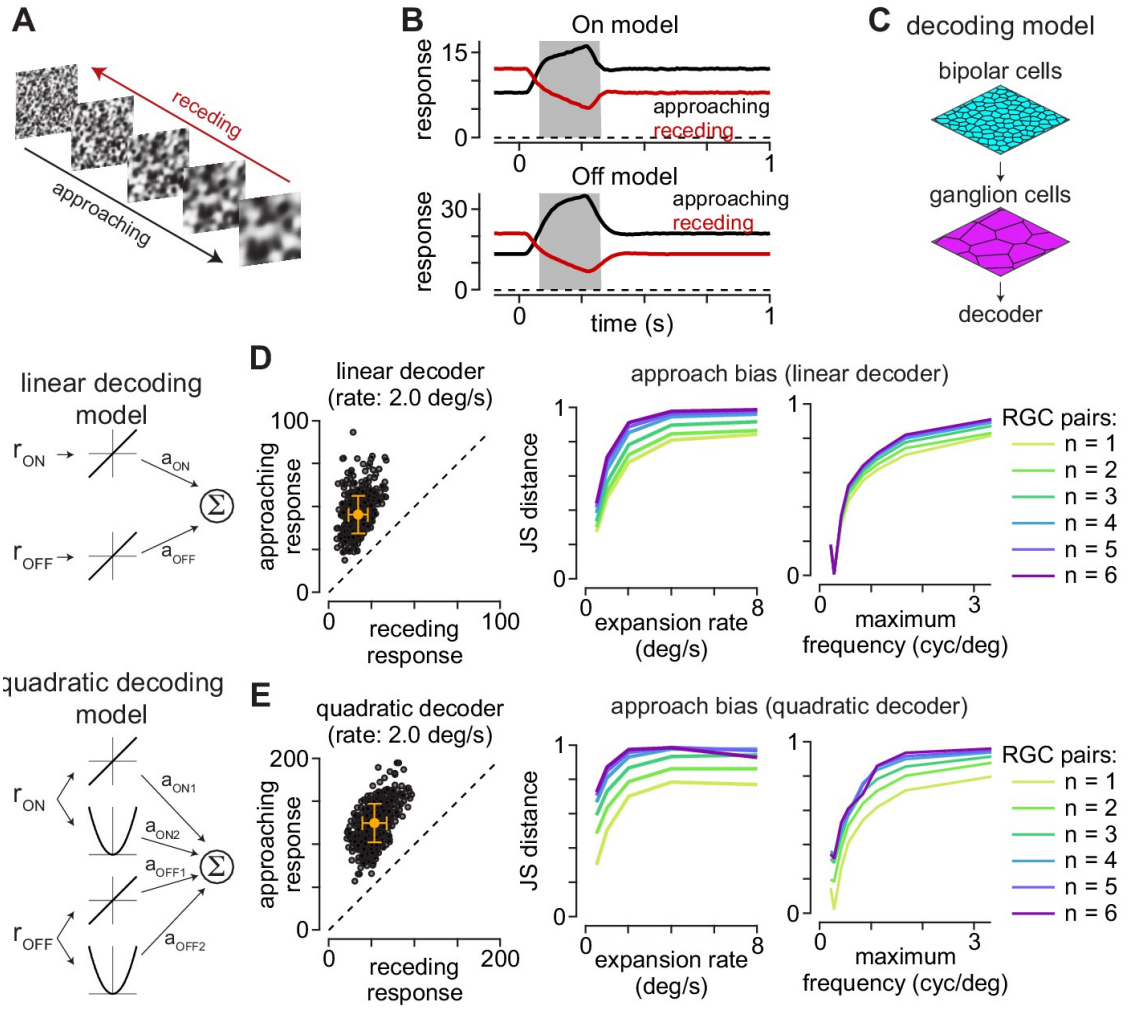

Figure 2.4: Computational model predicts selectivity for approaching textures. (A) Example approaching and receding textures. The same texture sequence was presented from highest-to-lowest spatial frequency (approaching) or lowest-to-highest spatial frequency (receding). Models were run on 500 unique texture sequences at five different expansion rates. (B) Average responses of On (top) and Off models (bottom) to 500 textures that approached or receded at 2.0 degree s^{-1}. (C) Basic organization of decoding models. Model bipolar cells provided input to ganglion cell mosaic which, in turn, provided input to the decoder. (D) The output of the linear decoding model was the weighted sum of the outputs from the On and Off models. The model produced larger outputs for approaching than receding motion for each of the textures, shown as individual circles (left). Jensen-Shannon distance values computed between the distributions for approaching and receding textures at five expansion rates (middle). This approach bias persisted across a range of expansion rates and was highest at higher rates. Lines are color coded for the number of ganglion cells combined by the decoder. Right, Jensen-Shannon distance (y-axis as function of the maximum spatial frequency in the moving textures (x-axis). Discriminability of the approaching textures persisted across a broad range of spatial frequencies and fell off when spatial frequency content was very low (<0.3 cycles degree–1). (E) Same as (D) for the quadratic decoding model.

required to reliably detect approaching motion.

The type of motion that we studied with the approaching and receding texture stimuli is commonly encountered as an animal moves through the environment [157, 156]. The results presented thus far in our study support the premise that the output of the primate retina contains reliable information that could be used by downstream neural pathways for detecting approaching motion. Our next goal was to understand the specific neural circuit mechanisms mediating the observed motion preference.

2.3.4 Approach motion selectivity present for moving annuli

The subunit model in Figure 3 demonstrated that the nonlinear input-output properties of bipolar cell subunits could account for much of the observed approach selectivity to texture motion. We next wanted to determine whether this output nonlinearity accounted for all the observed effect or whether other circuit mechanisms also contributed. We did this by designing a stimulus paradigm which should not elicit approach selectivity for the nonlinear subunit circuit motif described in Figure 2.3. Thus, if approach selectivity were observed, other circuit mechanisms must also contribute. The stimulus used was a ring (annulus) that expanded outwardly (approaching) or contracted inwardly (receding) along the dendritic tree (Figure 2.5A). Figure 2.5B illustrates the widest extent of the annulus relative to the receptive-field profiles of example On and Off parasol cells that were measured using the stimulus paradigm described in Figure 2.2. The annulus was contained within the receptive-field center, which allowed us to probe cellular and model response properties without strongly engaging the surround.

We tested the predictions of three model configurations on the approaching and receding annuli: (1) a model in which the subunit outputs were linear (linear subunit model), (2) a model in which the output of each subunit was passed through an output nonlinearity (nonlinear subunit model), and (3) a model in which simulated electrical coupling between subunits occurred prior to the output nonlinearity (coupled subunit model).

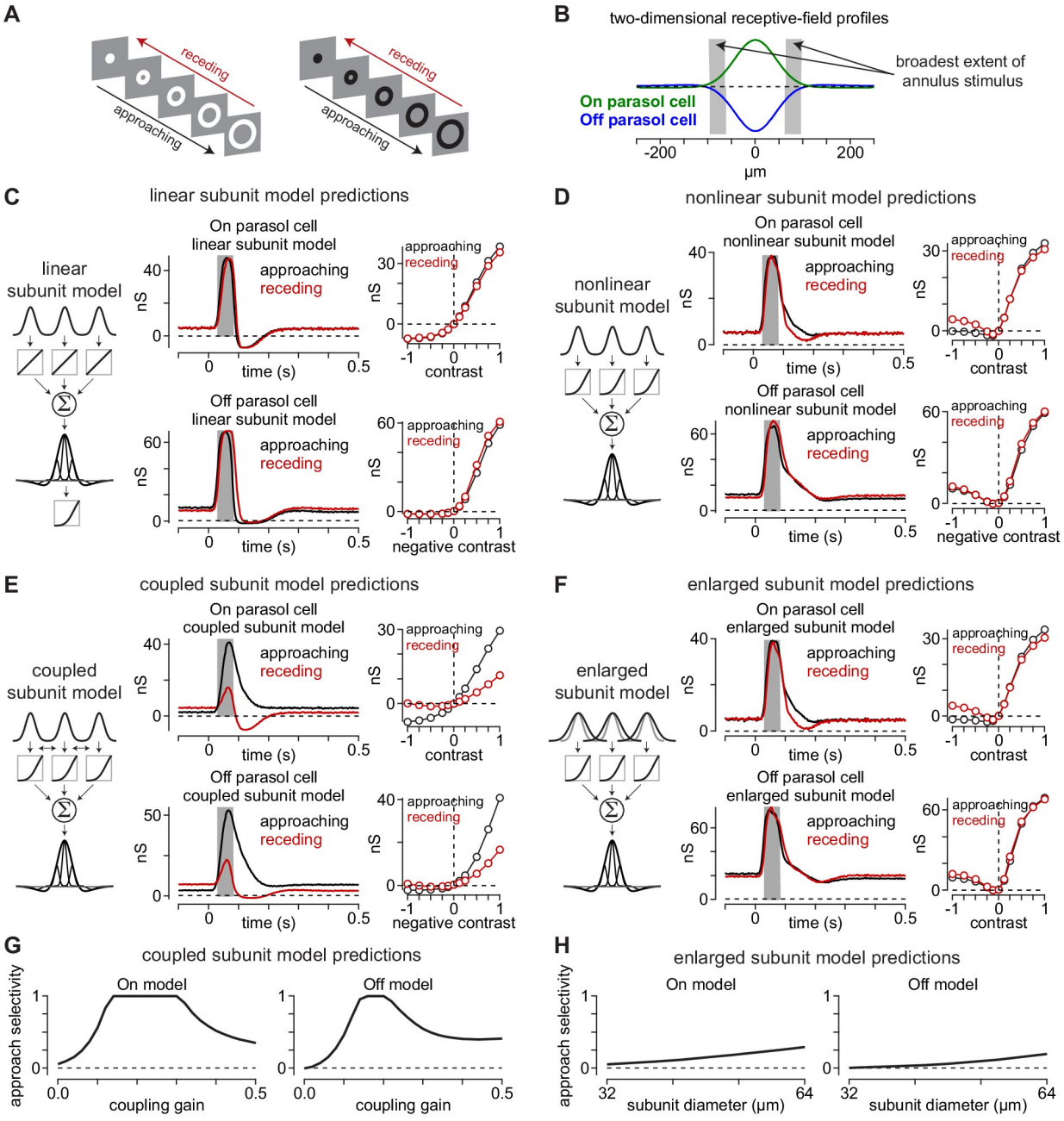
A
receding
approaching
receding
approaching
B
two-dimensional receptive-field profiles
broadest extent of annulus stimulus
On parasol cell
Off parasol cell
-200
0
200
µm
C
linear subunit model predictions
linear subunit model
On parasol cell linear subunit model
approaching
receding
nS
time (s)
contrast
Off parasol cell linear subunit model
negative contrast
D
nonlinear subunit model predictions
nonlinear subunit model
On parasol cell nonlinear subunit model
Off parasol cell nonlinear subunit model
E
coupled subunit model predictions
coupled subunit model
On parasol cell coupled subunit model
Off parasol cell coupled subunit model
F
enlarged subunit model predictions
enlarged subunit model
On parasol cell enlarged subunit model
Off parasol cell enlarged subunit model
G
coupled subunit model predictions
On model
Off model
approach selectivity
coupling gain
H
enlarged subunit model predictions
subunit diameter (µm)

Figure 2.5: Canonical receptive-field models predict a lack of approach selectivity. (A) Stimulus paradigm for approaching and receding annuli. Annuli either rapidly increased in radius (approaching) or decreased in radius (receding). (B) Two-dimensional spatial receptive-field profiles used in the model. Values were determined directly from parasol cell recordings as shown in Figure 2. Gray regions indicate the widest extent of the moving annuli. (C) The linear subunit model was created in which subunit input was integrated linearly prior to a single nonlinearity at the ganglion cell output. Model parameters came directly from measurements of spatiotemporal receptive field properties. On and Off models predicted similar responses for both approaching and receding annuli. (D) A model in which the output of each subunit was passed through the output nonlinearity prior to integration at the level of the ganglion cell also predicted similar responses to approaching and receding annuli. The nonlinear subunit model also predicted similar responses in Off parasol cells to approaching and receding annuli of a given contrast. (E) Output of On and Off models with electrical coupling between bipolar cells. This models produced excitatory conductances that were biased toward approaching motion. (F) A model in which coupling between subunits was absent, but the subunit receptive-field sizes were enlarged to simulate lateral spread through gap junctions. Approach selectivity was absent from this model, indicating that the increase in subunit receptive-field size alone could not account for the approach selectivity observed in (E). (G) Approach selectivity index calculated for the On and Off cell coupled subunit models at a series of coupling gains. Approach selectivity was highest for gains of $\sim$0.1–0.4. (H) Approach selectivity for the enlarged subunit models calculated for a series of subunit diameters. Selectivity was relatively low even at large diameters.

Unlike their predictions for the texture stimuli (Figure 2.3), the linear and nonlinear subunit models both predicted a lack of approach selectivity for the moving annuli, as model outputs were similar for the approaching and receding annuli at all contrasts (Figure 2.5C, D). The coupled subunit model, however, predicted larger responses to approaching annuli than to receding annuli (Figure 2.5E).

What accounts for the approach bias predicted by the coupled subunit model? It was proposed to us that the effect of coupling in expanding the subunit receptive-field size could explain the observed approach motion bias. Indeed, some studies have proposed that electrical coupling significantly increases the size of bipolar cell receptive fields [153, 160–162]. We sought insight into whether altering the subunit receptive-field size could account for the observed approach bias. We did this by varying the subunit receptive-field diameters in models lacking electrical coupling between subunits.

We used a receptive-field diameter of 32 μm in our coupled subunit model that exhibited approach selectivity to moving annuli (two-standard-deviation diameter; Figure 2.5E). This value was based on a previous study in which we used direct measurements of excitatory synaptic currents in parasol ganglion cells to determine the subunit size, coupling gain between subunits (gain, 0.1), and space constant for electrical coupling in the diffuse bipolar cell networks (λ, 36.4 μm) [25]. These model parameters would expand the subunit receptive field by $\sim$7 μm. Thus, if approach selectivity were a result of subunit receptive-field expansion, we would expect to observe comparable approach selectivity values for the coupled model and a model lacking electrical coupling with subunit diameters of $\sim$39–40 μm. However, this was not the case (Figure 2.5G, H). The coupled subunit models showed approach selectivity values of $\sim$0.5 when the coupling gain was 0.1 (On model, 0.56; Off model, 0.46), but the same models that lacked coupling and with subunit diameters of 40 m exhibited much lower approach selectivity (enlarged subunit model: On model, 0.09; Off model, 0.03). In fact, doubling the subunit receptive-field diameters did not reproduce the level of approach selectivity observed in the coupled subunit model or in our direct recordings from parasol ganglion cells (Figure 2.5G, H). Thus, approach bias does not arise primarily from enlarging subunit receptive fields.

These modeling simulations produced two principal results. First, the nonlinear subunit model predicted approach selectivity to the expanding texture stimuli (Figure 2.3), but not to the expanding annuli. Thus, if this model accurately reflects the underlying circuitry, then we should observe a lack of approach selectivity to the annulus stimulus in our direct recordings from primate ganglion cells.

Another important result of the simulations was the divergent predictions of the nonlinear and coupled subunit models (Figure 2.5D, E). These models were identical other than that the latter model simulated electrical coupling between subunits prior to the output nonlinearity. Thus, the differences in predicted output pattern between these two models suggested that electrical coupling in the bipolar cell network contributes to approach bias for certain classes of stimuli such as the

moving annuli (see Appendix 2.8). If such a mechanism were engaged by these stimuli, we would expect to observe approach selectivity to the moving annuli in our cellular recordings. Indeed, we next tested these predictions by recording the responses of ganglion cells to the moving annulus stimulus paradigm.

Consistent with the predictions of the coupled subunit model, parasol cells exhibited pronounced asymmetries to approaching and receding annuli. In On parasol cells, approaching bright annuli evoked much larger spike responses than receding annuli of the same contrast—at the highest contrast, approaching motion elicited 85.4 ± 10.9 spikes s^{-1} versus 7.1 ± 4.3 spikes s^{-1} for receding motion (contrast, +1.0; mean ± SEM; n = 26 cells; $p=8.3 \times 10^{-6}$; $p<2.6 \times 10^{-5}$ at all contrasts; Wilcoxon signed rank test, here and below). Likewise, approaching motion to strong negative contrasts in Off parasol cells evoked 148.7 ± 12.8 spikes s^{-1} versus 55.2 ± 9.4 spikes s^{-1} for receding motion (contrast, –1.0; mean ± SEM; n = 24 cells; $p=2.1 \times 10^{-5}$; $p<3.4 \times 10^{-5}$ at all contrasts).

We calculated the approach selectivity index for each cell (Figure 2.6H). Unlike to the moving textures, Off smooth monostratified and broad thorny cells lacked consistent approach selectivity to the annulus stimulus, but approach selectivity persisted in On smooth monostratified and On and Off parasol cells. Besides demonstrating that approach selectivity generalized to a broader range of visual stimuli in the latter three cell types, these results aligned well with the predictions of the coupled subunit model, suggesting that electrical coupling or other lateral interactions within the network contributes to approach selectivity in these cells. To gain further insight into the circuit mechanisms involved, we performed synaptic current recordings from parasol cells to the moving annulus stimulus paradigm.

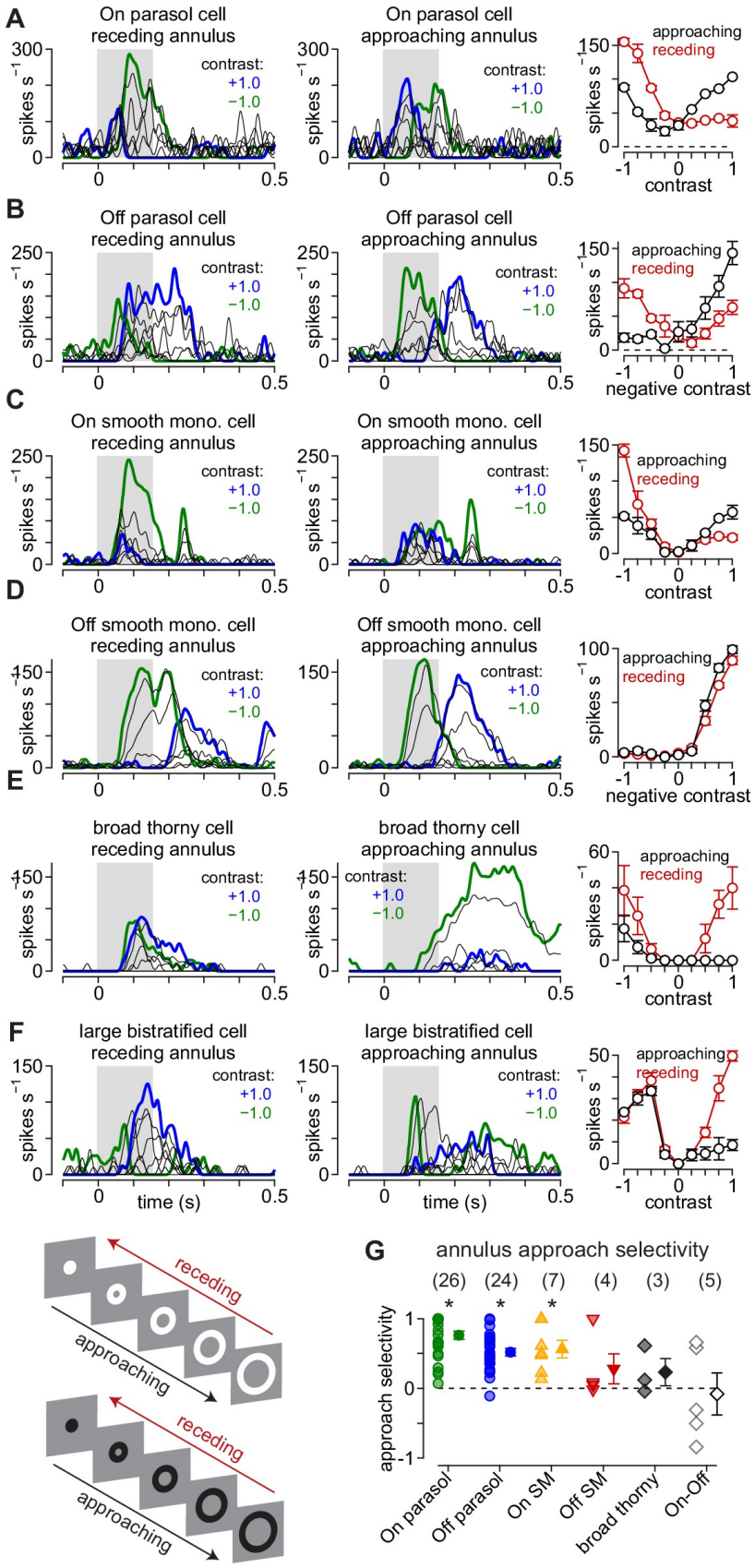
A
On parasol cell
receding annulus
On parasol cell
approaching annulus
contrast:
+1.0
−1.0
spikes s⁻¹
approaching
receding
contrast
B
Off parasol cell
receding annulus
Off parasol cell
approaching annulus
negative contrast
C
On smooth mono. cell
receding annulus
On smooth mono. cell
approaching annulus
D
Off smooth mono. cell
receding annulus
Off smooth mono. cell
approaching annulus
E
broad thorny cell
receding annulus
broad thorny cell
approaching annulus
F
large bistratified cell
receding annulus
large bistratified cell
approaching annulus
time (s)
receding
approaching
G
annulus approach selectivity
(26) (24) (7) (4) (3) (5)
approach selectivity
On parasol
Off parasol
On SM
Off SM
broad thorny
On-Off

Figure 2.6: Approach motion selectivity for moving annuli. (A) Spike responses in an On parasol ganglion cell to receding (left) and approaching (middle) annuli presented at a series of contrasts. Right, Average spike rate during movement of receding (red) and approaching (black) annuli as a function of stimulus contrast. (B–F) Same as (A) for Off parasol (B), On smooth monostratified (C), Off smooth monostratified (D), broad thorny (E), and large bistratified ganglion cells (F). (G) Approach sensitivity index values for the stimulus paradigm. Transparent shapes indicate individual cells. Opaque shapes and error bars indicate mean ± SEM. Asterisks indicate statistically significant values, determined using the Wilcoxon signed rank test.

2.3.5 Distinct contributions of the On and Off visual pathways to approach motion selectivity

We presented the approaching and receding annuli while recording the excitatory and inhibitory synaptic inputs to parasol ganglion cells (see Materials and methods). Excitatory and inhibitory currents were measured by holding a cell's membrane voltage at the reversal potentials for inhibitory (E_{Cl}, –70 mV) and excitatory synaptic currents (E_{cation}, 0 mV), respectively. The pattern of excitatory synaptic inputs mirrored the observed spiking pattern—excitatory currents were largest for approaching annuli matching the cell's preferred contrast polarity—positive contrasts in On cells and negative contrasts in Off cells (compare Figure 2.6, Figure 2.7). For example, 100% preferred-contrast approaching annuli evoked excitatory inputs that were much larger than receding annuli in both On (approaching, 40.4 ± 9.3 pC; receding, 0.7 ± 5.5 pC; n = 16 cells; p=4.4×10^{-4}) and Off parasol cells (approaching, 97.5 ± 17.2 pC; receding, 29.0 ± 10.5 pC; n = 19 cells; p=1.3×10^{-4}). In addition, receding annuli that were of a non-preferred contrast evoked larger responses than approaching annuli of the same contrast. These data indicated that the sensitivity to approaching motion observed in the parasol cell spike outputs was present in the excitatory synaptic inputs from diffuse bipolar cells to parasol ganglion cells (Figure 2.7). Inhibitory synaptic input to parasol cells showed the opposite pattern to that of excitation. Preferred-contrast receding annuli produced larger inhibitory currents than approaching annuli of the same contrast polarity (On: approaching, 89.4 ± 26.9 pC; receding, 127.4 ± 28.6 pC; n = 13 cells; p=0.15; Off: approaching, 64.1

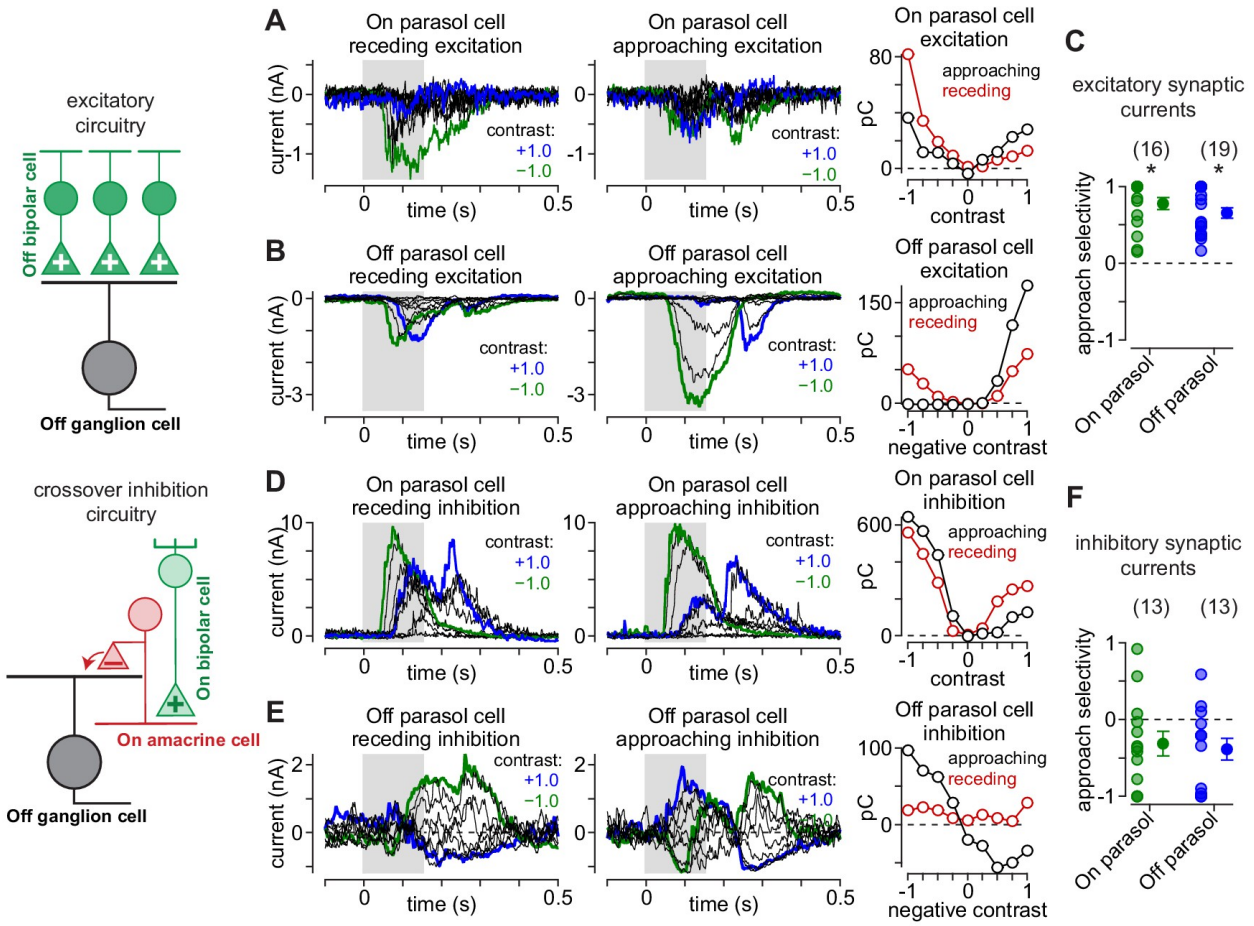

Figure 2.7: Asymmetrical synaptic input patterns underlie approach motion selectivity.Excitatory synaptic currents measured in an On parasol ganglion cell to receding (left) and approaching (middle) annuli presented at a series of contrasts. Right, Excitatory charge during movement of receding (red) and approaching (black) spots as a function of stimulus contrast. (B) Same as (A) for an Off parasol cell. (C) Approach selectivity index for excitatory synaptic currents for On (green) and Off parasol cells (blue). Individual cells are shaded; solid circles indicate mean ± SEM. (D) Inhibitory synaptic currents measured in an On parasol ganglion cell to receding (left) and approaching (middle) annuli presented at a series of contrasts. Right, Inhibitory charge as a function of contrast in the On cell. (E) Same as (D) for the Off parasol cell. (F) Approach selectivity index for inhibitory synaptic currents for On (green) and Off parasol cells (blue). Individual cells are shaded; solid circles indicate mean ± SEM. Statistical significance is indicated with an asterisk and was determined using the Wilcoxon signed rank test.

± 27.7 pC; receding, 114.4 ± 29.3 pC; n = 13 cells; $p=1.7 \times 10^{-2}$). This finding indicated that the increased selectivity to approaching motion was mediated by a combination of increased synaptic excitation and reduced synaptic inhibition relative to receding motion; this pattern of synaptic input amplified the differences in parasol cell responses to approaching and receding motion.

Our synaptic current recordings revealed an apparent contribution of inhibitory synaptic input to approach selectivity. Inhibitory input to parasol cells arises primarily from crossover inhibition [163, 16]. This type of inhibition emerges from amacrine cells with opposing contrast polarity—Off-type amacrine cells inhibit On parasol cells and On-type amacrine cells inhibit Off parasol cells. In addition to directly inhibiting ganglion cells, circuits for crossover inhibition can modulate glutamate release from retinal bipolar cells by directly inhibiting their synaptic terminals, and this can produce pronounced effects on ganglion cell firing [16, 164]. Thus, crossover inhibition can manifest in both the direct inhibition onto the ganglion cell and in the excitatory input from bipolar cells.

To measure the presynaptic and postsynaptic contributions of crossover inhibition to approach motion selectivity, we recorded synaptic currents in Off parasol cells while blocking crossover inhibition with agents that selectively disrupt signaling between photoreceptors and On-type bipolar cells [165]. We used an mGluR6 agonist/antagonist combination (L-APB, 5 μM; LY341495, 7.5 μM), which has been shown to silence crossover inhibition while minimizing off-target effects in primate retina [166]. A comparable pharmacological manipulation was not available for isolating crossover inhibition on On-type ganglion cells [25], so we focused on Off parasol cells for these experiments.

Crossover inhibition can act both presynaptically, by modulating bipolar cell glutamate release, and postsynaptically, by directly inhibiting ganglion cell dendrites [167–169, 16, 164, 170]. We measured these effects by recording excitatory and inhibitory synaptic input before and after blocking crossover inhibition (Figure 2.7—figure supplement 1). The effect of blocking crossover inhibition on excitatory synaptic inputs differed for approaching and receding motion. Blocking crossover inhibition did not significantly affect the magnitude of evoked excitatory synaptic currents to approaching motion, but to receding motion, excitatory currents increased following crossover blockade relative to the control condition (Figure 2.6—figure supplement 1A, B). This subsequently reduced approach selectivity relative to the control condition (Figure 7—figure sup-

plement 1C; n = 6 cells; p=1.6 × 10^{-2}; Wilcoxon signed rank test). These data indicated that during receding motion, the amacrine cell responsible for crossover inhibition provided inhibition at presynaptic bipolar terminals, but this presynaptic inhibition was not present during approaching motion.

These excitatory and inhibitory synaptic recordings indicated that crossover inhibition was more strongly recruited by receding motion than approaching motion. Thus, crossover inhibition enhanced approach motion selectivity by suppressing excitatory synaptic release and directly inhibiting ganglion cell dendrites during receding motion. Despite the apparent contribution of crossover inhibition to approach motion selectivity, excitatory synaptic input was larger for approaching motion than receding motion with crossover inhibition blocked. This indicated that the observed bias for approaching motion was present in both the bipolar cell and amacrine cell circuitries and was amplified by interactions between these circuit elements.

2.4 Discussion

We compared the responses of several primate ganglion cell types to approaching and receding motion. We found that parasol and smooth monostratified ganglion cells consistently showed larger responses to approaching textures and annuli relative to receding stimuli of the same type (Figure 2.1, Figure 2.6). We further demonstrated that the asymmetrical response patterns of these cells to approaching and receding motion arises from the concerted activity of excitatory and inhibitory synaptic inputs to these ganglion cells (Figure 2.5, Figure 2.7, Figure 2.7—figure supplement 1). Further, approach selectivity was weak or absent from several On-Off type cells indicating that it was not a general property of primate ganglion cells. Below, we note some functional implications of these results.

Canonical receptive-field models have been used to describe the visual properties of many ganglion cell types including parasol cells [53, 171] and smooth monostratified cells [28, 55]. These

models can accurately predict neural responses to a small subset of potential visual inputs such as briefly presented stimuli (Figure 2.5—figure supplement 1) or spatiotemporally uncorrelated noise [171], but they perform poorly at predicting responses to stimuli containing spatiotemporal correlations [25, 42], including naturalistic stimuli [101, 17, 18]. These failures occur because retinal circuits contain many nonlinearities that are not considered in classical receptive field models. Indeed, the traditional linear-nonlinear spatiotemporal model failed to accurately predict the strong asymmetries observed to approaching and receding motion (Figure 2.5, Figure 2.5—figure supplement 1, Figure 2.6).

In vertebrates, the principal retinal nonlinearities arise at the level of bipolar cell glutamate release [50, 51]. Additional nonlinearities are produced by electrical coupling between bipolar cells [42, 25, 172, 173] and by inhibitory amacrine cells [174–176, 67]. Further, a recent study revealed strong nonlinearities in the interactions between different dendritic branches of smooth monostratified ganglion cells, providing an additional level of nonlinear interactions after the bipolar cell nonlinearities [140]. Besides frustrating attempts by researchers to produce accurate computational models of retinal processing, these nonlinearities form the basis for extracting (or rejecting) specific features from visual inputs. For example, amacrine cell input allows the $\sim$15 bipolar cell types to differentially affect the $\sim$30–40 ganglion cell pathways [177, 178, 32, 179]. Further, these interactions contribute to spatial selectivity [180, 66, 64, 181, 182] and short-term plasticity [183, 90, 92, 184, 93].

The prominent type of inhibitory input at play in approach motion selectivity, crossover inhibition, arises via interactions between the On and Off visual pathways. The circuit motif for crossover inhibition has been conserved across several vertebrate species including fish [185], salamanders [168], guinea pigs [164, 72], rodents [68, 169], rabbits [170], and primates [163, 16], and it contributes to a variety of visual functions (reviewed in [186]). Here, we demonstrate that crossover inhibition amplifies the asymmetrical responses of primate ganglion cells to approaching and receding motion by providing inhibition both at the level of the diffuse bipolar cell terminals

and at the level of the ganglion cell dendrites (Figure 2.7, Figure 2.7—figure supplement 1; [68]).

In addition, our findings highlight the utility of electrical synapses in neural computation. Electrical coupling between neighboring bipolar cells enhances responses to visual inputs containing spatiotemporal correlations and endows certain ganglion cells with generalized motion selectivity [42, 25] and enhanced direction selectivity in others [173]. Our results here suggest that the effects of electrical synaptic transmission varies with the type of motion—potentiation occurs during approaching motion and was absent during receding motion (Figure 5, Appendix 2.8). Perhaps, the prevalence of these synapses in the retina was partly an adaptation, early in vertebrate evolution, for processing the spatiotemporal correlations that are so common in visual environments [37, 155], including those generated during an animal's own motion through the environment (Figure 2.1, Figure 2.4; [145, 146, 156]).

2.4.1 Relationship to previous findings

In rodent retina, approach selectivity is found only in a single ganglion cell class—the Off Alpha ganglion cell and is absent from several other types [68]. We found approach selectivity to be more ubiquitous in the primate retina, manifesting in parasol, smooth monostratified, and broad thorny ganglion cells to varying degrees (Figure 2.1, Figure 2.6). This variation may reflect the distinct ethological demands on these species. For example, the need to quickly detect approaching dark objects, such as overhead predators would be necessary for survival in prey species like mice [187]. Thus, expression of approach selectivity in an Off-type ganglion cell would allow these vital computations to occur early in the visual pathway. Likewise, the arboreal habitats of early primates increased the need to quickly and accurately perform visually guided movements with the arms and hands and led to the expansion of areas in the parietal cortex responsible for these tasks [114]. These habitats may have also produced a need for light/dark symmetry in detecting approaching motion as well as self-motion through the environment [145, 146].

2.4.2 Contributions to visual processing in primates

The selectivity of these macaque ganglion cell types to approaching motion should be distinguished from the looming-sensitive neurons found in retinorecepient brain regions. For example, looming-sensitive neurons in the optic tectum of pigeons respond when an object moves toward the animal, but do not respond when the animal moves toward the object [188]. The ganglion cells that we tested would not be able to distinguish self-motion and object motion in this way. Instead, the approach motion selectivity that we observed would be an initial step in a series of computations culminating in the detection of approaching objects.

Indeed, the same circuit nonlinearities that enhanced selectivity to approaching motion also produced ambiguities between the direction (approaching/receding) and contrast (light/dark) of moving objects. This result indicates that downstream visual circuits receiving input from parasol and smooth monostratified ganglion cells would also require input from other retinal pathways to resolve these ambiguities. For example, downstream circuits might obtain a more faithful readout of the reflectance of a moving object from the concerted activity of midget ganglion cells and then, with the aid of this information, determine whether the object were approaching or receding. However, future studies will be needed to determine how and where in the visual stream such ambiguities are resolved.

2.5 Materials and Methods

Experiments were performed in an in vitro, pigment-epithelium attached preparation of the macaque monkey retina [63]. Eyes were dissected from terminally anesthetized macaque monkeys of either sex (Macaca fascicularis, mulatta, and nemestrina) obtained through the Tissue Distribution Program of the National Primate Research Center at the University of Washington. All procedures were approved by the University of Washington Institutional Animal Care and Use Committee.

2.5.1 Tissue preparation and electrophysiology

The retina was continuously superfused with warmed (32–35°C) Ames' medium (Sigma) at ∼6–8 mL min^{-1}. Recordings were performed from macular, mid-peripheral, or peripheral retina (2–8 mm, 10–30° foveal eccentricity). Physiological data were acquired at 10 kHz using a Multiclamp 700B amplifier (Molecular Devices), Bessel filtered at 3 kHz (8-pole [900 CT, Frequency Devices] in series with 4-pole in Multiclamp), digitized using an ITC-18 analog-digital board (HEKA Instruments), and acquired using the Symphony acquisition software package developed in Fred Rieke's laboratory (http://symphony-das.github.io).

Recordings were performed using borosilicate glass pipettes containing Ames medium for extracellular spike recording or, for whole-cell recording, a cesium-based internal solution containing (in mM): 105 CsCH3SO3, 10 TEA-Cl, 20 HEPES, 10 EGTA, 2 QX-314, 5 Mg-ATP, and 0.5 Tris-GTP, pH ∼7.3 with CsOH, ∼280 mOsm. Series resistance (∼3–9 MΩ) was compensated online by 50%. The membrane potential was corrected offline for the approximately –10 mV liquid junction potential between the intracellular solution and the extracellular medium. Excitatory and inhibitory synaptic currents were isolated by holding cells at the reversal potentials for inhibitory currents (Echloride, ∼–70 mV) and excitatory currents (E_{cation} , 0 mV), respectively.

2.5.2 Visual stimuli

Visual stimuli were generated using the Stage software package developed in the Rieke lab (http://stage-vss.github.io) and displayed on a digital light projector (Lightcrafter 4500; Texas Instruments) modified with custom LEDs with peak wavelengths of 405, 505, and 640 nm. Stimuli were focused on the photoreceptor outer segments through a 10X microscope objective. Mean light levels were in the medium photopic regime, (in photoisomerizations [R*] $cone^{-1}$ s^{-1}) L-cone: 1.5×10^4–1.5×10^5, M-cone: 1.2×10^4–1.3×10^5, S-cone: 3.9×10^3–5.5×10^4, rod: 3.6×10^4–4.0×10^5. The ratios of L-cone:M-cone:S-cone activations approximate the equal-energy white point

after removing the lens (J. Kuchenbecker and M. Manookin, in preparation). Contrast values for annuli are given in Weber contrast and for texture stimuli in root-mean-squared (RMS) contrast.

Spike rate values in the text are given relative to the maintained spike rate prior to presenting the stimulus. For several of the stimulus conditions (e.g. receding motion of a preferred contrast), these spike rates fell below zero and, as a result, the values were set to zero when calculating the approach selectivity index.

For extracellular recordings, currents were wavelet filtered to remove slow drift and amplify spikes relative to the noise [189] and spikes were detected using either a custom k-means clustering algorithm or by choosing a manual threshold. Spike rate (in spikes s^{-1}) was calculated using a Gaussian temporal envelope (SD, 0.67 ms). Prior to analysis, data were downsampled to 1 kHz using a Chebushev filter (type I IIR; filter order, 8). Whole-cell recordings were leak subtracted and responses were measured relative to the median membrane currents immediately preceding stimulus onset (0.25–0.5 s window).

2.5.3 Stochastic textures

The stochastic texture stimuli used in the model were generated by bandpass filtering a matrix of random noise [146]. To simulate approaching or receding motion, the center frequency of the filter changed on each frame such that each frame was a rescaled version of the original texture (geometric mean spatial frequency, 1.6 cycles degree^{-1}). This bandpass filter was a cosine function in the spatial frequency domain:

$$\hat{F}(\omega) = .5 + .5cos(W), -\pi \leq W \leq \pi \tag{2.2}$$

where

$$W = log_2\left(\frac{\omega}{2f(t)}\right) \tag{2.3}$$

where ω are the spatial frequencies in the image with the F_0 component shifted to the center of the

spectrum (using the fftshift function in MATLAB). Values of W (in radians) were constrained to fall between $\pm\pi$. Texture spatial frequency (f) changed exponentially as a function of time:

$$f(t) = exp(log_e[f_0] - rt) \tag{2.4}$$

where f0 is the peak frequency of the filter at time zero and r is the rate of texture expansion in Hz. Spatial frequency proceeded from the highest to the lowest values for approaching textures and from the lowest to the highest values for receding textures as in Equation 2.4.

2.5.4 Difference-of-Gaussians receptive field model

For each of the computational circuit models, the parasol cell receptive field was modeled as a difference-of-Gaussians. Receptive-field parameters were measured using sinusoidally modulated spots that varied in size. Spike responses were fit with Equation 5 [190, 191]:

$$R = \omega_{center}\left(1 - exp\left(-\frac{r^2}{2\sigma^2_{center}}\right)\right) - \omega_{surround}\left(1 - exp\left(-\frac{r^2}{2\sigma^2_{surround}}\right)\right) \tag{2.5}$$

where w_x is the weighting of the center or surround and $_x$ is the standard deviation of the center or surround. The sizes and weightings of center and surround regions were then used in the pooling stage of our computational models.

2.5.5 Determining the difference in kinetics between center and surround

The kinetics of center and surround regions of the receptive field were measured using a Gaussian temporal flicker stimulus. On each stimulus frame, center or surround regions were uniformly presented with a single contrast which was drawn pseudo-randomly from a Gaussian distribution with a mean of 0.0 and a standard deviation of 0.1. Temporal filters were then determined by cross-correlating the presented contrast trajectory (S) with the cell's spike output (R; Equation 6; [79]).

$$F(t) = \int R(\tau)S(t+\tau)(d\tau) \tag{2.6}$$

These filters were then modeled as a damped oscillator with an S-shaped onset [113, 192] as described by Equation 7,

$$F(t) = A\frac{(t/\tau_{rise})^n}{1+(t/\tau_{rise})^n} exp\left(-t/\tau_{decay}\right) cos\left(\frac{2\pi t}{\tau_{period}} + \varphi\right) \tag{2.7}$$

where A is a scaling factor, τ_{rise} is the rising-phase time constant, τ_{decay} is the damping time constant, τ_{period} is the oscillator period, and φ is the phase (in degrees). For surround subunits, a temporal lag of 15 ms was included in the temporal component of the receptive field to account for the delay relative to the center (see Figure 2.2).

The relationship between input and output (i.e. the nonlinearity) was calculated by convolving the temporal filter and stimulus to generate the linear prediction (P)

$$P(t) = \int F(\tau)S(t-\tau)(d\tau) \tag{2.8}$$

The prediction (x-axis) and response (y-axis) were modeled as a cumulative Gaussian distribution [99].

$$N(x) = \varepsilon + \frac{\alpha}{\sqrt{2\pi}} \int_{-\infty}^{\alpha} e^{\frac{-(\beta t+\gamma)^2}{2}} dt \tag{2.9}$$

where α indicates the maximal output value, ε is the vertical offset, β is the sensitivity of the output to the generator signal (input), and γ is the maintained input to the cell. In practice, Equation 9 was invoked using MATLAB's cumulative distribution function ($normcdf$).

We created models of the retinal circuitry to gain a deeper understanding of how synaptic nonlinearities and circuit motifs could shape neural response properties. The model was implemented in the following stages:

Space-time filtering stage

- Generate the subunit spatiotemporal receptive fields (F)
- Generate a stimulus (S) with the same dimensionality as the receptive field. Stimulus values are given in contrast.
- Generate the subunits linear response (R) by convolving the stimulus and receptive field; add Poisson noise.

Coupling stage (coupling model only)

- Calculate the Euclidean distance between each pair of subunits (d).
- Calculate the change in current in each subunit due to simulated electrical coupling.

Subunit input-output stage

- Pass the result (R) through the appropriate input-output function.

Pooling stage

- Apply temporal delay to subunits forming the ganglion cell's receptive-field surround.
- Weight each subunit according to its distance from the model ganglion cell's receptive field center.
- Sum subunit inputs to the model ganglion cell.

2.5.6 Stage 1: Subunit spaec-time filtering

We first generated a hexagonal grid of model subunits with an average spacing of 32 μm between neighboring units. The location of each subunit was randomly shifted in the x and y dimensions to simulate randomness in the bipolar cell mosaic (s. d. ± 2 μm). Subunit spatial filtering was

modeled with a difference-of-Gaussians receptive-field model (Equation 2.5) using parameters based on previous measurements from diffuse bipolar cells in macaque retina (Dacey et al., 2000; Boycott and Wässle, 1991; Tsukamoto and Omi, 2015; Tsukamoto and Omi, 2016). Temporal filtering was performed using parameters from Equation 2.7 obtained by direct measurement of excitatory synaptic outputs of diffuse bipolar cells onto parasol cell dendrites (Manookin et al., 2018). Thus, the subunit's spatiotemporal receptive field (F) was the product of a two-dimensional difference-of-Gaussians (spatial domain, x) and a temporal filter (time domain, t). The output of each subunit (R) was determined by convolving the stimulus (S) with the subunit's spatiotemporal receptive field (F) as described in Equation 10.

$$R(t) = \int_0^t d\tau \int d^2x F(\overrightarrow{x}, \tau) S(\overrightarrow{x}, t-\tau) \tag{2.10}$$

Random fluctuations in membrane potential were simulated by adding Poisson noise to subunit responses; noise values were based on our previous direct measurements of diffuse bipolar cell synaptic outputs [25].

2.5.7 Stage 2: Apply coupling between subunits

For the coupling model, we first calculated the Eucliean distance between model subunits from their x- and y-locations.

$$d_{ij} = \sqrt{(x_i - x_j)^2 + (y_i - y_j)^2} \tag{2.11}$$

where d_{ij} is the distance between the ith and jth subunits.

Subunits in the coupling model shared a portion of their output based on differences in driving force and distance between subunits (Equation 12). The response of each subunit following coupling was determined by adding the change due to coupling to the response prior to coupling (R_0).

$$R_i(t) = R_{0i}(t) + \left[\sum_{j=1}^{n} g(R_{0i}(t) - R_{0j}(t))exp(-d_{i,j}/\lambda)\right] \tag{2.12}$$

where g is the coupling gain or portion of the response shared between subunits, λ is the coupling length constant, $d_{i,j}$ is the pairwise Euclidean distance between the ith and jth subunits, and n is the total number of subunits in the model.

2.5.8 Stage 3: Subunit input-output functions

The response of each subunit was then passed through the appropriate input-output function—responses in the linear subunit model were passed through a linear function (i.e., $y = x$) and the nonlinear and coupled subunit models were passed through the nonlinear function that we directly measured from excitatory synaptic inputs to parasol ganglion cells (see Equation 2.9).

2.5.9 Stage 4: Pooling

The final stage of the model, the pooling stage, was then performed for each of the three subunit models. Model ganglion cell responses were the weighted (w_x) sum of inputs from center and surround subunits (z_x).

$$z_{RGC}(t) = \omega_{center} z_{center}(t) - \omega_{surround} zsurround(t) \tag{2.13}$$

where the weightings of the center and surround regions of the ganglion cell receptive field (ω_x) were determined via direct measurements from parasol cells (see Figure 2, Equation 2.5). To determine the pooled inputs from center and surround subunits (z_x), subunit responses (N) following spatiotemporal filtering (linear subunit model) or the output nonlinearity (nonlinear and coupled

subunit models) were pooled according to Equation 14,

$$z_x(t) = \sum_{i=1}^{n} N_i(t) exp(-d_i^2/2\sigma_x^2) \tag{2.14}$$

where d_i is the Euclidean distance from the ith subunit's receptive field center to the center of the ganglion cell's receptive field and σ_x is the standard deviation of the center or surround regions of the ganglion cell's receptive field (see Figure 2.2, Equation 2.5).

2.5.10 Decoding models

We employed two decoding models to better understand how accurately downstream visual circuits could determine the direction of texture motion from the outputs of model On and Off parasol cells. The linear model summed the scaled outputs of the model On and Off cells as described in Equation 15,

$$f_{linear} = a_{on} r_{on} + a_{off} r_{off} \tag{2.15}$$

where a_{ON} and a_{OFF} are scaling constants. The quadratic model was similar in structure except that the response from each pathway was squared prior to summation (Equation 16),

$$f_{quadratic} = a_{on1} r_{on1} + a_{on2} r_{on2}^2 + a_{off1} r_{off1} + a_{off2} r_{off2}^2 \tag{2.16}$$

We evaluated the ability of the decoding models to distinguish between approaching and receding textures using the Jensen-Shannon distance. Model output was discretized by rounding to the nearest integer value. The Jensen-Shannon distance (i.e. the square-root of the Jensen-Shannon divergence) was calculated from the Kullback-Leibler divergence (D_{KL}) between the probability distributions for the model outputs to each approaching (P) and receding (Q) texture sequence.

$$JS_{dist}(P,Q) = \sqrt{\frac{1}{2}\left[D_{KL}\left(P\middle|\frac{P+Q}{2}\right) + D_{KL}\left(Q\middle|\frac{P+Q}{2}\right)\right]} \tag{2.17}$$

The Kullback-Leibler divergence between the model output distributions was calculated according to Equation 18.

$$D_{KL} = \sum_{n} p_n log_2 \left(\frac{p_n}{q_n} \right) \tag{2.18}$$

where p_n is the probability of observing an output of magnitude n in the sample window during approaching motion and q is the probability of observing an output of n in the sample window during receding motion.

2.5.11 Quantification and statistical analysis

All statistical analyses were performed in MATLAB (R2018b, Mathworks). Reported p values in this study were paired and were calculated using the Wilcoxon signed-rank test. Final figures were created in MATLAB (version R2018b), Igor Pro (version 8), and Adobe Illustrator.

2.6 Appendix

We simulated the subunit activation patterns encountered during approaching and receding annuli with diverging and converging network activations, respectively. Diverging network activation occurred when proximal subunits imparted current to the distal subunits, and converging activation occurred when the distal subunits imparted current to proximal subunits. In all cases, the total amount of input current in the network was conserved (x-axis). Following subunit activation, the input of each subunit was passed through an input-output function. Four different input-output functions were tested—a function in which the mapping between input and output was linear (i.e., y=x) and three nonlinear functions with differing shapes to their input-output relationships.

To determine whether the overall output of the network differs with network configuration, we varied the ratio of proximal and distal subunits and we computed the ratio of network output for

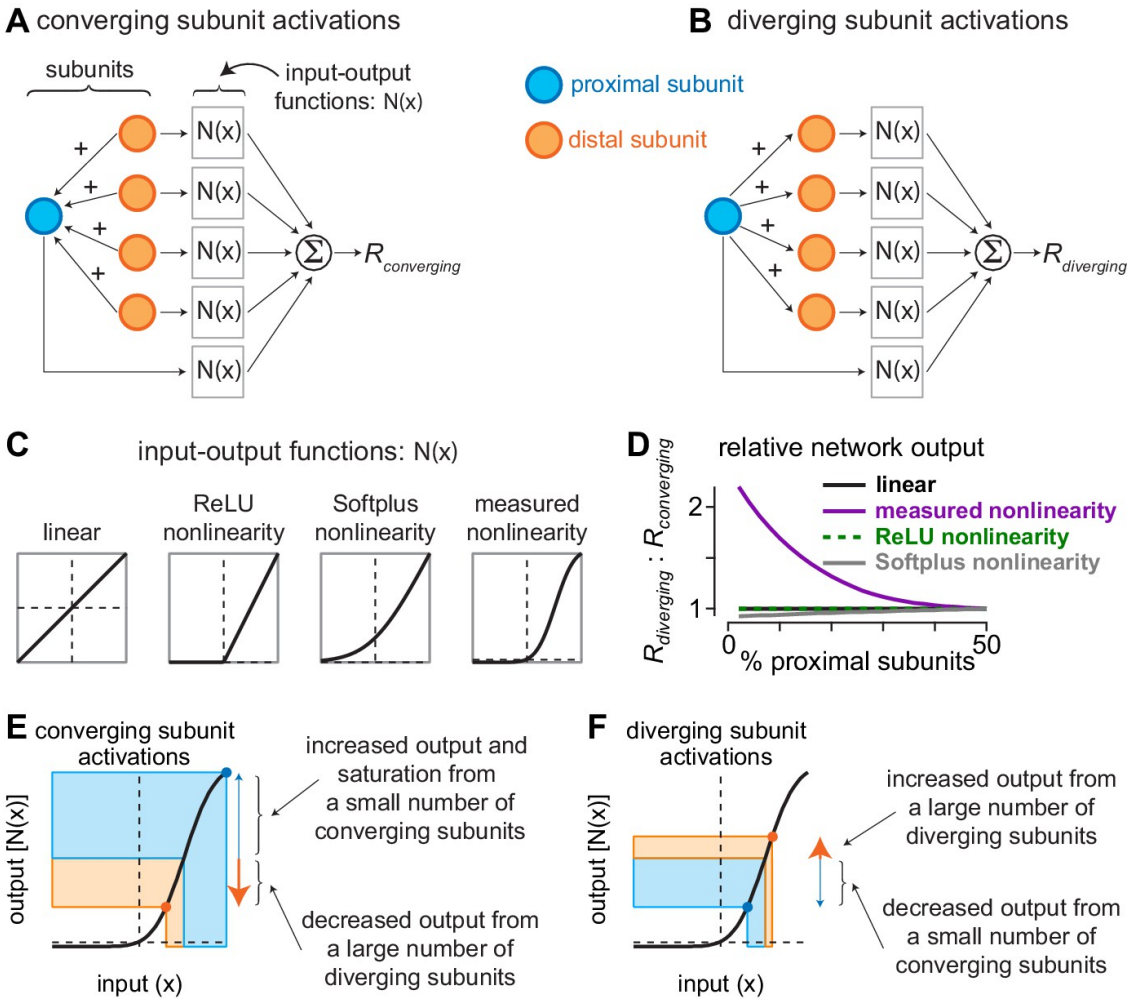

Figure 2.8: Current redistribution and nonlinearity shape determine network bias. (A) Activation pattern for converging subunit network. Distal subunits (orange) imparted a portion of their input to proximal subunits (blue). Subunit inputs then pass through input-output functions prior to being summed as the converging response ($R_{converging}$). (B) Activation pattern for diverging subunit network in which proximal subunits impart a portion of their current to distal subunits. (C) Shapes of different input-output functions evaluated with the network model. (D) Ratio of outputs from diverging ($R_{diverging}$) and converging ($R_{converging}$) activations (y-axis) as a function of the percentage of proximal subunits in the network (x-axis). The nonlinearity measured directly from excitatory synaptic inputs to parasol cells produced a large bias for diverging network activation when distal subunits outnumbered proximal subunits by $\leq$ 3:1. (E–F) Contributions of nonlinearity shape to output bias of subunit networks. (E) During convergent activation, the numerical mismatch between proximal and distal subunits and the shape of the input-output nonlinearity drives the small number of proximal subunits to saturating regions of the output curve, whereas the large number of distal subunits decrease their outputs. This results in a relatively small network output ($R_{converging}$). (F) During divergent activation, a small number of distal subunits are suppressed while a large number of distal subunits are potentiated, causing the network output to increase ($R_{diverging}$).

diverging activation ($R_{diverging}$) and converging activation ($R_{converging}$). For the linear and rectified linear unit (ReLU) input-output functions, the ratio of diverging and converging network activations was equivalent for all conditions tested, and the Softplus nonlinearity also lacked a bias for diverging subunit activation (Selectivity to approaching motion in retinal inputs to the dorsal visual pathway Appendix 1—figure 2.8D). However, the input-output function that we directly measured in parasol ganglion cells produced a very different result. Under conditions in which the relative number of proximal subunits was low, the network output was much (>100%) larger for diverging network activation than for converging activation, reminiscent of the approach motion bias observed in our subunit models (Figure 2.3, Figure 2.5).

Why does the shape of the input-output function produce such different network behaviors? The key to answering this question is in understanding the way in which the input currents are redistributed during network activation. When subunits impart a portion of their current, this current is divided equally among the recipient subunits. Thus, the current from a large number of subunits would produce a large positive movement along the input (x) axis if it were divided among a relatively small number of recipient subunits, and the subunits imparting the current would then show smaller negative movements along the input axis. Under conditions in which the movements occur along linear regions of the input-output function, the loss of current by imparting subunits and the gain in current by recipient subunits would cancel. However, if this gain in current occurred in a region in which the function saturates, as is the case for the function we directly measured in parasol cells, further increases along the input axis would produce negligible changes along the output axis; however, loss of current by imparting subunits would still produce a decrease along the output axis, resulting in a relatively small network output (Selectivity to approaching motion in retinal inputs to the dorsal visual pathway Appendix 1—figure 2.8E). Indeed, this is precisely the case in our network model when distal subunits greatly outnumber proximal subunits—converging network activation increases the inputs of a relatively small number of proximal subunits and decreases inputs of a large number of distal subunits. Proximal subunits are then pushed to regions of

the curve that produce saturation in the output. The output of distal subunits, however, decreases and this, coupled with the saturation of proximal subunits, produces a relatively small output from the network.

Diverging subunit activation produces a very different pattern. A relatively small number of proximal subunits impart a portion of their current to distal subunits. As a result, the proximal subunits decrease their outputs, while the distal subunits increase their outputs. Because the imparted current of a few proximal subunits is spread out over many more distal subunits, these distal subunits are unlikely to end up in a saturating region of the curve. Together, these factors result in a relatively large network output (Selectivity to approaching motion in retinal inputs to the dorsal visual pathway Appendix 1—figure 2.8F).

These simplified network simulations highlight two principles that are key to understanding how bias for approaching motion can arise from networks of electrically coupled subunits. First, the sequence in which the subunits are activated is critical—activation of a few subunits that then spreads to a larger number of subunits, as is the case during approaching motion, potentially produces the largest network outputs (Selectivity to approaching motion in retinal inputs to the dorsal visual pathway Appendix 1—figure 1D). Second, the shape of the input-output function is essential to the observed effects. Linear (linear; ReLU) or accelerating (e.g., Softplus) functions did not strongly affect network output. The nonlinearity we directly measured with our synaptic input recordings was sigmoidal, causing saturation at large positive values along the input axis. This saturation favors conditions in which activation is distributed over a larger number of subunits rather than strongly activating a few subunits. Thus, prudent selection of the shape of an input-output nonlinearity can be as important to neural circuit function as the placement of that nonlinearity within the circuit.

Chapter 3

Surround motion modulates the encoding properties of primate retinal ganglion cells

A version of this chapter is being peer reviewed for publication:

Todd R. Appleby, Fred Rieke, Michael B. Manookin (2024). Surround motion modulates the encoding properties of primate retinal ganglion cells *Cell Reports*. In review

3.1 Summary

Antagonistic interactions between center and surround regions of the receptive field are widely observed across sensory systems. In the early visual system, these interactions contribute to important computations such as edge detection. Less is known about how center-surround interactions depend on the spatiotemporal properties of the visual input. Here, we show that surround motion strongly modulated the response properties of two understudied primate ganglion cell types. Broad thorny cell responses were strongest when motion in the center and surround was uncorrelated, similar to object-motion-sensitive cells found in other species. A different pattern was observed in On smooth monostratified cells: surround activation was suppressive for static stimuli and facilitatory for motion. These effects of surround activation diverge significantly from classical center-surround models and more closely resemble how surround motion affects responses in primate visual cortex.

3.2 INTRODUCTION

The receptive field provides a concise summary of the stimulus selectivity of a sensory neuron, and much of what we know about early sensory systems has been learned by measuring receptive-field properties [9, 193]. In the early visual system, spatial receptive fields are classically composed of center and surround regions with distinct stimulus selectivity – the same stimulus falling in the center versus surround typically elicits responses with opposite polarity [193, 13, 10]. These differences in stimulus preference between center and surround subserve important general computations such as edge detection, wavelength selectivity, and efficient encoding of natural scenes [14, 15, 194, 28, 195, 196].

The canonical center-surround receptive field is described as a linear combination of responses to two opposing Gaussian spatial weighting functions – a relatively compact one describing the center, and a broader one describing the surround. In this framework an important function of the surround is to decorrelate spatial inputs. However, receptive field surrounds of different retinal ganglion cell types can be generated by distinct circuitry, and correspondingly surrounds can differ in their functional properties [197]. Cell type specific suppression of non-primate ganglion cells to saccade-like image shifts provides an example of specialized surround function [198–200]. Object-motion-sensitive cells provide another example. These cells respond strongest when motion in the center and surround is uncorrelated, thus enhancing the cell's response to local motion [66, 141, 201]. It is unclear whether primate ganglion cell surrounds share this diversity of motion-related function, in large part because the majority of primate cell types have not been characterized functionally.

To better understand the contributions of the receptive field surround to early visual processing in primates, we measured the effects of surround activation to moving and non-moving stimuli on the response properties of several understudied cell types – specifically broad thorny and smooth monostratified ganglion cells. Both cells exhibit classic center-surround antagonism for stationary

stimuli. However, motion in the receptive field surround produced distinct effects on the response properties of these cells. Broad thorny cells show sensitivity to differential motion between the center and surround regions of the receptive field, similar to the object-motion selectivity observed in other vertebrate retinas [66, 141, 201]. Unlike the broad thorny cells, motion in the receptive-field surround increased (facilitated) responses of On smooth monostratified cells to motion and non-motion stimuli. Thus, the receptive-field surround can produce varying effects on primate ganglion cells that depend on the retinal pathway and the statistics of incoming stimuli.

3.3 RESULTS

Our goal was to determine the impact of center-surround interactions on motion processing in several understudied primate ganglion cell types – particularly On smooth monostratified and broad thorny cells. First, we show that center-surround interactions cause broad thorny cells, but not On smooth monostratified cells, to respond more strongly to local motion relative to global motion. Second, we show that luminance and motion in the receptive field surround have distinct effects on the responsiveness of On smooth monostratified cells – changes in luminance produce classical receptive-field antagonism while motion produces non-classical response facilitation. Third, we show that the enhancement of On smooth monostratified cell responses produced by surround motion persists after motion ends.

On and Off parasol, On and Off smooth monostratified, and broad thorny ganglion cells were identified based on their characteristic responses to light steps, receptive field size, and dendritic morphology (Figure 3.1A, B; [30, 140]). We focused on how center-surround interactions influence responses to motion in On smooth monostratified and broad thorny cells, and we were particularly interested in cases in which such center-surround interactions differed from those observed in better-studied cells such as On and Off parasol cells.

Many of our experiments required targeting stimuli separately to the receptive-field center and

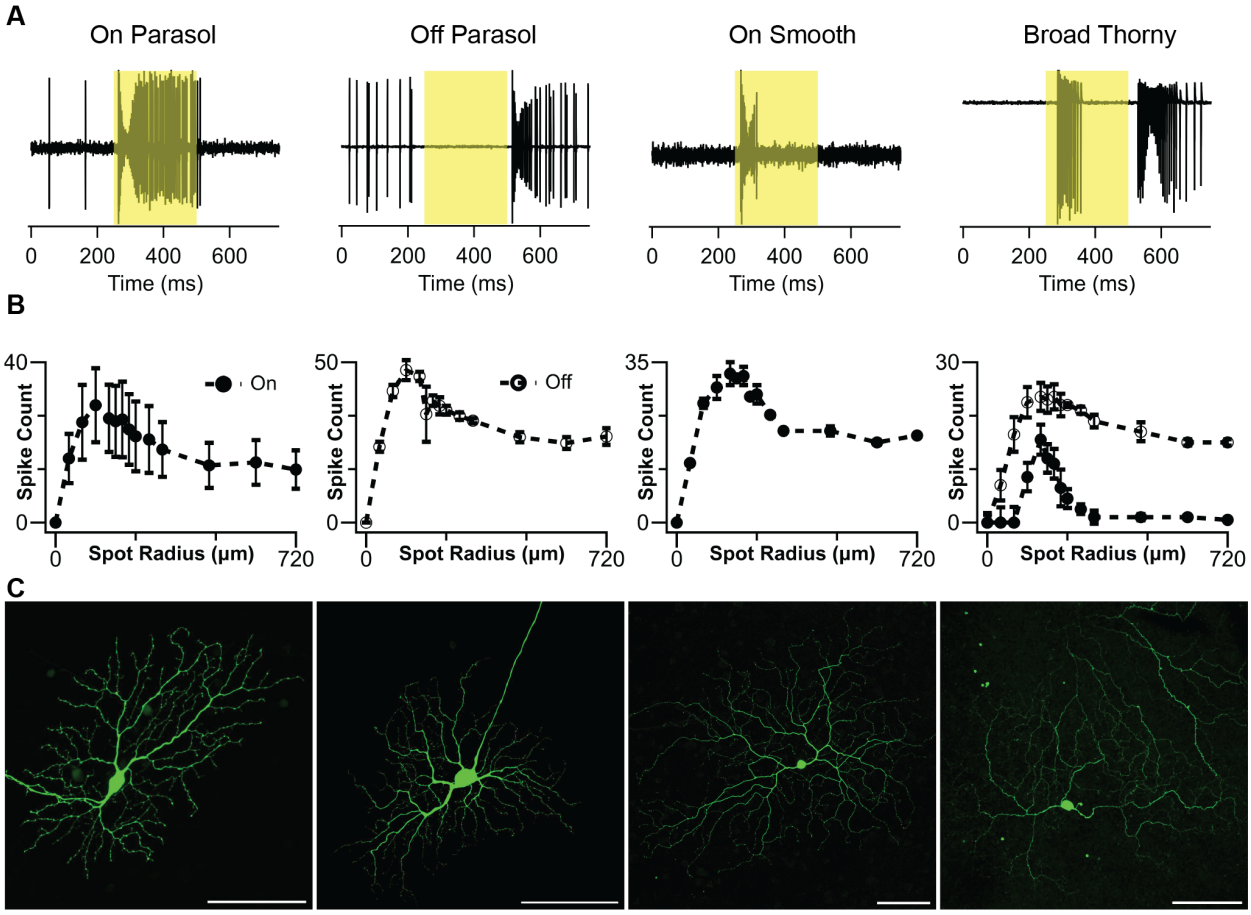

Figure 3.1: Ganglion cells show classical surround suppression to stationary spots (A) Spike responses to a 250 ms light step from On parasol, Off parasol, On smooth monostratified, and broad thorny ganglion cells measured with cell-attached recording. The duration of the light increment is highlighted in yellow. B) Spots of multiple sizes (40–720 μm radius) delivered for 500 ms to the receptive field center of each cell type. Spots were either contrast increments or decrements from a background, with contrast polarity matching the response polarity of each cell type. Broad thorny ganglion cell responses were elicited by contrast decrements to match the dominant polarity of the cell. (C) Fluorescence images of each cell's morphology generated on a confocal. Scale bar on each image is 100 μm.

surround. In each recorded cell, we used an annulus of increasing inner diameter to determine the radius at which responses switched from center dominated to surround dominated – the point at which either the annulus stopped generating spikes or the response polarity flipped (Supplementary Figure 3.8). Center-targeted stimuli were restricted to circular discs smaller than this radius, while surround-targeted stimuli were restricted to annuli with a larger inner radius. A gap between the

center and surround stimuli helped ensure good separation.

3.3.1 The On smooth monostratified and broad thorny cells show distinct sensitivities to center-vs-surround motion

Objects moving in a visual scene produce inputs that are uncorrelated relative to inputs created by global motion such as those produced by eye movements. To test for such object motion sensitivity, we used two stimuli previously used to identify this motion computation in non-primate retinal ganglion cells. The first stimulus captures several features of motion elicited by fixational eye movements([66]). This stimulus consists of randomly moving gratings with three conditions (Figure 3.2A, left; Supplementary Video 1 3.6): 1) a condition in which motion occurred only in the receptive-field center ('Center'), 2) a condition in which the random motion trajectories of the center and surround gratings were identical ('Correlated'), and 3) a condition in which the random trajectories of the center and surround gratings differed ('Uncorrelated') (see Methods). Across cell types, the center-only stimulus evoked instantaneous firing rates of at least 100 Hz. Figure 3.2B shows the mean spiking response to multiple random trajectory presentations for each condition.

We quantified these responses by comparing responses in the presence and absence of surround motion. Specifically, we measured the normalized difference between responses with surround motion and those with center motion only (see Methods). Object-motion-sensitive cells in non-primates produce weak responses to the 'Correlated' condition relative to the 'Center' condition and strong responses to the 'Uncorrelated' condition relative to the 'Center' condition17. Broad thorny ganglion cells in our recordings responded most strongly when the motion trajectory between center and surround was uncorrelated, similar to object-motion-sensitive cells found in other species (Figure 3.2B, C). Unlike broad thorny ganglion cells, On smooth monostratified cells responded well to motion in the surround regardless of whether it was correlated or uncorrelated with

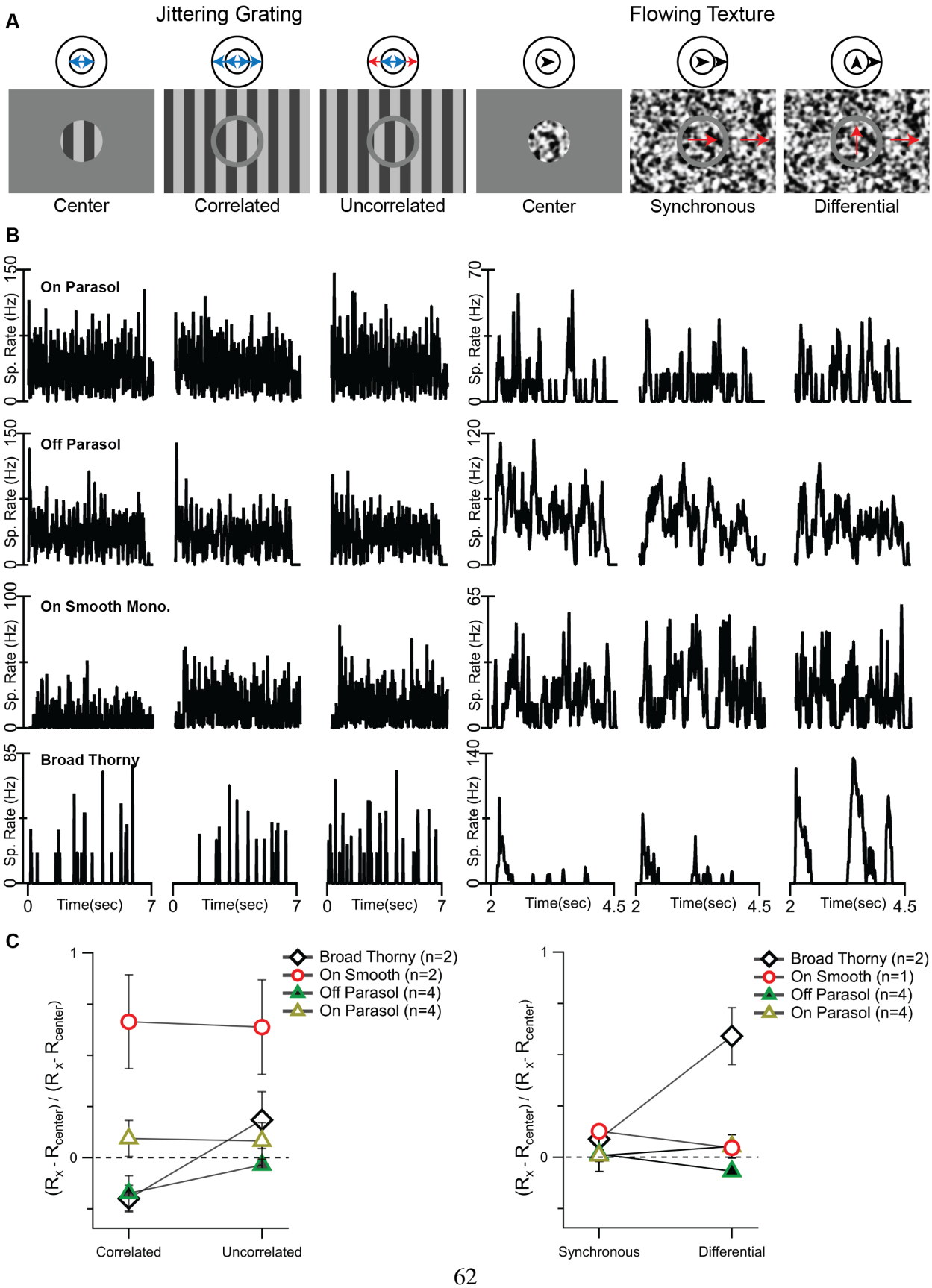
A
Jittering Grating
Flowing Texture
Center
Correlated
Uncorrelated
Center
Synchronous
Differential
B
On Parasol
Off Parasol
On Smooth Mono.
Broad Thorny
Sp. Rate (Hz)
Time(sec)
C
Broad Thorny (n=2)
On Smooth (n=2)
Off Parasol (n=4)
On Parasol (n=4)
On Smooth (n=1)
(Rx - Rcenter) / (Rx - Rcenter)
Correlated
Uncorrelated
Synchronous
Differential

Figure 3.2: Broad thorny and On smooth monostratified cells show distinct motion sensitivities (A) Jittering grating (left) and moving texture stimuli (right) used to characterize object versus background motion sensitivity. Single frames of each stimulus condition are depicted at the top of each column, along with a diagram indicating the relative trajectory of motion in the center and surround receptive-field regions (top). For example, in the Uncorrelated condition, the center and surround gratings follow distinct trajectories and this is indicated by blue and red arrows in the center and surround. (B) Spike responses for the stimulus in (A) for four cell types: On parasol (top row), Off parasol (second row), On smooth monostratified (third row), and the broad thorny (bottom row). Each response corresponds to the stimulus condition indicated in the aligned top panel. Spike rate responses to the flowing texture stimulus are shown starting at motion onset, two seconds after the stationary texture was presented. (C) Motion preferences were quantified by comparing responses with the surround (R_x) with those for the center-only stimulus (R_{center}). The normalized difference between these responses (y-axis) measures the spiking preference for each full-field condition relative to its center-only condition. Numbers of cells for each stimulus (Grating/Texture) are as follows: Broad thorny (n=2/n=2), On smooth monostratified (n=2/n=1), Off parasol (n=4/n=4), On Parasol (n=4/n=4). Points are mean ± S.E.M.

the center, but spiked less for motion limited only to the receptive-field center. Off parasol cells responses were modestly suppressed by motion in the surround and On parasol cells responses were enhanced, but, in both cases, these surround effects did not depend on the relation between center and surround motion.

The second stimulus comprised textures that flowed in a single direction, originally used to separate object-motion-sensitive ganglion cell types in the mouse retina18. Three stimulus conditions were tested: 1) a condition in which motion occurred only in the receptive-field center, 2) a condition in which motion in the center and surround were synchronous, and 3) a condition in which the direction of texture motion in the center was orthogonal to the direction of the surround texture.(Figure 3.2A, right; Supplementary Video 3.6). As with the jittering grating stimulus, the flowing texture stimulus evoked instantaneous firing rates of at least 100 Hz in each cell type. Broad thorny cells showed a strong preference for differential motion relative to center-only and synchronous motion (Figure 3.2B, C). Responses of On smooth monostratified cells and both On and Off parasol cells were not strongly affected by surround motion for this stimulus (Figure 3.2B, C).

In summary, these experiments revealed the distinct effects of surround motion on the response properties of four primate ganglion cell pathways. Surround motion did not strongly affect the responsiveness of On and Off parasol cells, but affected broad thorny and On smooth monostratified cells. Broad thorny cells, however, were strongly modulated by the degree of correlated motion between the center and surround regions of the receptive field. This dependence on the center-surround correlation structure was similar to object-motion-sensitive cells that have been described in salamander, rabbit, and mouse retina17–20. The responses of On smooth monostratified cells were also modulated by surround motion, but they did not depend on the center-surround correlation structure. Instead, surround motion facilitated responses in these cells. Thus, the effect of surround stimulation for On smooth monostratified cells depends on the stimulus properties – the surround is classically suppressive to changes in luminance and facilitatory for motion (Figures 3.1, 3.2).

3.3.2 Spatial correlations between moving objects modulates ganglion cell spike outputs

The classic stimuli used in Figure 3.2 distinguish cells that are sensitive to local versus global motion. This distinction has been helpful in identifying the roles these cells may play in vision. However, local and global motion represent two extreme forms of motion correlations, and testing sensitivity only to these extremes may not fully capture how the spatial scale of motion correlations impact responses. Such spatial scales will be important in relating motion preferences to natural vision (see Discussion). Hence, we measured how a cell's responses change as we systematically altered the spatial scale of motion correlations.

The stimulus that we used to measure tuning to the spatial scale of motion correlations consisted of small moving squares, with the motion trajectories of the squares consisting of two components: motion that was independent for each square, and motion that was correlated across

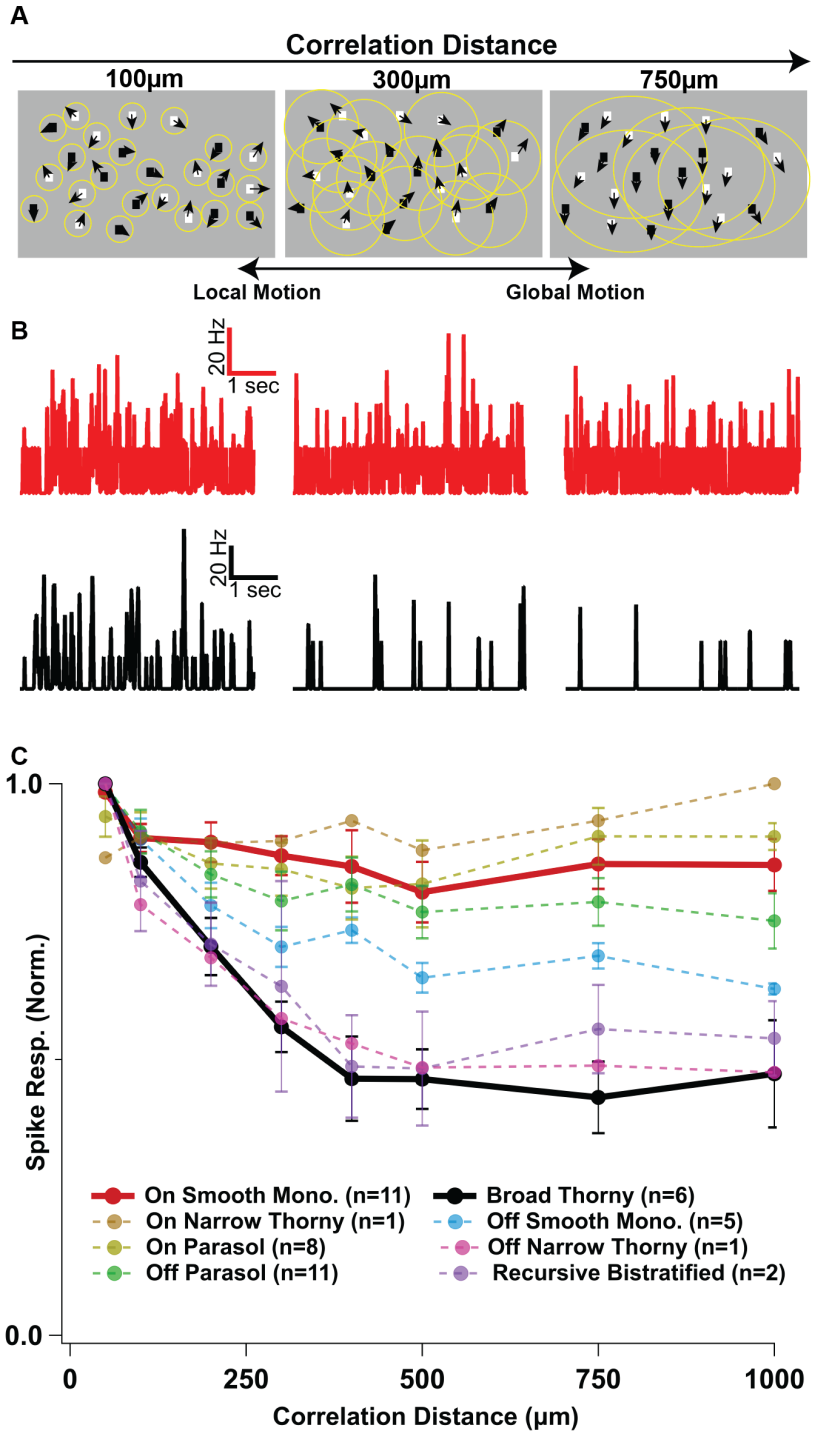

Figure 3.3: Spatial correlations modulate ganglion cell responses to motion. A) Stimulus diagram showing an increase in motion coherence between squares with increasing space constant. A larger correlation distance increases the coherent motion between distant squares. B) Example spike rates (average of 8 random trials) for a On smooth monostratified (top) and a broad thorny cell (bottom). Traces correspond to the correlation lengths shown in (A). (C) Average responses to the correlated motion stimulus for eight primate retinal ganglion cell types. Bold traces correspond to On smooth and broad thorny cell types. Included cell types are the On smooth monostratified (n=11), On narrow thorny (n=1), On parasol (n=8), Off parasol (n=11), broad thorny (n=6), Off smooth monstratified (n=5), Off narrow thorny (n=1), and recursive bistratified (n=2). Points are mean ± S.E.M.

squares. We measured responses to stimuli with a range of discrete distances of the correlated motion component (Figure 3.3A, B). The mean spike rate was determined at each correlation distance for each cell, creating a measure of sensitivity across a range of motion correlation distances (Figure 3.3C). Different ganglion cell types exhibited quite different dependencies on motion correlation distance – On parasol and On smooth monostratified cells showed little dependence on correlation distance, while broad thorny and several other understudied cell types showed a strong preference for motion correlations occurring over short distances.

Figures 3.2 and 3.3 show that broad thorny cells share several characteristics with the object-motion-sensitive cells identified in other species, most notably a strong preference for local over global motion. The On smooth monostratified cells showed a facilitatory interaction between motion in the surround and responses elicited in the receptive field center. This differs from the same cells' receptive fields for luminance, which show classic center/surround antagonism. Hence, we turned to additional experiments that further characterize how surround motion influences On smooth monostratified responses.

3.3.3 Motion in the receptive field surround shifts the input/output relationship of the receptive field center

We next asked whether surround facilitation for On smooth monostratified cells was truly motion sensitive or whether surround facilitation persisted when surround motion was replaced by local contrast variations over time [42, 25]. To answer this question, we measured a cell's spike output to a flickering spot over the receptive field center while modulating the surround with motion or non-motion stimuli. Equal numbers of black and white bars were presented in the surround under three different conditions (Figure 3.4A; Supplementary Video 3 3.6): (1) an apparent motion condition in which the bars moved from left to right across the screen, (2) a condition in which the bar locations were randomized to eliminate coherent motion, and (3) a static condition in which the

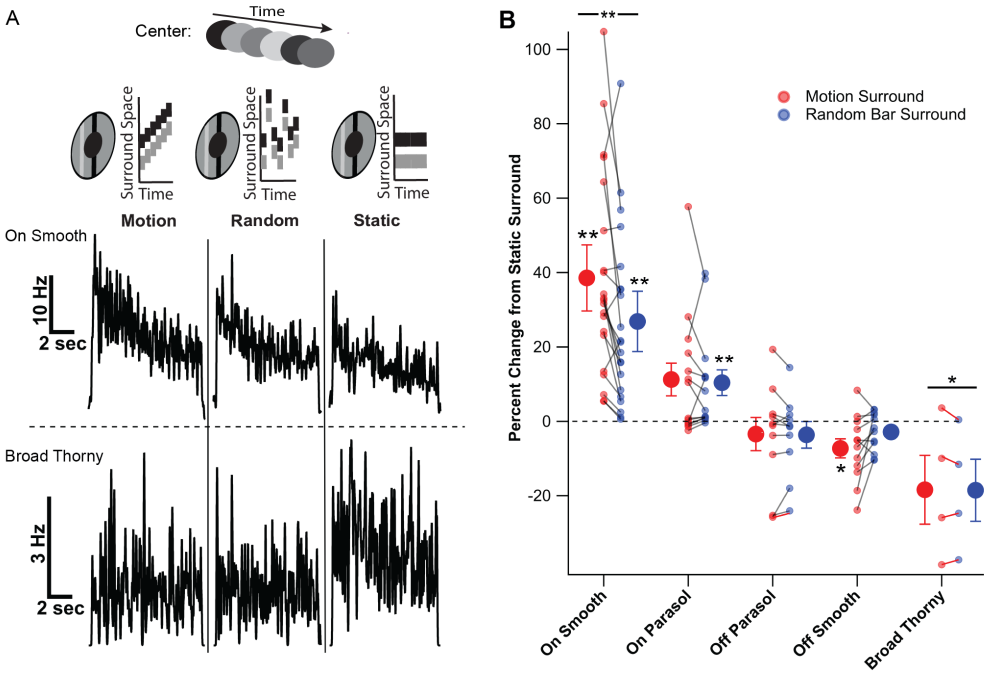

Figure 3.4: The effects of surround motion on spike output vary with ganglion cell type. A) Stimulus diagram (top) shows example bar space-time trajectories delivered to a cell's receptive-field surround in each surround condition. An example stimulus contrast trajectory delivered to the receptive field center is shown above the surround conditions. Surround condition diagrams align with example spiking responses for a single On smooth monostratified and broad thorny cell. B) Population data for On smooth monostratified (n=20), On parasol (n=14), Off parasol (n=10), Off smooth monostratified (n=12), broad thorny cells (n=4) tested using the surround motion stimulus. Statistical significance calculated by Wilcoxon signed rank test (*: $p < 0.05$; **: $p < 0.01$). Asterisks over means indicate a significant change from baseline. The asterisk and line above the broad thorny results indicates significance when motion and random samples are summed. The asterisks flanked by lines above the On smooth monostratified results indicate a significant difference between motion and random conditions. Error bars represent mean ± SEM.

bars were stationary.

The impact of the surround was determined by comparing changes in spike responses during the motion and random conditions to those during the static condition (Figure 3.4B). Both motion and random surround stimulation significantly increased responses of On smooth monostratified cells ($p = 8 \times 10\text{-}4$) and significantly decreased responses of broad thorny cells ($p = 1.6 \times 10\text{-}2$; Figure 3.4), whereas activation of the surround by preferred-polarity changes in luminance were

suppressive for both cell types (Figure 3.1). The increase in On smooth monostratified responses produced by the motion condition was significantly larger than that produced by the random condition ($p = 9 \times 10^{-3}$; Figure 3.4). Thus, dynamic activation of On smooth monostratified surrounds, particularly by coherent motion, facilitates spiking in these cells.

Several circuit mechanisms could account for modulation of the spike output by surround activitation. One mechanism is an additive/subtractive effect, in which surround activity controls the offset or bias of responses generated by activation of the center. Another is a multiplicative or gain scaling of responses generated in the center. These mechanisms produce distinct changes in a neuron's input-output relationship: changes in offset shift the relationship along the input axis while changes in gain change the slope.

We fit the responses with a linear-nonlinear model to distinguish between changes in offset and gain (Figure 3.5). In this paradigm, the relationship between the input stimulus and the neural response is described by a linear filtering stage and a nonlinearity that maps the output of the linear filter to spike rate23. A common linear filter was used for each cell and separate nonlinearities were calculated for each condition (Figure 3.5A-C). These nonlinearities were compared to determine whether the effect of motion in the receptive-field surround was to modulate the offset or the gain of the ganglion cell pathways. Changes in offset will be reflected by lateral shifts along the input/x axis, as suggested in Figure 3.5B, while changes in gain will affect the slope of the nonlinearity.

Different surround conditions produced clear changes in nonlinearities, especially in On smooth monostratified cells (Figure 3.5B). For On smooth monostratified cells, this analysis produced significantly lower error values for changes in horizontal offset ($p < 1.5 \times 10^{-4}$; $n = 20$; Figure 3.5D). The horizontal shift was significantly larger for the motion condition relative to the random bar condition, indicating that the observed facilitation was strongest when motion was present in the receptive-field surround ($p = 1.2 \times 10^{-3}$, Wilcoxon signed rank test, Figure 3.5E). Moreover, the On smooth monostratified cell motion and random conditions both had a mean horizontal shift that was significantly greater than baseline ($p = 8 \times 10^{-5}$ for motion and 1.9×10^{-3} for random, $n =$

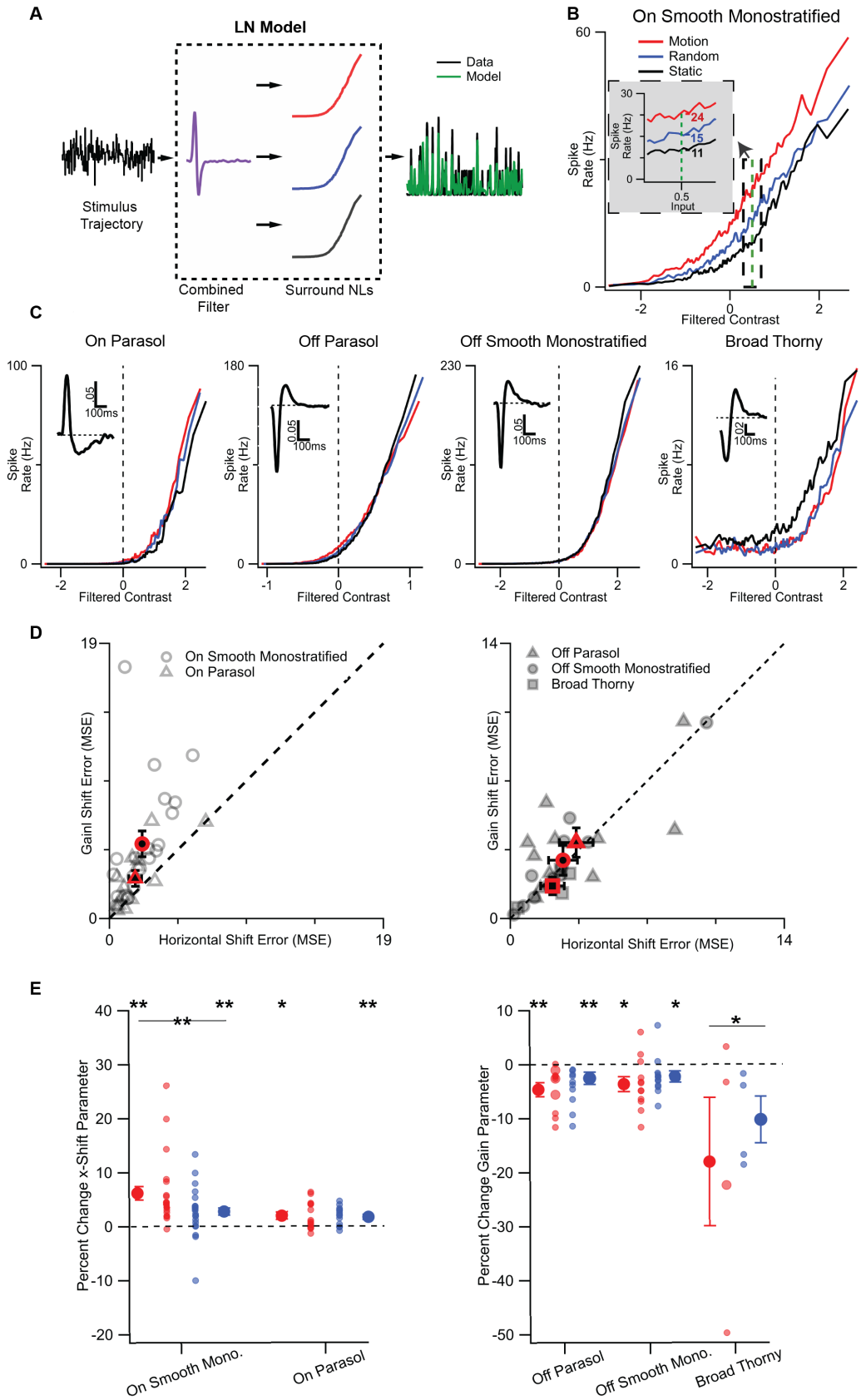
A
LN Model
Data
Model
Stimulus
Trajectory
Combined
Filter
Surround NLs
B
On Smooth Monostratified
Motion
Random
Static
Spike
Rate (Hz)
Filtered Contrast
C
On Parasol
Off Parasol
Off Smooth Monostratified
Broad Thorny
100ms
D
On Smooth Monostratified
On Parasol
Gainl Shift Error (MSE)
Horizontal Shift Error (MSE)
Off Parasol
Off Smooth Monostratified
Broad Thorny
Gain Shift Error (MSE)
E
Percent Change x-Shift Parameter
On Smooth Mono.
On Parasol
Percent Change Gain Parameter
Off Parasol
Off Smooth Mono.
Broad Thorny

Figure 3.5: Additive Mechanism Generates Surround Motion Sensitization. A) To generate input-output nonlinearities, a single temporal filter is generated from responses to the contrast trajectory (left) during surround conditions from stimulus in Figure 3.4 The temporal filter and stimulus create a shared generator signal, which is compared with the spiking output to each surround condition, creating an input-output nonlinearity for each stimulus condition. B) Example input-output nonlinearities from a On smooth monostratified cell shows sensitization during motion. Inset: numbers next to each nonlinearity show spike rate for a shared input. C) Example nonlinearities and average filters for On and Off parasol, Off smooth monostratified, and broad thorny cell types D) Mean squared error for either gain (y-axis) or horizontal shift (x-axis). Values above the unity line show a better fit when the horizontal shift parameter is allowed to change across modeled input-output curves. Error bars represent mean ± SEM. E) Percent change for each free parameter (either horizontal shift or gain) from the static condition. Statistical significance calculated by Wilcoxon signed rank test (*: $p < 0.05$, **: $p< 0.01$). Significance labels are the same as in Figure 3.4 Error bars represent mean ± SEM

20; Figure 3.5E, left). Changes in horizontal offset in other cell types were smaller, although they were still significant in On parasol cells for both motion and random conditions (p-value: motion, 2.5 x 10-2 ; random, 8.5 x 10-3, n = 14; Figure 3.5E, left).

Broad thorny cell changes in gain were widely variable across cells, with some showing sizable shifts (Figure 3.5E, right). While gain changes were not significant when the surround conditions were considered individually, the gain of the combined surround conditions differed significantly from the static surround condition. Gain changes in other cell types were smaller, although the gain differed significantly from baseline for Off parasol and Off smooth cells (Off parasols: p = 3.9 x 10^{-3} for motion and 2.0 x 10^{-3} for random, n= 10; Off smooth monostratified cells: p = 2.7 x 10^{-2} for motion and 3.4 x 10^{-2} for random, n = 12; Figure 3.5E, right).

3.3.4 Facilitation in On smooth monostratified cells persists following motion offset

To determine whether the facilitation in the On smooth monostratified cell to surround motion persisted after motion offset, we presented a grating in a cell's receptive-field surround that was either stationary or moving (Figure 3.6A). Following the offset of the stationary or moving grating,

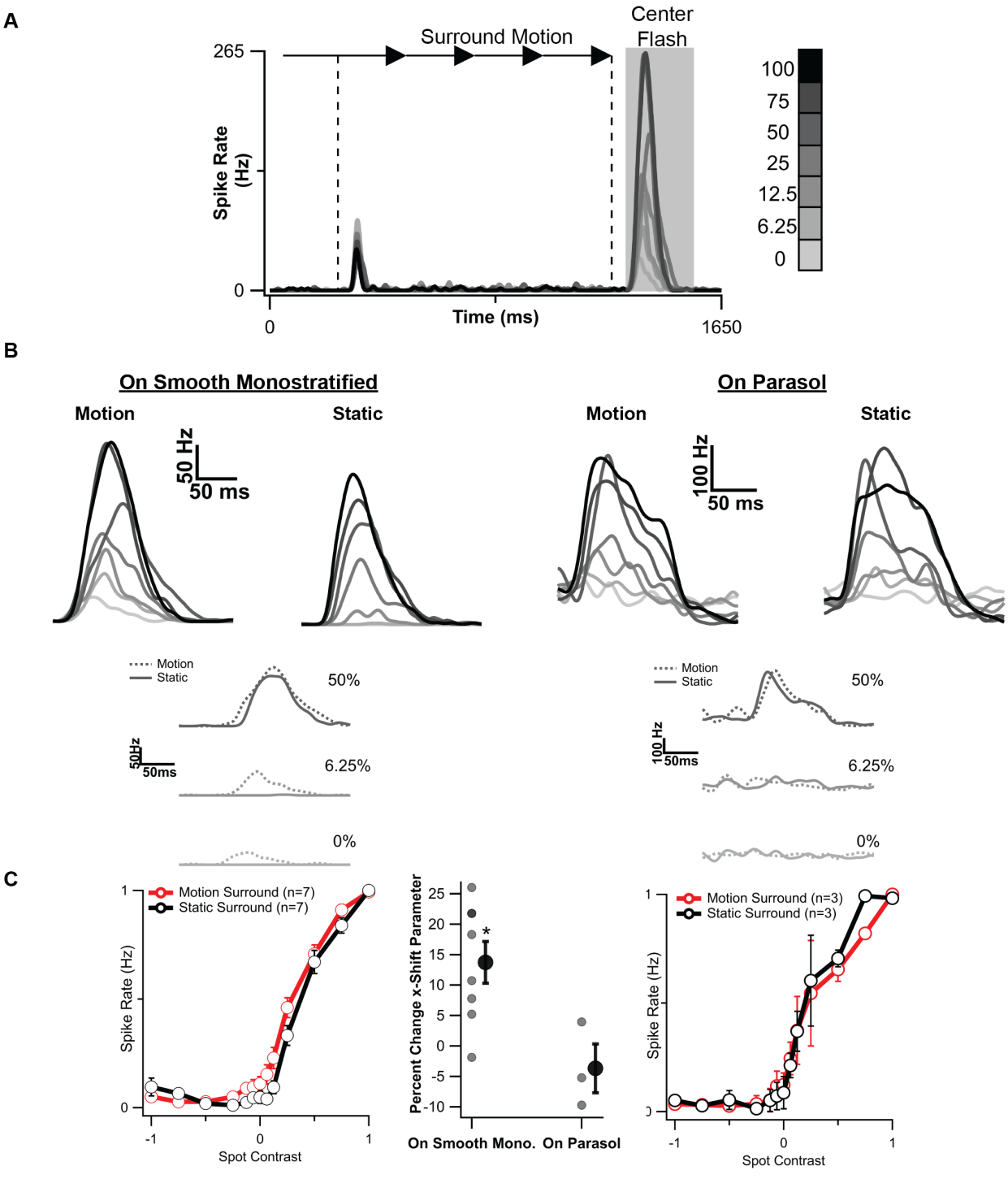
A
Surround Motion
Center Flash
265
0
Spike Rate (Hz)
Time (ms)
0
1650
100
75
50
25
12.5
6.25
0
B
On Smooth Monostratified
On Parasol
Motion
Static
Motion
Static
50 Hz
50 ms
100 Hz
50 ms
Motion
Static
50%
6.25%
0%
50Hz
50ms
Motion
Static
50%
6.25%
0%
100 Hz
50ms
C
Motion Surround (n=7)
Static Surround (n=7)
Spike Rate (Hz)
Spot Contrast
Percent Change x-Shift Parameter
On Smooth Mono.
On Parasol
Motion Surround (n=3)
Static Surround (n=3)
Spike Rate (Hz)
Spot Contrast

Figure 3.6: The effects of surround motion persist following motion offset. A) Stimulus sequence and corresponding example responses of the On smooth monostratified cell to center spots of increasing contrast. The surround contains either a drifting grating or stationary grating, depending on stimulus condition. The curve gray-scale value corresponds to percent contrast from a mean luminance. B) Enlarged view of example spike rates for motion or static conditions for On smooth monostratified and On parasol cell types C) Normalized contrast response functions for On smooth monostratified (left) and On parasol cells (right) following the moving and static surround conditions. The center panel plots the change in the horizontal offset for the moving grating relative to the stationary grating as calculated in Figure 3.5 (*: $p < 0.05$). Error bars represent mean ± SEM.

a spot was presented over the receptive-field center to measure the corresponding contrast-response function. For On smooth monostratified cells, the contrast-response function following the moving grating showed a leftward shift along the x-axis relative to the stationary grating (Figure 3.6). This persistent leftward shift indicates that facilitation from motion in the receptive-field surround persists following motion offset (Figure 3.6C). On parasol cells did not show such a shift.

To measure the extent of the response shift for each cell type after surround motion, we used a similar nonlinearity modeling paradigm to that in Figure 3.5. The horizontal offset parameter changed significantly for flash responses following surround motion compared to conditions with a static surround ($p = 1.5 \times 103.5$, $n = 8$; Figure 3.6C, middle). In contrast, the On parasol cell did not show a significant horizontal offset (Figure 3.6C, middle) or change in gain (data not shown). This finding indicates that facilitation from surround motion can persist following motion offset. This may contribute to visual processing in behaviorally relevant ways by increasing responsiveness in these cells following wide-field motion such that produced by ballistic eye movements.

3.4 Discussion

A central pursuit of systems neuroscience is to understand how circuit structure shapes the computational properties of neural circuits. Here, we demonstrate that the parallel output pathways in the primate retina show a wide diversity in the strengths and properties of their receptive-field

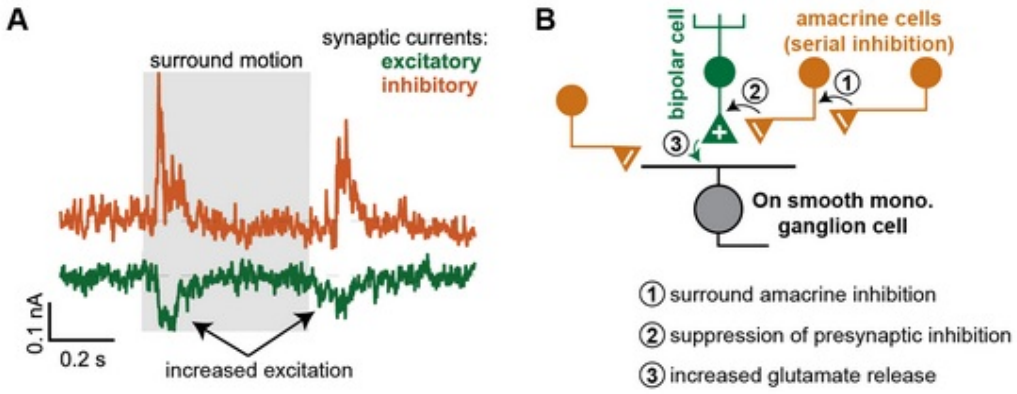

Figure 3.7: Circuit model for surround facilitation in On smooth monostratified cells. A) Synaptic current recordings from an On smooth monostratified ganglion cell. A moving grating was presented to the receptive-field surround while a constant gray stimulus was presented over the center region. Shaded region indicates period of surround motion. Inward excitatory synaptic currents were observed at motion onset and offset, consistent with surround modulation of presynaptic glutamate release from bipolar cells. B) Serial inhibition circuit model for generating surround facilitation that is consistent with synaptic recordings in (A). An amacrine cell located in the receptive-field surround inhibits another amacrine cell, which, in turn, provides inhibition to bipolar cells that provide excitatory synaptic input to a On smooth monostratified cell. Activation of the surround amacrine cell inhibits the second amacrine cell, which then produces disinhibition at the level of the bipolar cell resulting in an increased glutamate release onto the ganglion cell dendrites.

surrounds. This heterogeneity in receptive-field surrounds contributes to a diversity in computational properties and stimulus selectivities across these ganglion cell pathways. At one end of the spectrum, the strongly suppressive surround of the broad thorny ganglion cell produces similar properties to the object-motion-sensitive cells found in other vertebrate retinas (Figures 3.2, 3.4; [66, 141, 201, 187]). At the other end of the spectrum, the surround of the On smooth monostratified cell is suppressive for stationary stimuli and facilitatory for motion, a retinal property that, to our knowledge, is unique to primates (Figures 3.1, 3.2, 3.4 - 3.6).

3.4.1 Diversity of receptive-field surround strength in the primate retina

We observed a wide diversity in both the strength of receptive-field surround antagonism and in the functional consequences of the surround across ganglion cell types (Figures 3.1-3.6). Broad thorny

and On smooth monostratified cells appear to bookend much of the range, but the effects of spatial correlations on ganglion cell spike output formed a continuum across the cell types tested rather than falling into two distinct operating modes (Figure 3.3). This variability in surround effects likely arises from the ways in which the many amacrine cell types interact with bipolar cells, ganglion cells, and with one another. However, the properties of these amacrine cells and their interactions with other circuit elements is only beginning to be understood [66, 67, 17, 64, 177, 63].

3.4.2 Source of surround facilitation in On smooth monostratified cells

The component of the receptive-field surround arising in horizontal cells in the outer retina is shared by all ganglion cell types [31, 202]. Thus, the distinct effects of surround activation and surround motion on these cell types likely arises from differences in surround structure formed by amacrine cells in the inner retina [58, 56]. For example, serial inhibition by amacrine cells is an established circuit motif that could explain the surround facilitation observed in On smooth monostratified cells (Figure 3.5). Serial inhibition involves two different amacrine cell types – one type directly inhibits bipolar cells that provide excitatory synaptic input to ganglion cells and/or the ganglion cells themselves (Figure 3.7). This amacrine cell is, in turn, inhibited by another amacrine cell type that, in the case of the On smooth monostratified cell, would be located in the receptive-field surround. Stimulating this second amacrine cell with motion in the surround, would then inhibit the amacrine cell and would produce disinhibition at the level of the bipolar cells and/or ganglion cell. While serial inhibition is the most parsimonious explanation, future studies are needed to understand the circuit motifs and neural mechanisms that govern visual computations in On smooth monostratified cells and in the primate retina more generally.

3.4.3 Implications of surround motion sensitivity during natural viewing

Correlated motion can occur across multiple spatial scales during natural vision. For example, self motion caused by eye movements or an observer's movements through the scene produce correlated motion over large distances. By contrast, local motion correlations can be produced when an object moves relative to the observer, and the length of those correlations on the retina depend on the object's size and its distance from the observer. Thus, sensitivity to these correlations can significantly benefit sighted animals in navigating the environment, avoiding predators, capturing prey, and other important functions.

Our experiments revealed a wide range of sensitivities to spatial motion correlations (Figure 3.3). The spike output of broad thorny ganglion cells was strongly suppressed by medium and long-range correlations, and other ganglion cell types were likewise suppressed by these correlations, though to a lesser extent. Still other cells, such as On smooth monostratified cells, showed little sensitivity to the spatial extent of motion correlations, and continued to respond strongly for motion with long-range correlations. Natural images do not have a characteristic size or scale, in large part because an object of a given physical size can appear at any distance from an observer. The same consideration should apply to motion, and hence the highly diverse sensitivities to motion correlation length could help provide an efficient encoding of the range of motion signals encountered in natural vision.

3.4.4 The broad thorny as a candidate object-motion sensitive cell in primates

Detection of an object moving relative to an animal's own motion is an important, behaviorally relevant neural computation. Ganglion cells have been found in the salamander, rabbit, and mouse retinas that show this type of motion selectivity [66, 141, 201, 25, 187][141][201]. Our experiments reveal similar stimulus selectivity for broad thorny ganglion cells – they show strong surround

suppression, slow response kinetics, and respond most robustly when differential motion occurs between the center and surround regions of the receptive field (Figures 3.1-3.3). In addition to these similar light response properties, the dendritic morphology and stratification within the retinal neuropil of broad thorny cells resembles that of object-motion sensitive cells found in other species [30, 141].

Broad thorny cells may also share a common circuit motif with object-motion sensitive cells in other species. In mice, object-motion sensitive ganglion cells receive excitatory synaptic input from vGlut3-positive amacrine cells, and this synaptic input is a key feature to the motion sensitivity of these cells [201, 187]. Recent electron microscopic reconstructions of broad thorny ganglion cells in macaque retina have shown that these cells receive synaptic contacts from an amacrine cell that resembles vGluT3-positive amacrine cell in the baboon retina34,35. However, more work is needed to determine the potential similarities and differences between the broad thorny circuit and the object-motion sensitive cells found in other species.

3.4.5 Feature selectivity in the dorsal visual pathway of primates

The classical center-surround receptive field has been a foundational concept in sensory neuroscience for more than a century [9, 193, 13, 10]. Indeed, with few exceptions, models of the early vision in primates have been based on the idea that retinal responses can be adequately described as a simple weighted sum of the stimuli falling within the receptive-field center and surround regions [28, 203, 204, 86]. However, over time, findings in several sensory systems, including the vertebrate retina, have challenged this traditional model of receptive-field organization [17, 205, 131, 206–209].

Notably, in the medial temporal (MT) area of the primate cortex, cells have been found with center-surround receptive fields akin to those reported here for the broad thorny and On smooth monostratified ganglion cells – motion in the receptive-field surround strongly suppressed the responses of one set of cortical neurons and facilitated the responses of another set of neurons [131].

Other aspects of motion processing, such as motion direction, similarly appear to occur both at the retinal and cortical levels in primates [134, 210] and non-primates [118].

The parallel computation of motion in the retina and cortex likely indicates its ethological importance, such as its roles in reflexive eye movements that center the fovea on specific image structure and in higher level computations such as parsing a scene into objects. Here, we show that interactions of the receptive field center and surround in primate retinal ganglion cells are not restricted to spatial filtering, but instead also contribute to the extraction of visual motion.

3.5 Methods

3.5.1 Tissue preparation

Macaque monkey eyes were enucleated and hemisected, and vitreous humor was removed by hand. Retinas were dissected out of the eye under infrared light and kept in a *sim*32-34°C Ames bicarbonate solution (Sigma) bubbled with 5% CO2 and 95% O2. Before experimental use, retinas were dark adapted for at least 1 hour. Pieces of pigmented epithelium-attached retina (2-8 mm, *sim*10-30° foveal eccentricity at temporal or nasal positions relative to the eye) were mounted ganglion cell-side up onto a poly-D-lysine-coated coverslip (BD Biosciences) and placed in a dish perfused at *sim*6-8 mL min-1 warmed (32°C) Ames solution. Tissue was illuminated at 940 nm for visualization.

3.5.2 Electrophysiology and Data Analysis

To obtain spiking responses from ganglion cells, cell-attached and extracellular recordings were performed with borosilicate glass pipettes filled with Ames solution. Data was acquired at 10 KHz using a Multiclamp 700B amplifier (Molecular Devices) and Symphony data acquisition software.

All analysis of spiking data was performed using customized scripts in MATLAB (R2019 and R2022b, Mathworks). Wavelet filtering was used to amplify spikes relative to the noise. Spike detection was performed using k-means clustering on spike waveforms or by choosing a manual threshold of standard deviation relative to baseline.

3.5.3 Visual Stimulation

Stimuli were displayed on either an 800 x 600 pixel OLED monitor (eMagin) or an 1140 x 912 Lightcrafter 4500 digital light projector (Texas Instruments) before being focused via a microscope objective onto the photoreceptors of each retinal specimen. Light levels were in the mid- to high- photopic range (4 x 10^3 to 4 x 10^4 cone photoisomerizerizations s^{-1}). Symphony (http://symphony-das.github.io) and Stage (http://stage-vss.github.io) software packages were used to generate visual stimuli. Stimuli were presented at 60 Hz refresh rates.

For each recording, stimuli were centered on the receptive field center using a sinusoidally modulated bar in either horizontal or vertical orientation (bar size, 50 x 1000 μm). The peak response along each orientation determined x and y coordinates used to center stimuli. We then determined the size of the receptive field center using an annulus of increasing inner diameter. The inner diameter at which the cell either reversed its firing phase (that is, from an onset to an offset response) or stopped responding was determined as the inner diameter of the receptive-field surround. An additional ring of mean luminance of 25-50 μm width was used as a buffer between center and surround (see Supplementary Figure 3.8).

To ensure that motion stimuli caused strong spiking responses in the parasol, On smooth monostratified, and broad thorny cells, we calculated interspike intervals to measure momentary firing rates during center-only conditions for stimuli in Figure 3.2. We calculated the percentage of interspike intervals with durations less than 10 ms, reflecting instantaneous spike rates of >100 Hz. Spiking intervals at this scale are near the refractory limit for spiking, indicating a robust response. The percentage of interspike intervals at less than 10 ms for each cell type were 42% and 43% for

the On parasol (grating and texture conditions), 46% for both for the Off parasol, 32% and 4.6% for the On smooth monostratified cell, and 40% and 26 percent for the broad thorny cell.

Our temporal flicker stimulus was generated by drawing contrasts from either a gaussian distribution with variance of 0.3 or a binary distribution. Linear filters were computed as cross correlations of the flicker stimulus and its responses22,52. Input-output curves were generated by convolving the linear filter with the stimulus to create a generator signal (filtered contrast) that was compared against the spiking response to each surround stimulus condition (ganglion cell output). The input-output nonlinearities were modeled in Figures 3.5 and 3.6 as cumulative Gaussian distributions23:

$$O(I) = \varepsilon + \frac{\alpha}{2\pi}\int_{-\infty}^{I} e\frac{-(\beta t+\gamma)}{2}dt \tag{3.1}$$

where I is filtered input contrast. Four parameters control the shape of the resulting curve. The curve is scaled to its maximum response α, the slope of the curve is generated by β, horizontal offset is controlled by γ, and vertical offset is controlled by ε. To compare whether nonlinearities shifted predominately along the input axis (horizontally) or by the gain of the response (slope of the curve) nonlinearities for each stimulus condition of Figure 3.4 were fit together for three of the parameters and allowed to be fit independently by either β or γ. Performance of fits relative to the data for each fit curve type (horizontal shift change or gain change) was determined by comparing a mean-squared error measure.

The motion preference index used in Figure 3.2 is given by the equation below:

$$Motion\ Preference\ Index = \frac{R_X - R_{center}}{R_X + R_{center}} \tag{3.2}$$

3.6 Supplementary Videos

Supplementary videos can be found on YouTube:

Video 1: Grating

Video 2: Texture

Video 3: Surround Motion

Video 4: Dots (spatial correlation stim)

3.7 Supplementary Figures

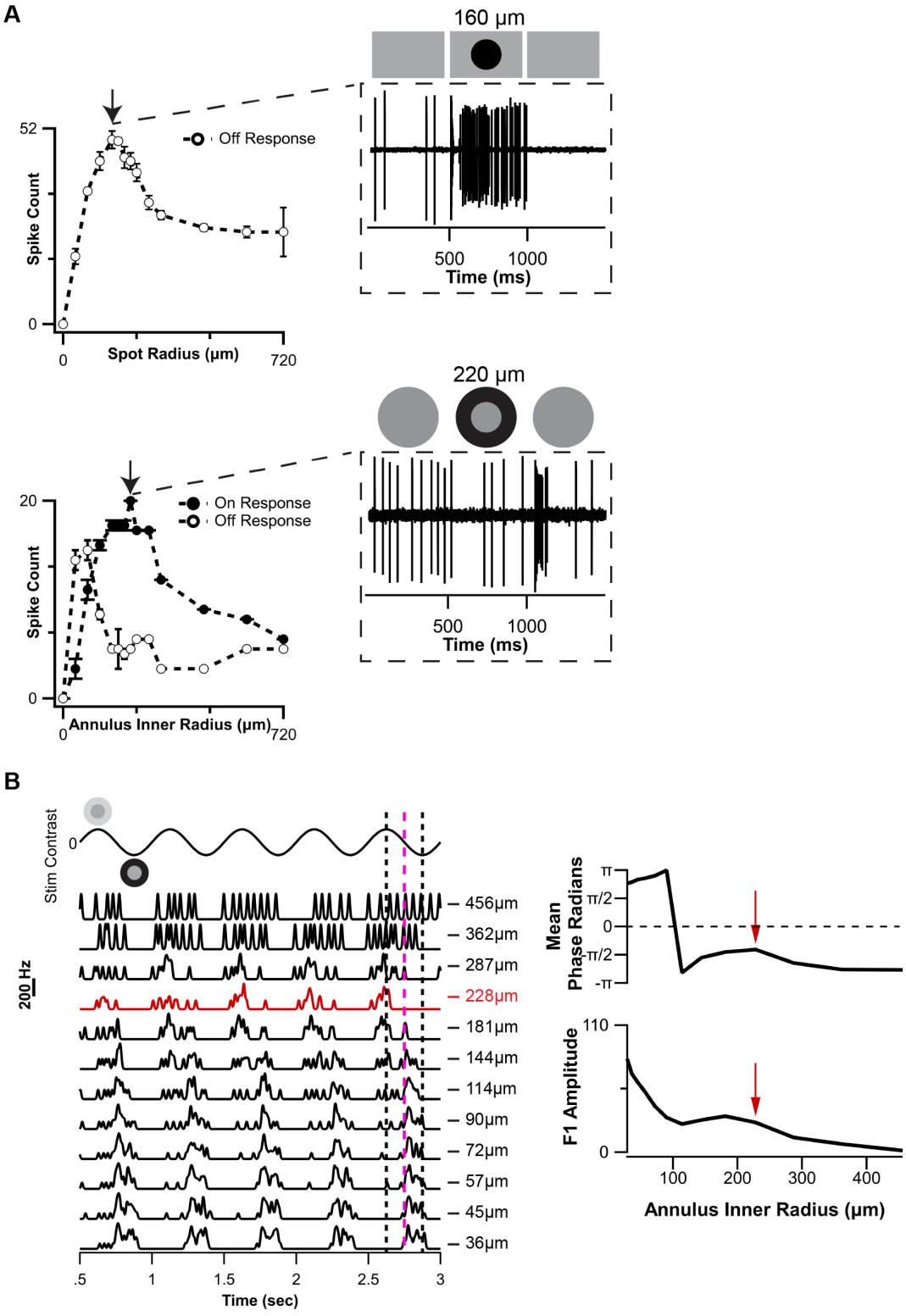
A
160 µm
52
Spike Count
0
Off Response
0
Spot Radius (µm)
720
500
1000
Time (ms)
220 µm
20
Spike Count
0
On Response
Off Response
0
Annulus Inner Radius (µm)
720
500
1000
Time (ms)
B
Stim Contrast
0
200 Hz
456µm
362µm
287µm
228µm
181µm
144µm
114µm
90µm
72µm
57µm
45µm
36µm
.5
1
1.5
2
2.5
3
Time (sec)
Mean Phase Radians
π
π/2
0
-π/2
-π
F1 Amplitude
110
0
100
200
300
400
Annulus Inner Radius (µm)

Figure 3.8: Determining Extent of Receptive Field Center with Spots and Annuli. Two stimulus paradigms were used to separate ganglion cell receptive field centers from surrounds. A) Top: Spots of multiple sizes (40 - 720 μm radius) delivered to an Off smooth monostratified cell. Top Inset: Spike response to a 160 μm radius negative contrast spot. Bottom: Annuli of multiple sizes (40 - 720 μm inner radius) delivered to the same cell. Bottom Inset: Spike response to a 220 μm radius negative contrast annulus. Arrows indicate point to spot response on the left panel to which inset panel corresponds. B) Annuli of multiple sizes change their contrast relative to the center on a 2 cycles/sec sinewave trajectory. Left: mean PSTHs for each annulus inner diameter are shown for cell in (A). The magenta dotted line indicates the halfway point of the final cycle. Block dotted lines on either side of the magenta line indicate contrast peak of each cycle half. Right: phase data indicates cycle preference (increase or decrease in contrast as indicated by spiking output) for each annulus inner radius. Arrow indicates phase shift of red trace in left panel.

Chapter 4

Neural Sensitization Improves Encoding Fidelity in the Primate Retina

The study presented in this chapter has been published as: Todd R. Appleby and Michael B. Manookin (2019). Neural Sensitization Improves Encoding Fidelity in the Primate Retina. *Nature Communications* 10, 4017

4.1 Summary

An animal's motion through the environment can induce large and frequent fluctuations in light intensity on the retina. These fluctuations pose a major challenge to neural circuits tasked with encoding visual information, as they can cause cells to adapt and lose sensitivity. Here, we report that sensitization, a short-term plasticity mechanism, solves this difficult computational problem by maintaining neuronal sensitivity in the face of these fluctuations. The numerically dominant output pathway in the macaque monkey retina, the midget (parvocellular-projecting) pathway, undergoes sensitization under specific conditions, including simulated eye movements. Sensitization is present in the excitatory synaptic inputs from midget bipolar cells and is mediated by presynaptic disinhibition from wide-field amacrine cells. Direct physiological recordings and a computational model indicate that sensitization in the midget pathway supports accurate sensory encoding and prevents a loss of responsiveness during dynamic visual processing.

4.2 Introduction

The fundamental constraints on sensory coding require that neural circuits adjust their outputs based on the statistical properties of their recent inputs [211, 206, 212]. Neurons respond to dynamic inputs using two distinct strategies—adaptation and sensitization. Adapting cells respond to strong stimulation by decreasing their sensitivity and this decrease in responsiveness can persist for several seconds after the stimulus intensity decreases [79, 213, 78, 212, 80, 77]. Thus, adapting cells are relatively insensitive to weak stimuli occurring during these transition periods. Sensitizing cells show the opposite pattern—increasing their responsiveness at these transitions [90, 92, 91]. For this reason, adaptation and sensitization are commonly thought to constitute opposing and complementary forms of short-term neural plasticity [90, 92].

This hypothesis requires that a sensitizing cell type have an adapting counterpart that encodes common information [90]. However, this constraint could potentially decrease the amount of information that can be encoded in an neural ensemble and increase the metabolic demands on a sensory tissue [212, 214]. Nowhere is the need for metabolic and encoding efficiency more evident than in the macula of the primate retina where the tight packing of cells places space and metabolic resources at a premium. Alternatively, adaptation and sensitization might be signatures of fundamentally distinct neural coding strategies [215]. Further, these alternative hypotheses are not mutually exclusive—adapting and sensitizing cells could mirror each other in some species and neural pathways and not in others, depending on the particular coding and metabolic constraints in those systems [206, 212, 214, 216]. However, given that neural sensitization was only recently discovered, relatively little is known about its roles in neural information processing.

To address this issue, we recorded from five types of output neurons in the macaque monkey retina—broad thorny (koniocellular-projecting), On and Off parasol (magnocellular-projecting), and On and Off midget (parvocellular-projecting) ganglion cells. These cells have well described roles in visual processing and no known functional counterparts. We studied how these cells re-

sponded to global fluctuations in contrast and other stimulus statistics. We report that whereas broad thorny and parasol cells strongly adapted, midget cells sensitized—increasing their responsiveness to certain types of visual stimulation, including simulated eye movements. Synaptic current recordings revealed that this increased sensitivity was present in the excitatory input from midget bipolar cells and was mediated by presynaptic disinhibition. The mechanism that increased sensitivity in midget cells originated in the receptive-field surround and showed a spatial extent in excess of 0.5mm (>2.5 degrees). A computational model based on synaptic input recordings further indicated that this increase in sensitivity greatly enhanced the fidelity of encoding natural scenes. Moreover, the lack of an adapting counterpart to midget cells indicated that sensitizing circuits performed a distinct role in primate retina relative to that observed in other vertebrate neural systems [90, 92, 91, 217].

4.3 Results

4.3.1 Midget ganglion cells exhibit contrast sensitization/facilitation

The midget pathway of the primate retina is commonly believed to lack short-term plasticity mechanisms such as contrast gain control. This belief is based on reports that midget cells do not exhibit noticeable changes in responsiveness following transitions from high to low-contrast regimes [87, 85]. The assay used to measure adaptation was a sinusoidally modulated drifting grating in which contrast was high for several seconds after which it transitioned to low contrast. Following the offset of high-contrast stimulation, midget cells did not exhibit a noticeable change in spiking relative to the period prior to the onset of high-contrast stimulation. This was in stark contrast to the behavior observed in parasol ganglion cells. Parasol cells showed a strong and persistent depression in spiking following the offset of high contrast—behavior consistent with cells undergoing contrast adaptation [87, 85].

The grating stimulus that did not elicit visible adaptation in midget cells was comprised of a spatial frequency tuned to the size of each cell's receptive-field center, which is narrower than many other retinal cell types. Thus, if plasticity in the midget pathway depended on mechanisms with broader spatial tuning, this assay would not have engaged these mechanisms.

To determine whether short-term plasticity in the midget pathway depends on the spatial properties of the stimulus, we repeated this assay while varying the spatial tuning of the gratings. Consistent with previous reports [87, 85], midget cells did not exhibit a notable change in firing following the offset of a high contrast, high spatial frequency grating relative to the period that preceded high-contrast stimulation (Figure 4.1A). To determine whether this lack of either adaptation or sensitization persisted across a range of stimulus conditions, we varied the spatial frequency content of the drifting gratings. Following the offset of low spatial frequency gratings, most midget cells showed an increase in spiking relative to the period preceding grating onset (Figure 4.1B). This increase in spiking following high contrast is characteristic of the contrast sensitization observed in other vertebrate retinas [90, 92, 91]. The presence of sensitization at low spatial frequencies suggested that it depended on the ability to engage elements in the midget cell receptive field with broad spatial tuning relative to the midget bipolar cell.

To ensure that this increase in spiking was not an artifact of the phase of the grating at the offset of high contrast, we randomized the grating phase on each trial in several cells. Indeed, randomizing the grating phase did not produce significant changes at grating offset relative to cells recorded with a fixed phase (midget cell p-value, 0.53; n=12 midget cells; parasol cell p-value, 0.3; n=14 parasol cells; Wilcoxon rank sum test).

4.3.2 Stimulus dependence of contrast sensitization in midget ganglion cells

Our next goal was to determine how this putative wide-field component of the midget cell receptive field contributed to contrast coding. To accomplish this goal, we sought a more spatiotemporally precise assay of sensitivity following wide-field adaptation. Contrast tuning of parasol and midget

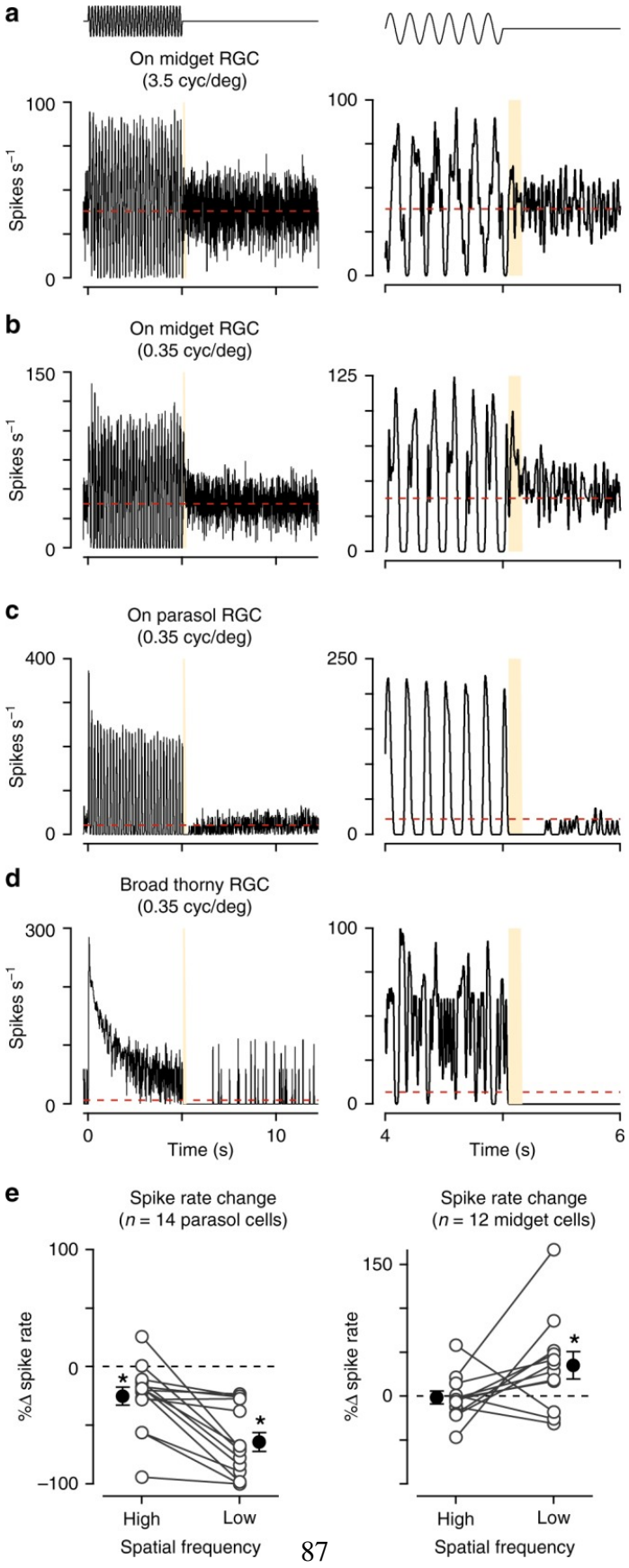
a
On midget RGC
(3.5 cyc/deg)
100
0
Spikes s−1
100
0
b
On midget RGC
(0.35 cyc/deg)
150
0
Spikes s−1
125
0
c
On parasol RGC
(0.35 cyc/deg)
400
0
Spikes s−1
250
0
d
Broad thorny RGC
(0.35 cyc/deg)
300
0
Spikes s−1
100
0
0
10
Time (s)
4
6
Time (s)
e
Spike rate change
(n = 14 parasol cells)
100
0
−100
%Δ spike rate
*
*
High
Low
Spatial frequency
Spike rate change
(n = 12 midget cells)
150
0
%Δ spike rate
*
High
Low
Spatial frequency

Figure 4.1: Parasol and midget cells exhibit opposing forms of plasticity. (A) Spike rate in an On midget ganglion cell to a high spatial frequency grating presented for 5s (temporal frequency, 6Hz; spatial frequency, 3.5 cyclesdegree^{-1}). The spike rate immediately after grating offset showed little change relative to the period prior to grating onset. Right: Zoom of transition period. (B) Spike responses from the same cell as in a to a low spatial frequency grating (0.35 cycles degree^{-1}). Spiking showed a transient increase following the offset of high contrast, consistent with contrast sensitization. (C) Spike rate in an On parasol ganglion cell to a low spatial frequency drifting grating (0.35 cycles degree^{-1}). After the offset of high contrast, the spike rate declined below the level prior to grating onset (red dashed line). (D) Same as (A) in a broad thorny (On-Off type) ganglion cell. (E) Change in spike rate for the period directly after grating offset relative to period prior to grating onset in parasol (left) and midget ganglion cells (right). Spiking in parasol cells was significantly reduced for both spatial frequencies ($p<6.0\times10^{-3}$; n=14 cells) and significantly increased in midget cells for the low spatial frequency grating ($p=3.4\times10^{-2}$; n=12 cells). Statistical significance calculated using the Wilcoxon signed rank test.

cells was determined with spots centered on the receptive field. Responses were measured in isolation (unadapted condition) or 50–100ms following the offset of an adapting stimulus (adapted condition). The adapting stimulus was a large, high-contrast spot modulated at 12–30Hz (diameter, 730μm). Presentations of the adapted and unadapted stimuli were interleaved to account for any potential variability in cellular responses over time.

Our next goal was to determine how this putative wide-field component of the midget cell receptive field contributed to contrast coding. To accomplish this goal, we sought a more spatially and temporally precise assay of sensitivity following wide-field adaptation. Contrast tuning of parasol and midget cells was determined with spots centered on the receptive field (duration, 0.1 s; parasol diameter, 80-200 μm; midget diameter, 40-80 μm). Contrast responses were measured in isolation (unadapted condition) or 50-100 ms following the offset of an adapting stimulus (adapted condition). The adapting stimulus was a large, high-contrast spot modulated at 20-30 Hz (diameter, 730 μm; contrast, 0.5-1.0, duration, 1.25 s). Presentations of the adapted and unadapted stimuli were interleaved to account for any potential variability in cellular responses over time.

Example spike responses to this stimulus paradigm are shown in Figure 4.2 Parasol cells increased their spike rate at the onset of the adapting stimulus and the spike rate quickly decreased

to a steady-state rate by $\sim$0.25s. Test flashes presented after the offset of the adapting stimulus evoked fewer spikes relative to the unadapted control (Figure 4.2A), resulting in a decrease in gain, defined as the steepest slope of the contrast-response function [87, 85, 89]. Both of these patterns—a transient increase in spike rate following the transition to high contrast and a decrease in spiking after the transition from high contrast—are characteristic of cells undergoing contrast adaptation [79, 78, 218]. This result confirms previous reports that parasol cells readily adapt to changes in contrast (Figure 4.2G; [87, 85, 89]).

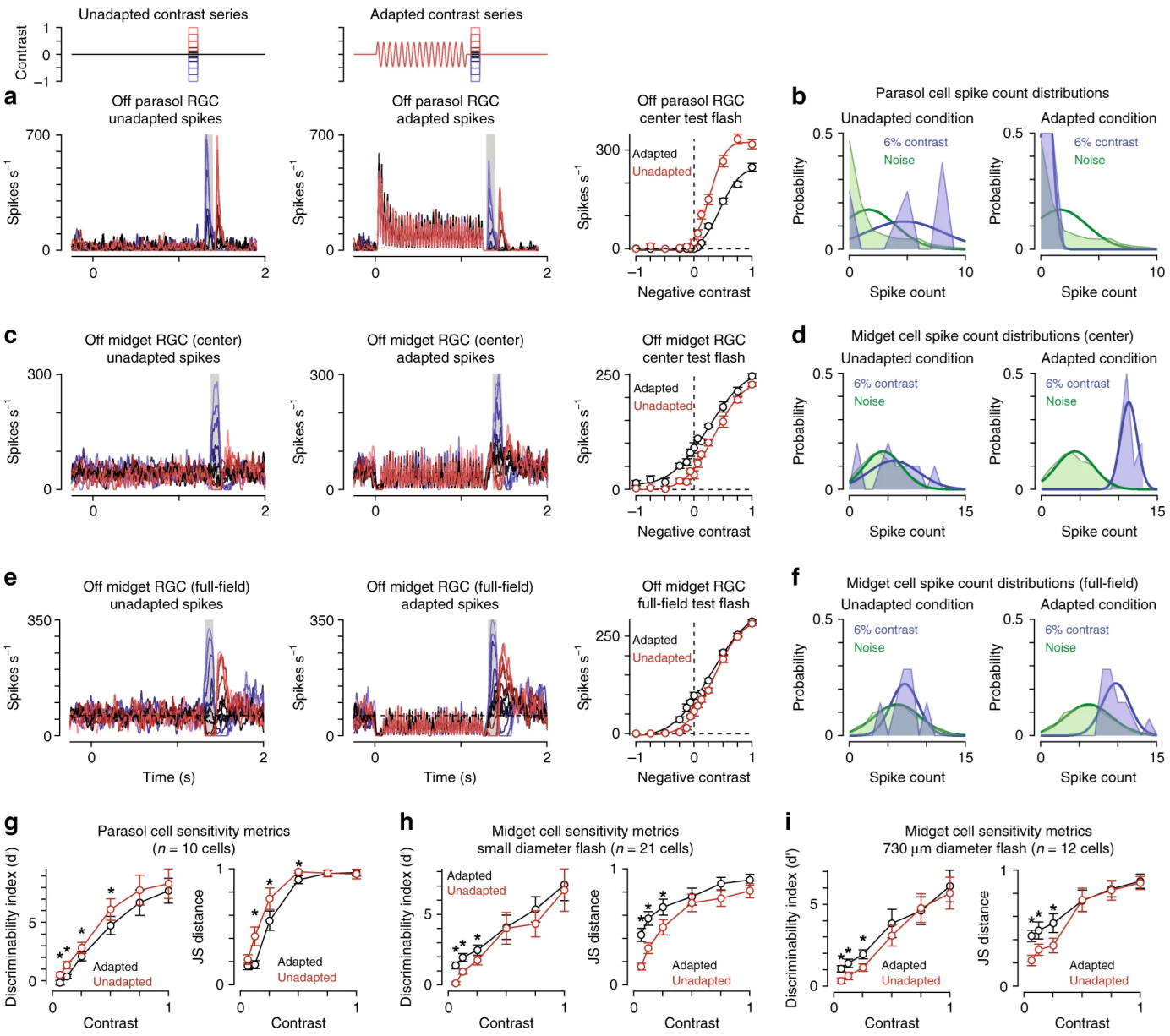
Unadapted contrast series
Adapted contrast series
Contrast
a
Off parasol RGC unadapted spikes
Off parasol RGC adapted spikes
Off parasol RGC center test flash
Adapted
Unadapted
Spikes s−1
Negative contrast
b
Parasol cell spike count distributions
Unadapted condition
Adapted condition
6% contrast
Noise
Probability
Spike count
c
Off midget RGC (center) unadapted spikes
Off midget RGC (center) adapted spikes
Off midget RGC center test flash
d
Midget cell spike count distributions (center)
e
Off midget RGC (full-field) unadapted spikes
Off midget RGC (full-field) adapted spikes
Off midget RGC full-field test flash
Time (s)
f
Midget cell spike count distributions (full-field)
g
Parasol cell sensitivity metrics (n = 10 cells)
Discriminability index (d')
JS distance
Contrast
h
Midget cell sensitivity metrics small diameter flash (n = 21 cells)
i
Midget cell sensitivity metrics 730 µm diameter flash (n = 12 cells)

Figure 4.2: Midget ganglion cells display contrast sensitization. (A) Spike responses from an Off parasol ganglion cell to a series of spots centered over the receptive field. Spots were either presented alone (left) or 50ms following the offset of an adapting stimulus (middle). Shaded regions indicate sampling windows. Right: Average spike rate across the shaded regions. The wide-field adaptation evoked a decrease in the slope (gain) of the contrast-response curve (black) relative to the unadapted control condition (red). (B) Spike count distributions for the Off parasol cell in (A) to a -6% contrast flash and the noise condition in which a flash was not presented (i.e., 0% contrast). The adapting stimulus decreased spiking at low contrast and shifted the low-contrast distribution toward the noise distribution (right) relative to the unadapted condition (left). (C) Same as (A) for an Off midget ganglion cell. Right: Average spike rate across the shaded regions. The wide-field adaptation evoked a leftward shift in the contrast-response curve (black) relative to the unadapted control condition (red). (D) Same as (B) for the Off midget cell in (C). The adapting stimulus increased spike counts at low contrast, increasing the separation between the low-contrast and noise distributions. (E) Spike responses of an Off midget cell to wide-field test flashes in the absence (left) or presence (middle) of the adapting stimulus. (F) Same as (D) for the Off midget cell in (E). (G) Discriminability index (left) and Jensen-Shannon distance (right) for preferred-contrast responses relative to background noise in parasol ganglion cells (n=10). (H) Sensitivity indices in 21 midget ganglion cells for small diameter test flashes. Discriminability index and Jensen-Shannon distance increased significantly at low contrast ($\leq$25%) following the adapting stimulus ($p<0.01$). (I) Sensitivity indices in 12 midget cells for wide-field test flashes. The adapting stimulus produced a significant increase in the Jensen-Shannon distance at low contrast (6%; $p=1.5\times10^{-3}$). Circles and bars indicate mean±SEM. Statistical significance calculated using the Wilcoxon signed rank test

Midget cells showed a different pattern—instead of reducing sensitivity as it did for parasol cells, the adapting stimulus significantly increased sensitivity in midget cells at low contrast (Figure 4.2H. To determine whether these effects differed between On and Off midget cells, we separately analyzed the sensitivity metrics for On and Off cells for this stimulus paradigm. Following the adapting stimulus, contrast sensitivity significantly increased relative to the unadapted control in both On and Off midget cells at contrasts 0.25 ($p<0.05$; Wilcoxon signed rank test), indicating that sensitization improved contrast sensitivity in both the On and Off midget pathways.

We next tested whether contrast sensitization varied with the size of the test flash by repeating the adaptation experiment with wide-field test flashes to measure the contrast tuning of midget cells (diameter, 730 μ m). Indeed, the adapting stimulus produced a significant increase in sensitivity relative to the unadapted condition at low contrast (Figure 4.2I). These data indicated that sensiti-

zation persisted for wide-field stimulation. We further tested the time course of the sensitization effect and found that it could be engaged with relatively brief periods of stimulation (0.25s) and persisted for ∼0.4s following the offset of high-contrast stimulation (Figure 4.3).

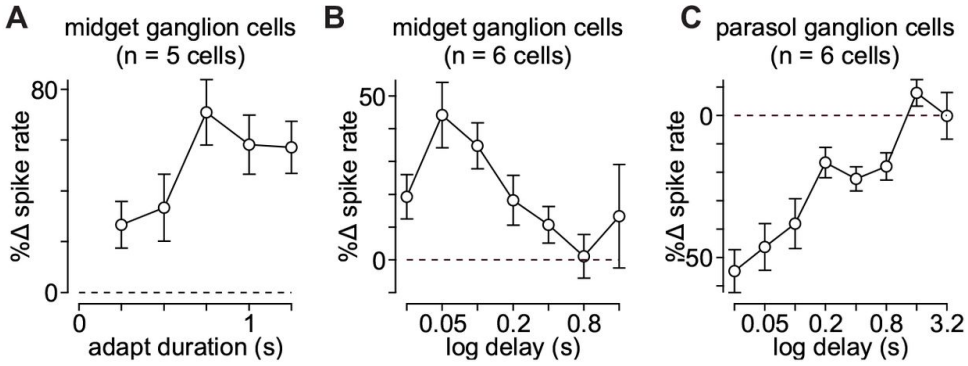

Figure 4.3: Time course of contrast sensitization and adaptation. (A) Change in spike rate for the adapted condition relative to unadapted control for adaptation periods (contrast, ±0.25–0.5; delay 0.05s). Adaptation period was varied between 0.25 and 1.25s (x-axis). The adapting stimulus produced a significant increase in spiking for each of the durations tested ($p<4.0\times10^{-3}$; n=9 cells). (B) Duration of contrast sensitization in midget ganglion cells. Test flashes (contrast, ±0.25–0.5) were presented at different delays (x-axis) following the offset of an adapting stimulus. Percent change in spike rate for the adapted condition relative to the unadapted condition is shown on the y-axis. Increase in spiking was statistically significant for delays ≤0.4s ($p<7.0\times10^{-3}$; n=11 cells). (C) Same as (B) for parasol ganglion cells. The adapting stimulus significantly reduced spiking at delays ≤0.8s ($p<7.0\times10^{-3}$; n=10 cells). Error bars indicate mean±SEM. Statistical analyses were paired and significance was calculated using the Wilcoxon signed rank test.

Collectively, the experiments described thus far indicated that mechanisms within the midget cell receptive-field surround strongly contributed to contrast sensitization. To determine whether the observed plasticity mechanisms persisted for surround stimulation alone, we repeated the adapting stimulus paradigm while restricting both the adapting stimulus and the test probe to the receptive-field surround. Just as with full-field adaptation, surround adaptation significantly improved sensitivity at low contrast (Figure 4.4). These results indicated that surround stimulation alone was sufficient to produce sensitization in midget cells. These data also indicated that the surround mechanism responsible for sensitization in the midget cells must be much larger than 160μm in order to exert the observed effects on spiking in midget cells.

To estimate the spatial extent of the surround mechanism mediating contrast sensitization, we repeated the surround adaptation experiment using mask diameters of 160–640μm in the same cell. Surround adaptation increased the spike output of midget cells to flashed annuli for mask diameters $\leq$480μm (Figure 4.4E). This increase in evoked spiking resulted in significant increases in sensitivity for a range of mask diameters (Figure 4.4F). These data indicate that this mechanism must have a spatial extent well in excess of 480μm in order to exert the observed effects on spiking in midget cells. This means that the sensitization mechanism we measured operates over spatial scales that are >10 times the size of the classical receptive-field center—the spatial extent of this effect narrows the candidate mechanisms to either horizontal cells in the outer retina or wide-field amacrine cells in the inner retina. Below, we present evidence that wide-field amacrine cells mediate contrast sensitization in the midget pathway.

4.3.3 Temporally uncorrelated stimuli reveal interactions between adaptive and sensitizing mechanisms

To measure the effects of spatially localized changes in stimulus variance, we presented a randomly flickering spot over the receptive field (Figure 4.5, top left). Cellular responses were modeled using the linear–nonlinear (LN) paradigm. Separate nonlinearities were calculated for the high-contrast condition, for the low-contrast region immediately following the transition from high to low contrast (low early; 100–600ms following the transition), and for the more sustained period of low-contrast stimulation (low late). Changes in gain (the steepest slope of the nonlinearity) and horizontal offset were calculated by scaling the low contrast nonlinearities to match the nonlinearity at high contrast (see Methods section) [89].

We measured responses from midget cells to the same stimulus protocol—the time-varying contrast trajectory was presented within a small spot over the receptive field (diameter, 40–80μm). As with the parasol cells, midget cells showed a reduction in gain that slowly recovered follow-

ing the transition to low contrast (Figure 4.5C,D). This pattern of gain changes was consistent with weak contrast adaptation in midget cells to continuous stimulation that was localized to the cells' receptive-field center and near surround. This result was surprising in the context of the other experiments presented thus far indicating that midget cells sensitized to stimulation of the receptive-field center+surround or of the surround alone. The differing results of these experiments and the noise experiments could arise from differences in the temporal frequency content of the stimuli—the stimuli eliciting sensitization were restricted to higher temporal frequencies (12–30Hz) while the noise stimuli were temporally broad-band, equally sampling frequencies up to the Nyquist limit of the display (30Hz). Another difference between these stimuli was their distinct spatial properties—the stimuli eliciting sensitization strongly modulated the receptive-field surround whereas the noise stimuli were primarily localized to the receptive-field center.

Parasol cells showed a reduction in gain during the transition to low contrast relative to the later period of low contrast (Figure 4.5A,H). Figure 4.5B illustrates the change in gain as a function of time for an example Off parasol cell. Following the transition to low contrast, the cell's gain increased to a steady-state value over the course of $\sim$1s. This result was again consistent with strong contrast adaptation in parasol cells.

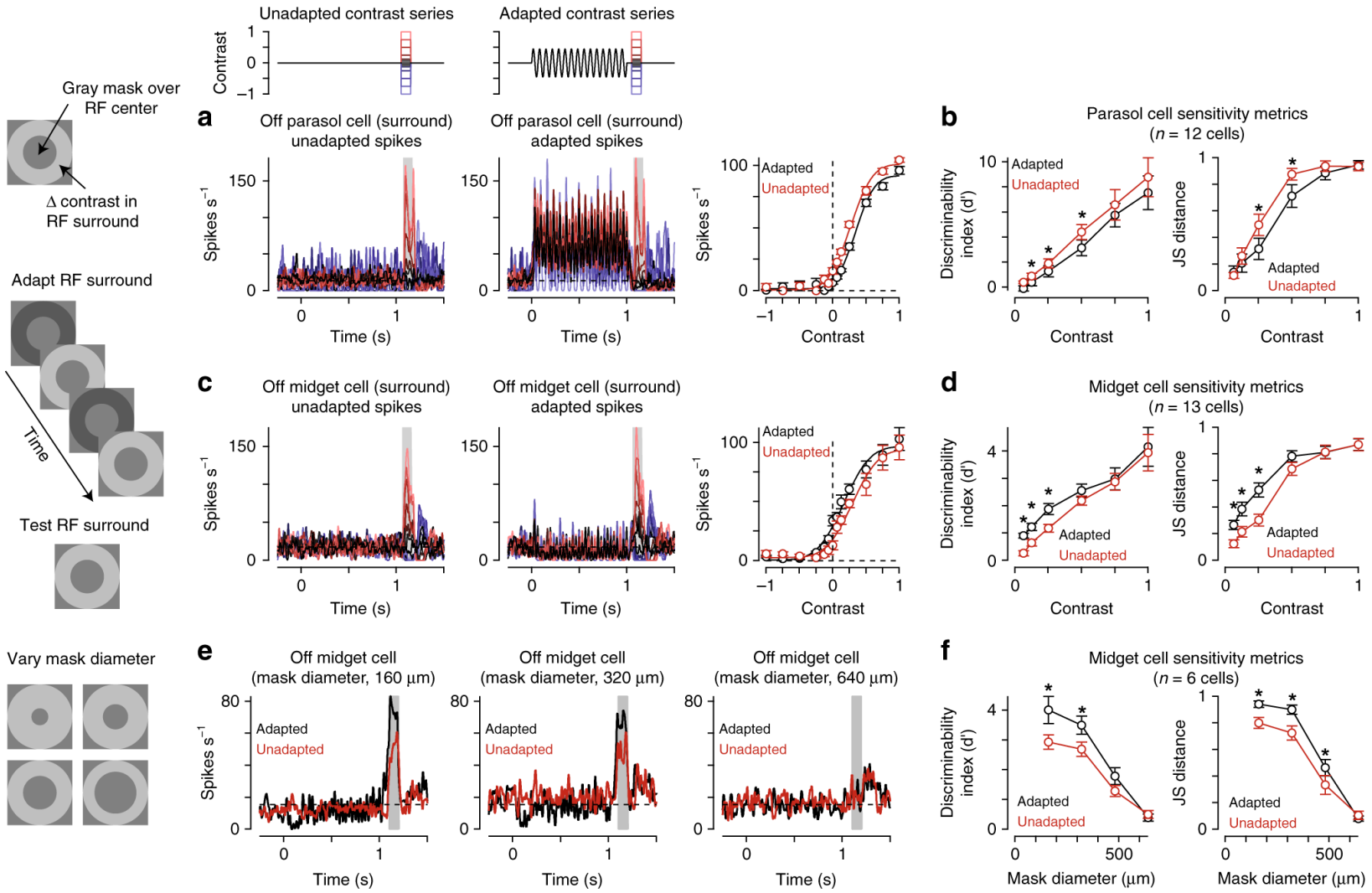
Unadapted contrast series
Adapted contrast series
Contrast
Gray mask over RF center
Δ contrast in RF surround
Adapt RF surround
Time
Test RF surround
Vary mask diameter
a
Off parasol cell (surround) unadapted spikes
Off parasol cell (surround) adapted spikes
Spikes s⁻¹
Time (s)
Adapted
Unadapted
Contrast
b
Parasol cell sensitivity metrics (n = 12 cells)
Discriminability index (d')
JS distance
c
Off midget cell (surround) unadapted spikes
Off midget cell (surround) adapted spikes
d
Midget cell sensitivity metrics (n = 13 cells)
e
Off midget cell (mask diameter, 160 μm)
Off midget cell (mask diameter, 320 μm)
Off midget cell (mask diameter, 640 μm)
f
Midget cell sensitivity metrics (n = 6 cells)
Mask diameter (μm)

Figure 4.4: Sensitization arises in the receptive-field surround. (A) Spike responses from an Off parasol ganglion cell to a series of stimuli presented in the receptive-field surround. Annuli were presented in isolation (left) or following an adapting stimulus that was also presented in the receptive-field surround (middle). The adapting stimulus evoked a decrease in spiking at positive contrasts relative to the unadapted condition (red). (B) Discriminability index (d'; left) and Jensen-Shannon distance (right) for contrast responses relative to background noise in parasol ganglion cells (n=12). Statistically significant change in sensitivity indicated with asterisk. (C) Responses from an Off midget ganglion cell to the surround adaptation stimulus paradigm. Consistent with weak contrast sensitization, the adapting stimulus elicited a slight leftward shift in the contrast-response function relative to the control condition (right). (D) Sensitivity indices in 12 midget ganglion cells for surround test flashes. (E) Sensitization varies with the degree of surround stimulation. Spike responses from an Off midget cell to the surround adaptation stimulus for three mask diameters. For some mask diameters, surround adaptation (black) produced larger spike responses during the surround flash relative to the unadapted condition (red). This increase in responsiveness was not present for the largest mask diameter (640 μm, right). (F) Sensitivity metrics for four mask diameters in midget ganglion cells (n=6 cells). Surround adaptation produced significant larger d' values for mask diameters $\leq 320\mu$m and Jensen-Shannon distance values for diameters $\leq 480\mu$m ($p<0.05$; Wilcoxon signed rank test). Error bars indicate mean±SEM

To distinguish between these possibilities, we repeated the noise experiments in the same cells using large diameter spots that stimulated both the receptive-field center and surround (diameter, 730μm), and this stimulus elicited a distinct response pattern in midget cells. Following the transition to low contrast, gain rapidly increased after which it decreased gradually to the steady-state level (Figure 4.5F). This increase in gain following the transition to low contrast was evidence that contrast sensitization depended on the spatial properties of the adapting stimulus and could be elicited with temporally white stimuli [90].

These results demonstrated that the midget cell receptive field contained two competing mechanisms contributing to short-term plasticity on different spatial scales—a center mechanism that weakly adapted to fluctuations in contrast and a surround mechanism that produced sensitization (i.e., prevented adaptation). We further tested how interactions between these narrow- and wide-field mechanisms contribute to visual coding in midget cells below. First, however, we tested whether midget cell responses saturated at high contrast similar to sensitizing cells in other species [90].

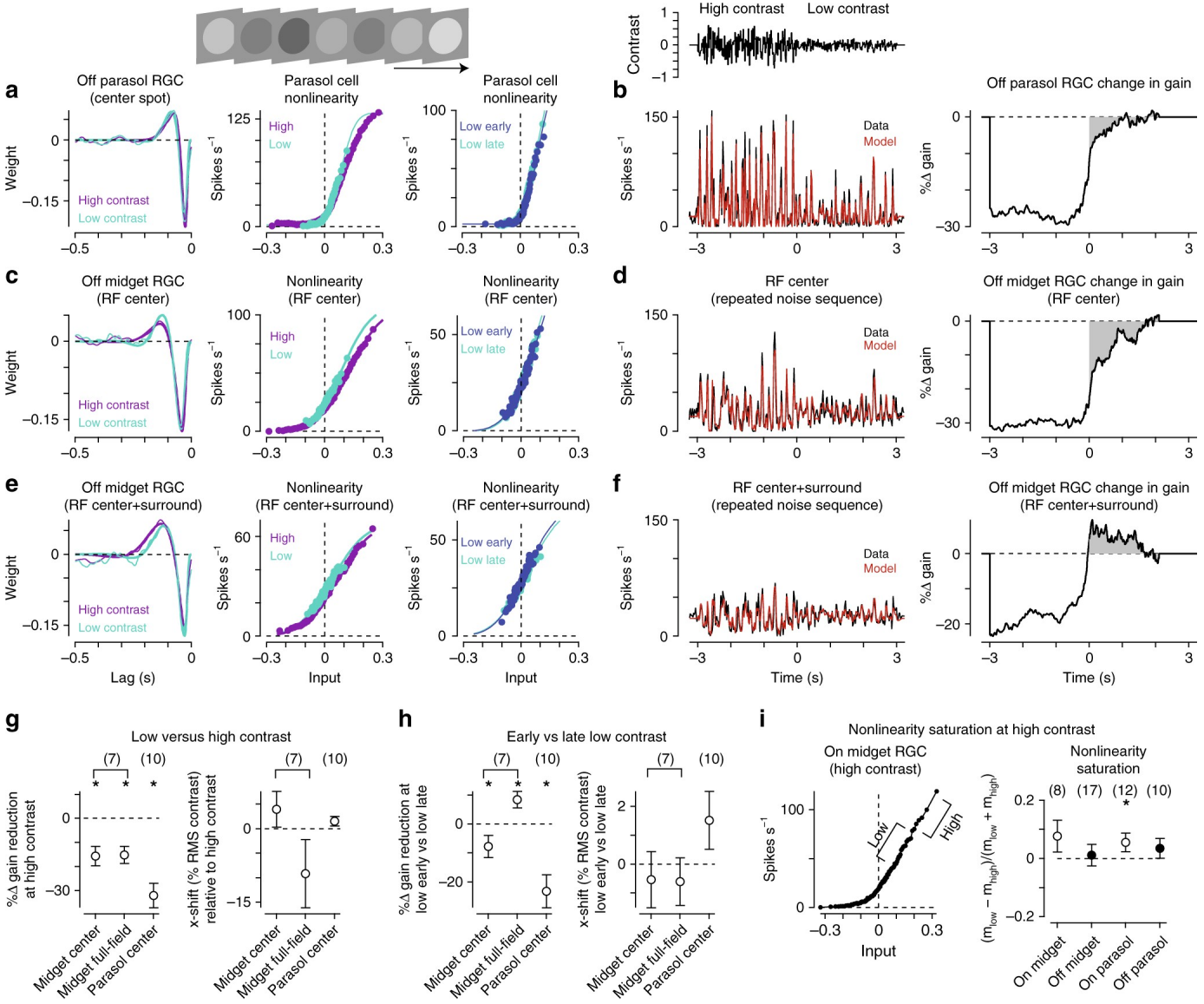
a
Off parasol RGC
(center spot)
Parasol cell
nonlinearity
Parasol cell
nonlinearity
Weight
High contrast
Low contrast
Spikes s⁻¹
High
Low
Low early
Low late
b
High contrast
Low contrast
Contrast
Off parasol RGC change in gain
Data
Model
%Δ gain
c
Off midget RGC
(RF center)
Nonlinearity
(RF center)
Nonlinearity
(RF center)
d
RF center
(repeated noise sequence)
Off midget RGC change in gain
(RF center)
e
Off midget RGC
(RF center+surround)
Nonlinearity
(RF center+surround)
Nonlinearity
(RF center+surround)
Lag (s)
Input
Input
f
RF center+surround
(repeated noise sequence)
Off midget RGC change in gain
(RF center+surround)
Time (s)
Time (s)
g
Low versus high contrast
%Δ gain reduction
at high contrast
x-shift (% RMS contrast)
relative to high contrast
Midget center
Midget full-field
Parasol center
h
Early vs late low contrast
%Δ gain reduction at
low early vs low late
x-shift (% RMS contrast)
low early vs low late
i
Nonlinearity saturation at high contrast
On midget RGC
(high contrast)
Low
High
Nonlinearity
saturation
On midget
Off midget
On parasol
Off parasol

Figure 4.5: Changes in stimulus variance evoke changes in the input–output properties of midget cells.(A) Temporal filters (left) and input–output nonlinearities (middle) in an Off parasol cell for the high and low-contrast periods. Separate nonlinearities were also calculated for the low-contrast region directly following the transition from high-to-low contrast (low early) and for the sustained low-contrast region (low late; right). (B) Average spike rate (black) and linear–nonlinear model prediction (red) for the repeated contrast trajectory (left). Data and model showed high correspondence (high contrast r^2, 0.87±0.02; low contrast r^2, 0.73±0.04; n=10 cells). Right, average gain as a function of time. Values are shown relative to the sustained low-contrast period. Shaded regions indicate the period of low contrast. (C) Same as (A) for an Off midget ganglion cell to a small spot (diameter, 80μm) presented over the receptive-field center. (D) Left: Spike rate (black) and model prediction (red) for repeated contrast trajectory (high contrast r^2, 0.91±0.02; low contrast r^2, 0.71±0.07; n=7 cells). The cell's gain was reduced following the shift to low contrast and recovered quickly to the level of sustained gain. e Linear–nonlinear model for the cell in (C) to a large spot (diameter, 730μm). (F) Responses of the cell in (B) for the large diameter spot (left). Following the transition to low contrast, gain quickly increased, exceeding the sustained level for $\sim$2s (right). (G) Left: Reduction in gain at high contrast relative to the low-contrast condition. Gain was significantly reduced at high contrast for both midget and parasol cells (n=7 midget cells; n=10 parasol cells; $p<0.05$). Right: Horizontal shift along the x-axis for the low contrast nonlinearity relative to high contrast. Wide-field stimulation in midget cells evoked a shift of $\sim$10 RMS contrast for the low-contrast condition indicating that lower contrasts were required to evoke the same spike rate as the high contrast condition. (H) Change in gain (left) and horizontal shift (right) for the early versus late low-contrast periods. (I) Nonlinearity saturation was measured for high contrast Gaussian noise (RMS contrast, 0.3) in midget and parasol ganglion cells. Saturation was quantified by comparing the slopes for the high and low-variance regions of the nonlinearity (left). The slope differences were near zero, indicating a lack of strong saturation in both midget and parasol ganglion cells (right); only On parasol cells showed saturation values that were significantly greater than zero ($p=4.6\times10^{-2}$; all other $p>0.1$). Error bars indicate mean±SEM. Statistical significance for paired values determined using Wilcoxon signed rank test and unpaired values with the Wilcoxon signed rank test

In salamander retina, sensitizing and adapting ganglion cells showed distinct sensitivity ranges. During high-contrast stimulation adapting cells reduced their gain, allowing them to avoid saturation and effectively encode contrast. However, their gain remained low for a time upon the shift to low contrast while the cells re-estimated the stimulus variance [79, 77, 75]. Sensitizing cells showed the opposite pattern—their gain remained high during transitions to low contrast, allowing them to effectively encode contrast during these shifts from high-to-low variance conditions. The downside of this behavior is that the gain of sensitizing cells was high during periods of high contrast, which caused their responses to saturate. Based on these observations, it was proposed that adapting and sensitizing cells function in a concerted manner with adapting and sensitizing

cells encoding in high and low-contrast regimes, respectively10. Thus, if the same pattern holds in primate retina, one would expect midget ganglion cells to saturate during high-contrast stimulation and one would likewise expect to find an adapting cell type that encodes common visual information to midget cells (i.e., red-green color, achromatic).

$$saturation\ index\ = \frac{M_{low} - M_{high}}{M_{low} + M_{high}} \tag{4.1}$$

Values near zero would occur for nonlinearities with little or no saturation while values near one occur for strongly sigmoidal nonlinearities that saturated at high contrast. Consistent with a lack of saturation, index values were near zero for both On and Off midget cells (Figure 4.5G). Thus, unlike sensitizing cells in other species, midget cells did not show saturation at high contrast10, indicating that an adapting counterpart was not required to offset saturation in midget cells. This further suggested that sensitization performs a distinct role in midget cells relative to that posited for other species.

4.3.4 Sensitization enhances chromatic processing in midget cells

Midget ganglion cells in the central retina exhibit strong chromatic opponency which is formed from differential input from long-wavelength cones (L cones) and middle-wavelength cones (M cones) to the receptive-field center and surround [20, 19, 219]. To determine whether sensitization affected chromatic processing, we measured contrast responses in midget cells with purely chromatic (isoluminant) test flashes following the adapting stimulus.

Isoluminant (equiluminant) stimuli are commonly employed to study color mechanisms in isolation. We measured contrast-responses to purely chromatic (L-M; isoluminant) flashes (duration, 0.1s) in the presence or absence of an achromatic adapting stimulus, as above. This stimulus was specifically designed to modulate chromatic mechanisms that differentiate L- and M-cone inputs (L-M; isoluminant) while silencing achromatic mechanisms that sum inputs from the L- and M-

cone pathways (L+M; isochromatic).

As with the achromatic stimuli, the adapting stimulus significantly improved sensitivity for low-contrast test flashes (Figure 4.6C, indicating that contrast sensitization enhanced both achromatic and chromatic processing in midget cells. While chromatic processing was affected by sensitization, the observation that an achromatic adapting stimulus was sufficient to evoke sensitization demonstrated that chromatic stimuli were not necessary to elicit the phenomenon. These data did not, however, rule out contributions from purely chromatic mechanisms to contrast sensitization.

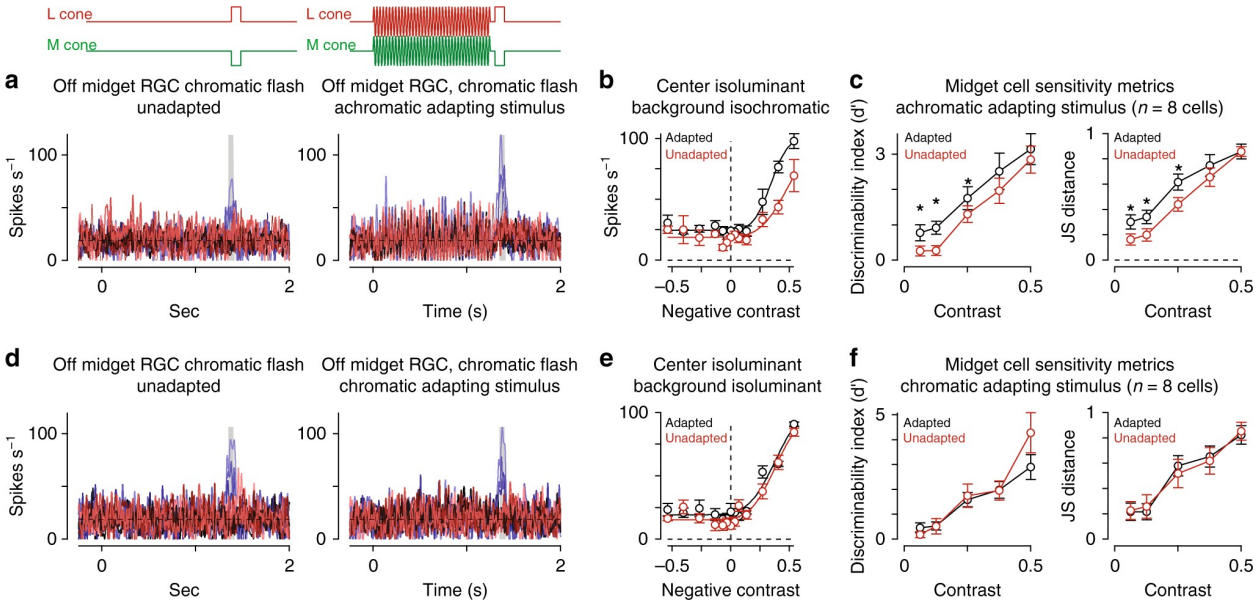

Figure 4.6: Sensitization arises from an achromatic mechanism. (A) Spike responses from an Off midget ganglion cell to a chromatic (isoluminant) contrast series. Spots were either presented alone (left) or 50ms following the offset of an achromatic adapting stimulus (right). Shaded regions indicate sampling windows. (B) Average spike rate across the shaded regions indicated in (A). Achromatic adaptation evoked a leftward shift in the contrast-response curve (black) relative to the unadapted control condition (red) for the chromatic test flash. (C) Sensitivity metrics for the achromatic adapting stimulus followed by a chromatic contrast series in eight midget ganglion cells. The adapting stimulus improved chromatic sensitivity at low contrast (contrast, $\leq$25; $p<0.05$; Wilcoxon signed rank test). (D) Spike responses for the cell in (A) to a chromatic adapting stimulus. (E) Average spike rate during the chromatic test flashes. The chromatic adapting stimulus did not evoke a large change in the contrast-response curve relative to control. (F) Sensitivity metrics for the chromatic adaptation experiment. Changes in sensitivity were not significantly different relative to the unadapted control at any contrast (n=8 cells; $p>0.1$; Wilcoxon signed rank test). Circles and bars indicate mean±SEM

To determine whether such a chromatic mechanism contributed to the observed contrast sensitization, we repeated the chromatic sensitivity tests following a chromatic adapting stimulus. However, the chromatic adapting stimulus did not produce a significant increase in chromatic contrast sensitivity at any contrast (Figure 4.6F). We interpret this result as evidence that contrast sensitization arose from an achromatic mechanism in the midget cell receptive field. Moreover, given the role of horizontal cells in forming the L-versus-M opponent receptive-field surround, these data excluded horizontal cells as the source of sensitization in the midget pathway [20].

4.3.5 Sensitization is present in excitatory synaptic input from midget bipolar cells

The experiments above found contrast sensitization in the spike output of midget ganglion cells. Our next goal was to understand the circuit mechanisms mediating sensitization. To accomplish this goal, we measured the direct excitatory and inhibitory synaptic inputs to midget ganglion cells with whole-cell, voltage-clamp recordings (see Methods). Excitatory currents were isolated by holding a cell's membrane voltage at the reversal potential for inhibition (-70mV), and likewise, inhibitory currents were recorded at the excitatory reversal potential (0mV). An increase in excitatory input to a cell was indicated by a more negative (inward) current relative to the leak current. Indeed, the adapting stimulus evoked larger inward excitatory currents relative to the unadapted control at all contrasts tested (Fiure 4.7A). Plotting excitatory charge as a function of contrast revealed a similar pattern to that observed in the spike recordings—the adapting stimulus evoked a leftward shift in the contrast-response curve relative to the unadapted control (Figure 4.7B). These results indicated that contrast sensitization was present in the excitatory synaptic input from midget bipolar cells to midget ganglion cells.

We also tested for the presence of sensitization in the inhibitory synaptic inputs to midget cells. Unlike the pattern observed in spiking and excitatory currents, the adapting stimulus did not elicit

significant shifts in the inhibitory contrast-response functions relative to control (Figure 4.7C). These data showed that contrast sensitization arose at or prior to the level of glutamate release from midget bipolar cells. This finding was consistent with the circuit model for contrast sensitization in bipolar cells in the retinas of fish, salamander, mice, and rabbits10–12. This model posited a mechanism in which a strongly adapting amacrine cell drove sensitization by a mechanism of presynaptic inhibition at the bipolar cell terminal11. During the adapting stimulus, the amacrine cell adapted such that, following stimulus offset, the cell decreased release of inhibitory neurotransmitter to the bipolar cell synaptic terminal relative to the tonic level. This presynaptic disinhibition, in turn, depolarized the bipolar cell synaptic terminal, allowing the cell to utilize its

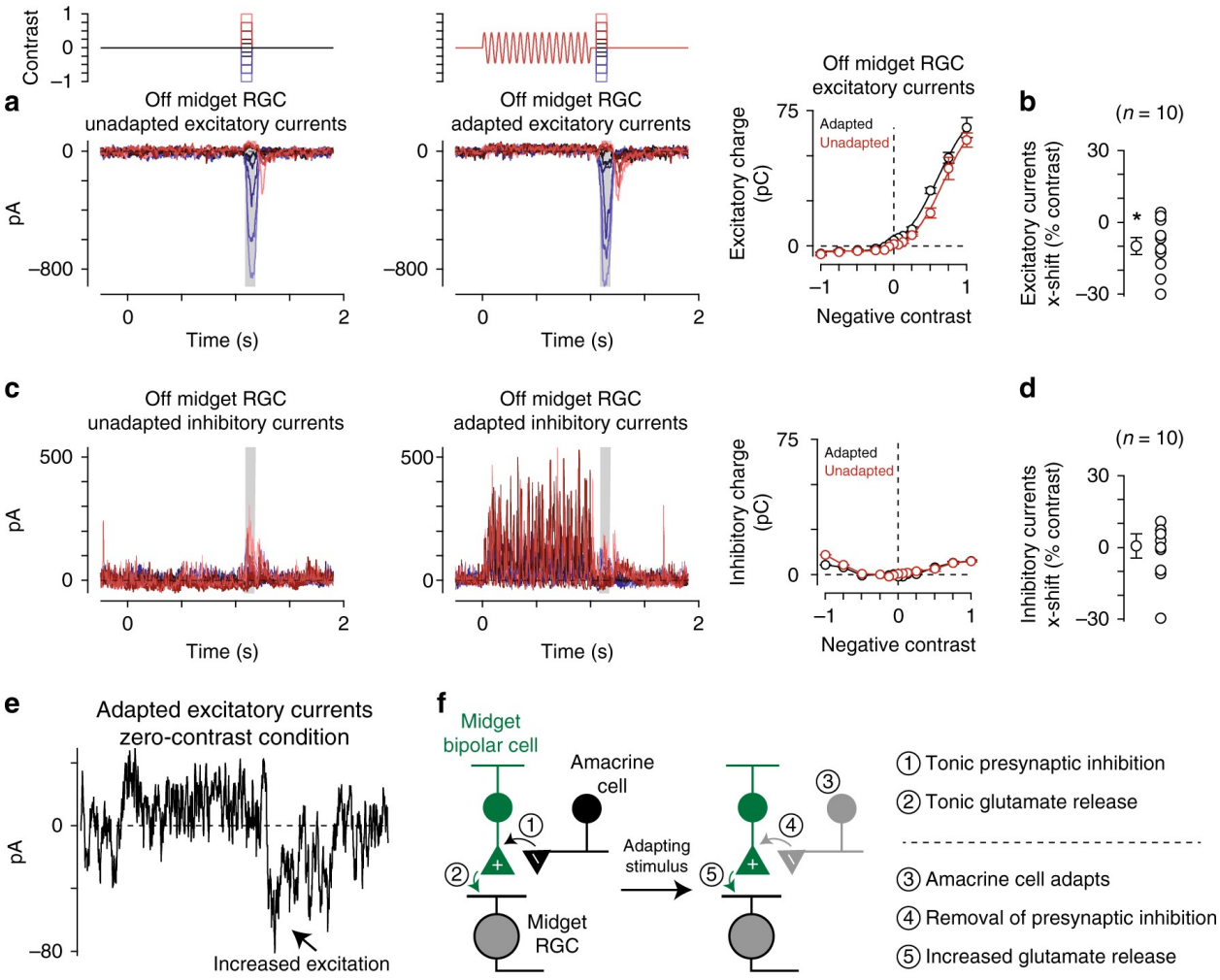

Figure 4.7: Sensitization was present in excitatory synaptic input from midget bipolar cells. (A) Excitatory synaptic currents from a central Off midget ganglion cell to a series of spots (diameter, 40–80μm) centered over the receptive field. Spots were either presented alone (left) or 50ms following the offset of an adapting stimulus (right; diameter, 730μm). Shaded regions indicate sampling windows. Right: Average excitatory synaptic charge across the shaded regions. The wide-field adaptation evoked a leftward shift in the contrast-response curve (black) relative to the unadapted control condition (red). (B) Population data from midget cells showing the x-axis shift for adapted relative to unadapted conditions in excitatory synaptic currents. The adapting stimulus evoked a significant leftward shift relative to the unadapted condition, indicating that contrast sensitization was present in the excitatory input from midget bipolar cells to midget ganglion cells (n=10 cells; p=1.4×10^{-2}). Mean values are shown in gray. Open circles are individual cells. c Inhibitory synaptic currents from the Off midget cell in (A). Inhibitory currents did not show a noticeable shift along the x-axis (right) and were small relative to excitatory currents recorded in the same cell (compare (A) with (C)). (D) Horizontal shift values for inhibitory synaptic inputs as in (B). Inhibitory inputs did not show consistent leftward shifts, indicating that postsynaptic inhibition was unlikely to contribute to the contrast sensitization observed in the spike output of midget ganglion cells (n=10 cells; p=0.15). Error bars indicate mean±SEM. Statistical significance determined with Wilcoxon signed rank test. (E) Excitatory current recordings from the Off midget cell in (A) under the condition in which the stimulus intensity returned to the mean luminance after the offset of the adapting stimulus and an additional test flash was not presented (zero-contrast condition). A sustained increase in excitatory current was observed at the offset of that stimulus. (F) Proposed model for contrast sensitization in midget bipolar cells. Statistical significance was determined using the Wilcoxon signed rank test

full dynamic range in signaling via glutamate release to postsynaptic ganglion cells (Figure 4.8).

Cleanly measuring the effects of presynaptic inhibition on circuit function has proven exceedingly difficult as use of inhibitory receptor antagonists typically cause many off-target effects that make data interpretation highly tenuous24. Indeed, adding inhibitory antagonists in primate retina evoked significant increases in tonic glutamate release from bipolar cells and changed the contrast polarity of On parasol cells [25]. Nonetheless, our spike and whole-cell recordings strongly supported the proposed model in which contrast sensitization arose from disinhibition at the presynaptic bipolar cell terminal11. First, the lack of sensitization to a purely chromatic (isoluminant) adapting stimulus indicated that sensitization did not arise in the outer retina at the level of horizontal cell feedback (Figure 4.6). Further, horizontal cells are unlikely to contribute significantly to contrast sensitization as work in other species indicates that these cells do not exhibit contrast

adaptation [79, 220, 221].

Second, the effect of presynaptic disinhibition was seen in our excitatory current recordings (Figure 4.7E). In one of our stimulus conditions the test flash contrast was zero such that the stimulus intensity returned to the average background intensity at the offset of the adapting stimulus. Although this stimulus lacked a change in contrast following the adapting stimulus, we observed a significant increase in excitatory synaptic input (adapted condition, +1.4 ± 0.6 pC; $p_{adapted}$= 3.7×10^{-2}; unadapted condition, +0.06 ± 0.11 pC; $p_{unadapted}$=0.47; n=10 cells; Wilcoxon signed rank test; Figure 4.7E).This response pattern was consistent with a decrease in presynaptic inhibition following the offset of the adapting stimulus, resulting in an increase in glutamate release from midget bipolar cells. Thus, our recordings in the midget pathway of primate retina were consistent with the circuit motif proposed in other vertebrate species (Figure 4.6 and 4.7F)11.

4.3.6 Sensitizing circuits more accurately reconstruct natural stimuli than adapting circuits

We next sought to understand how these differing strategies of adaptation and sensitization impacted encoding during naturalistic vision. This was done by testing the ability of adapting and sensitizing models to accurately encode natural scenes. We specifically wanted to determine how accurately downstream visual circuits could reconstruct naturalistic input stimuli based on the outputs of populations of model On and Off midget ganglion cells. The naturalistic stimuli used in the model were taken from the DOVES database—a dataset of eye movements in humans recorded while observing natural images [222]. Reconstruction accuracy was determined by calculating the correlation between the stimulus and response of each model (see Methods). Periods of fixation between ballistic eye movements are critically important to visual coding in primates; thus, model performance was separately calculated for the complete movie or for periods of fixation only.

We considered two different decoding models for estimating the stimulus contrast based on the

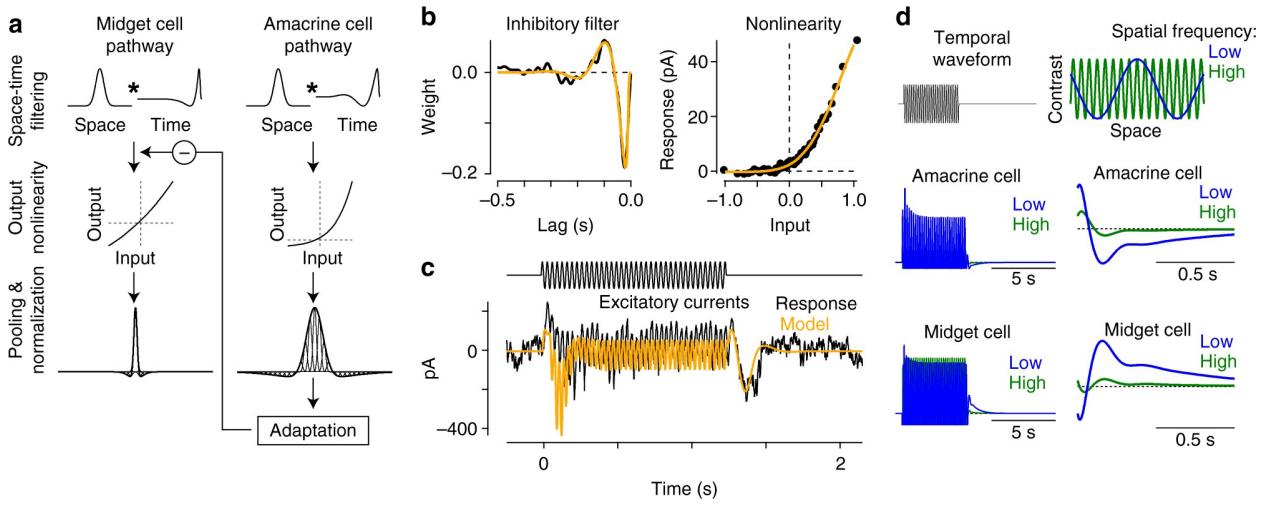

Figure 4.8: Sensitization model reproduces experimental results. (A) Sensitization model structure. Visual inputs were convolved with a spatiotemporal linear filter comprised of a Gaussian in space and a biphasic filter in time. Signals in the amacrine cell pathway were then passed through an output nonlinearity before passing to the adaptation stage of the model. The output of the amacrine cell model provided inhibitory input to the midget bipolar cell pathway upstream of the bipolar cell output nonlinearity. (B) Inhibitory temporal filter (left) and input–output nonlinearity (right) determined from noise recordings. These filters were then used as components of the computational model (A). (C) Excitatory current recording from an Off midget ganglion cell to the wide-field adapting stimulus (see Figure 3.7). Model prediction (orange) was generated from excitatory synaptic current recordings to the noise stimulus in the same cell. (D) Model output for drifting grating stimuli at high and low spatial frequencies

outputs of On and Off midget ganglion cells (see Methods). Regardless of the decoding scheme used, the sensitizing model showed higher accuracy for reconstructing the entire stimulus trajectory than either the adapting model or the LN model (Figure 4.9C). The sensitizing model also outperformed the other models when the analysis was restricted to periods of fixation (Figure 4.9D). We interpret the outperformance of the sensitization model over the adaptation and linear–nonlinear models as support for the hypothesis that neural sensitization improves faithful encoding of visual inputs to midget ganglion cells.

We next sought insight into the stimulus conditions in which neural adaptation would improve encoding. Previous work supported a role for adaptation in determining when salient stimulus features changed [215, 75, 82]. Thus, we fit our models to the change in contrast as a function

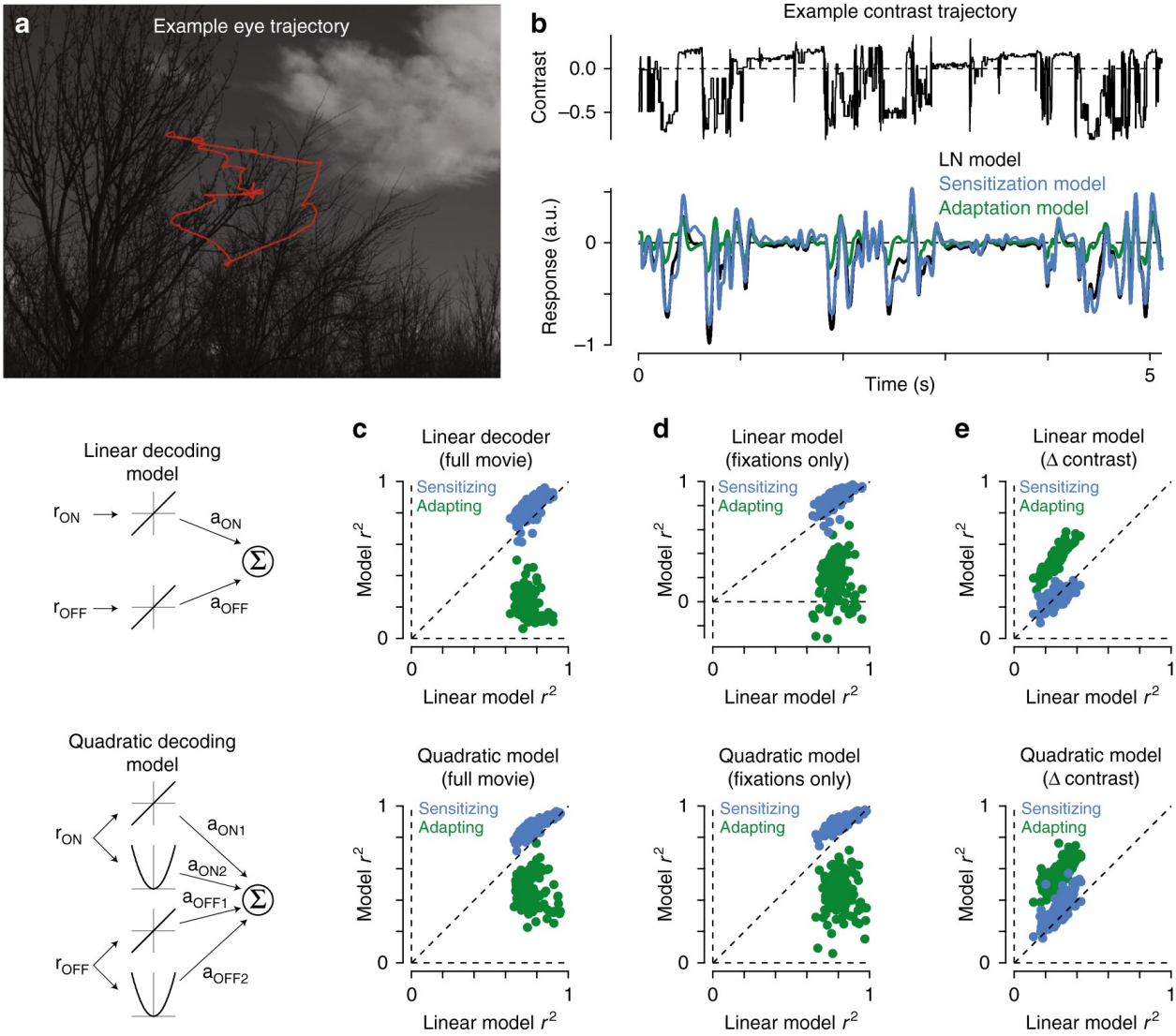

Figure 4.9: Sensitization increases the fidelity of encoding natural movies.(A) Example image from the DOVES database. The observer's eye trajectory is shown in red. (B) Top: temporal contrast sequence from the eye movement data in (A). Bottom: responses of the adaptation and sensitization models to the example contrast sequence. (C) Performance of the sensitization and adaptation (y-axis) models at reconstructing 161 natural movies in the database. Model performance is shown relative to the linear–nonlinear model performance for each movie (x-axis). Performance was measured as the Pearson correlation between the stimulus and model predictions after adjusting for temporal lag. Performance for each movie is indicated by a dot. The sensitization model outperformed the linear–nonlinear and adaptation models ($p<6.2\times10^{-}26$). (D) Model performances as in (C), but restricted to periods of fixation. The sensitization model again outperformed the linear–nonlinear and adaptation models ($p<4.4\times10^{-}25$). (E) Model performance for the change in contrast as a function of time. The adaptation model outperformed both the linear–nonlinear and sensitizing models at decoding the change in the contrast trajectory ($p<1.0\times10^{-}23$. Statistical tests were paired and were determined using Wilcoxon signed rank test

of time (see Methods). Indeed, the adaptation model outperformed both the sensitizing and linear–nonlinear models at reproducing the change in contrast (Figure 4.9E). In fact, the adaptation model performed significantly better at encoding the change in contrast than at encoding the contrast itself—model correlation improved by 149±10% for the linear decoding paradigm and 27±2% for the quadratic decoding paradigm ($p<3.9\times10–21$; n=161 movies; Wilcoxon signed rank test). Possible benefits of representing the temporal derivative of contrast in natural vision are considered in the Discussion.

4.3.7 Background motion evokes contrast sensitization in midget cells

The finding that the sensitization model outperformed the other model paradigms during periods of fixation suggested that sensitization could play a particularly important role in vision during periods of fixation following the offset of global motion. Mechanisms that would maintain sensitivity during eye movements would be particularly critical given the high frequency of these movements in primates. We, thus, sought to determine whether background motion could evoke contrast sensitization with direct recordings from midget ganglion cells. We measured contrast responses in parasol and midget cells following the offset of a full-field moving texture (speed, 5–11 degrees s^{-1}; duration, 1s). The goal was to simulate, as closely as possible, the brief periods of fixation following eye movements and to test sensitivity during these fixation periods. We interleaved these recordings with measurements when the texture was stationary throughout the trial.

As with the other adapting stimuli, background motion elicited a reduction in sensitivity in parasol cells (Figure 4.10. In midget cells, however, background motion elicited increased sensitivity at low contrast (Figure4.10F). These results indicated that eye motion should produce profoundly different effects on the two numerically dominant output pathways of the primate retina. As with the computational model (Figure 4.9), adaptation in parasol cells would render them less sensitive following eye motion. Due to sensitization, however, the midget pathway would be poised to report information about a fixated object following eye movements.

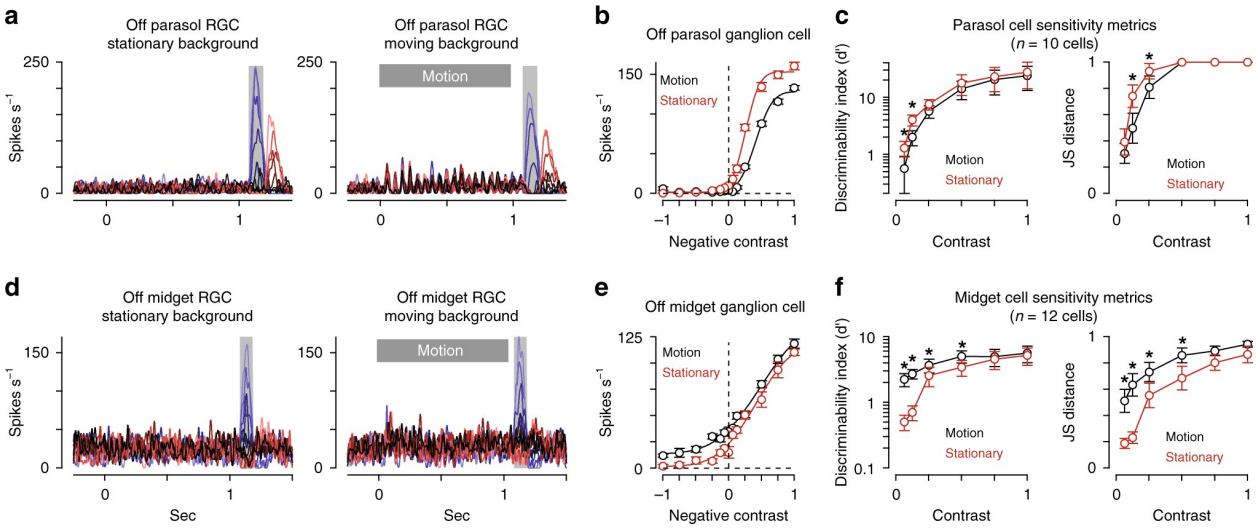

Figure 4.10: Background motion evokes adaptation in parasol cells and sensitization in midget cells. (A) Averages spike rate as a function of time for an Off parasol ganglion cell a stationary texture followed by a series of test flashes centered over the cell's receptive field (left) or following the offset of texture motion (right; speed, 11 degrees s^{-1}). (B) Contrast-response functions for the cell in (A) for the measurements with a stationary texture (red) or a moving texture (black). (C) Sensitivity metrics for this experiment across 10 parasol cells. (D) Spike responses from an Off midget ganglion cell to the same experimental protocol. e Average spike rate across the shaded regions indicated in (D). The wide-field adaptation evoked a leftward shift in the contrast-response curve (black) relative to the unadapted control condition (red). (F) Sensitivity values for the motion experiment across 12 midget cells. Motion produced a significant increase in sensitivity at low contrast relative to the stationary condition (contrast, $\leq$50%; p<0.05; Wilcoxon signed rank test). Circles and bars indicate mean±SEM

4.4 Discussion

Our results support a novel role for neural sensitization in primates relative to the function proposed in other species. Sensitizing cells are commonly thought to counteract the loss of responsiveness experienced by adapting cells during transitions from high to low variance environments10. This hypothesis requires that sensitizing cells have an adapting counterpart that encodes similar information about the environment. Midget (parvocellular-projecting) ganglion cells are well known for their roles in both chromatic and achromatic vision [20, 19, 223, 224]. Functional parallelism in the midget pathway is achieved by splitting signals between different classes of cone photoreceptor (L versus M) or bipolar cell (On versus Off) inputs to the midget cell receptive field. Further, we

found that both On- and Off-type midget cells exhibited sensitization (Figures 4.14.24.3 and [90]), and the primate retina lacks an adapting functional counterpart to midget cells with similar chromatic opponency or spatial acuity [179]; thus, sensitization does not counterbalance adaptation in another functionally parallel pathway. This conclusion is further bolstered by the observation that the spike output of midget cells did not saturate during high variance stimulation (Figure 4.10), indicating the sensitization performs a distinct function in primate retina relative to other species10.

Instead, our findings support a role for sensitization in maintaining the responsiveness of the midget pathway during dynamic visual processes, such as head or eye movements, that cause rapid fluctuations in light intensity on the retina. We base this conclusion on several key observations. First, sensitization was strongest following wide-field stimulation (Figure 4.1 and 4.2) or background motion (Figure 4.10). Second, sensitization persisted for >0.2s (Figure 4.3), a period that roughly corresponds to the durations of fixations following eye movements in primates (reviewed in [225]). Finally, sensitization greatly improved the fidelity of encoding natural movies, particularly during periods of fixation following ballistic eye motion (Figure 4.9). Thus, sensitization appears to play a unique and crucial role in neural coding in primates.

A parallel study also found evidence supporting the link between the sensitization mechanisms that we observed in midget ganglion cells and visual perception in humans33. Subjects showed a significant enhancement in contrast sensitivity following the offset of wide-field motion; and this increase in sensitivity was manifest as a leftward horizontal shift in the perceptual input–output relationship, just as we observed in midget cells (compare Figure 4.2 in our study with Figure 5 of ref. [183]). Together, these findings provide a rare example of a behavior that can be directly tied to a specific neural circuit motif.

4.4.1 Distinct functions of adaptation and sensitization in primate retina

Our findings also speak to the roles of neural adaptation in the parasol and broad thorny ganglion cell pathways. Previous work proposed that adapting cells could produce a nearly optimal faithful

encoding of sensory inputs [75]. Our computational model, however, indicates that sensitizing circuits outperform adapting circuits in faithfully encoding natural movies (Figure 4.9). The improved reconstruction accuracy of the sensitizing model was consistent with a recent theoretical report indicating that sensitizing cells are better for encoding faithful representations of sensory input than adapting cells [215]. According to this paradigm, sensitizing cells such as midget ganglion cells would be useful for directly encoding information about the properties of the input (e.g., contrast, color). Adapting cells, on the other hand, are optimized for performing inference tasks [215, 82].

Adapting cells dynamically adjust their input–output properties to align with the recent stimulus distribution [79, 77]. These adjustments make the cells exquisitely sensitive to changes in stimulus statistics, allowing them to infer when salient properties of the environment change. For example, quickly detecting object motion is an ethologically relevant and phylogenetically ancient neural computation [226, 227]; by decreasing their responsiveness during periods in which the background is either stationary or coherently moving, adapting neural circuits would be poised to report when an object moves relative to the background [66, 30]. Indeed, our adapting model outperformed other models at representing the change in contrast as a function of time (Figure 4.9). Algorithms that compute changes in image contrast as a function of time are commonly used in computer-based vision systems that calculate visual motion features such as optical flow. Whether the output of adapting retinal cells, such as parasol cells or broad thorny cells, might also be used for similar computations by downstream visual circuits is not currently known. However, both parasol and broad thorny ganglion cells have been implicated in motion processing [25, 30, 26, 27] and they project to retinorecipient brain regions in the lateral geniculate body, superior colliculus, and inferior pulvinar that contribute significantly to motion vision [149, 203, 228]).

4.4.2 Relationship to psychophysical measurements in humans

It has long been recognized that eye movements play important computational roles in visual processing (reviewed in refs. [229, 119]). Periods in which an image is stabilized on the retina cause that image to fade from perception45 and small fixational eye movements appear to counteract this fading [123, 230]. These eye movements can, however, produce large temporal fluctuations in contrast, particularly when viewing high-contrast objects. This would, in turn, produce fading phenomena in cells that strongly adapt, such as parasol ganglion cells—a prediction that was confirmed with our background motion experiments and computational model (Figure 4.9 and4.10).

Neural mechanisms such as sensitization may serve to counteract adaptation by maintaining the sensitivity of certain visual pathways during eye movements. Indeed, our computational model and direct measurements indicated that contrast sensitization in the midget ganglion cell pathway was engaged well by background motion such as that observed during eye movements (Figure 4.9 and 4.10). Thus, contrast sensitization might act to maintain sensitivity of image-forming visual pathways following eye movements that are commonplace in primate vision. Indeed, psychophysical studies in humans indicated that contrast sensitivity increases following both ballistic (saccade) and fixational eye movements [123, 230–232]. This increase in sensitivity was observed to chromatic stimuli and high-spatial-frequency achromatic stimuli, mirroring our results in midget ganglion cells. It was hypothesized that these increases in sensitivity arose in the thalamus47; however, our results support an origin much earlier in the visual pathway—in the interplay between wide-field amacrine cells and midget bipolar cells in the inner retina (Figure 4.7).

4.4.3 Future directions

Given its recent discovery, relatively few studies have investigated the role of sensitization in neural processing [90, 92, 91, 215, 217]. Here, we used a complementary set of visual stimuli and a computational model in our attempts to understand this phenomenon, but many questions remain. For

example, the roles that sensitization plays during natural vision are not well understood, and we developed a computational model to gain insight into this question. The parameters for this model were determined from direct recordings of synaptic inputs to midget ganglion cells using uncorrelated noise. Recent work, however, has clearly demonstrated that the recruitment of different neural mechanisms can vary dramatically between artificial and naturalistic stimuli [17, 18, 101]. Thus, studies of adaptation and sensitization in the context of more naturalistic stimuli are needed to elucidate the roles of short-term plasticity mechanisms in visual processing.

4.5 Methods

4.5.1 Tissue preparation and electrophysiology

Experiments were performed in an in vitro, pigment-epithelium attached preparation of the macaque monkey retina [63]. Eyes were dissected from terminally anesthetized macaque monkeys of either sex (Macaca fascicularis, mulatta, and nemestrina) obtained through the Tissue Distribution Program of the National Primate Research Center at the University of Washington. All procedures were approved by the University of Washington Institutional Animal Care and Use Committee.

The retina was continuously superfused with warmed (32–35°C) Ames' medium (Sigma) at $\sim$6–8 mL min^{-1}. Recordings were performed from macular, mid-peripheral, or peripheral retina (2–8 mm, 10–30 foveal eccentricity), but special emphasis was placed on recording from more centrally located cells. Physiological data were acquired at 10kHz using a Multiclamp 700B amplifier (Molecular Devices), Bessel filtered at 3kHz (900 CT, Frequency Devices), digitized using an ITC-18 analog-digital board (HEKA Instruments), and acquired using the Symphony acquisition software package developed in Fred Rieke's laboratory (http://symphony-das.github.io).

Recordings were performed using borosilicate glass pipettes containing Ames medium for ex-

tracellular spike recording or, for whole-cell recording, a cesium-based internal solution containing (in mM): 105 CsCH3SO3, 10 TEA-Cl, 20 HEPES, 10 EGTA, 2 QX-314, 5 Mg-ATP, and 0.5 Tris-GTP, pH 7.3 with CsOH, ∼280 mOsm. Series resistance (∼3–9 MΩ) was compensated online by 50%. The membrane potential was corrected offline for the approximately 11mV liquid junction potential between the intracellular solution and the extracellular medium. Excitatory and inhibitory synaptic currents were isolated by holding midget ganglion cells at the reversal potentials for inhibition/chloride (∼-70 mV) and excitation (0 mV), respectively.

4.5.2 Visual stimuli and data analysis

Visual stimuli were generated using the Stage software package developed in the Rieke lab (ttp://stage-vss.github.io) and displayed on a digital light projector (Lightcrafter 4500; Texas Instruments) modified with custom LEDs with peak wavelengths of 405, 505 (or 475), and 640 nm. Stimuli were focused on the photoreceptor outer segments through a ×10 microscope objective. Mean light levels were in the low to medium photopic regimes ($\sim 3 \times 103$–3.4×10^4 photoisomerizations [R*] cone^{-1} s^{-1}). Contrast values for contrast-response flashes are given in Weber contrast and for periodic stimuli in Michaelson contrast. All responses were analyzed in MATLAB (R2018b, Mathworks).

For extracellular recordings, currents were wavelet filtered to remove slow drift and amplify spikes relative to the noise54 and spikes were detected using either a custom k-means clustering algorithm or by choosing a manual threshold. Whole-cell recordings were leak subtracted and responses were measured relative to the median membrane currents immediately preceding stimulus onset (0.25–0.5 s window).

4.5.3 Sensitivity calculations

We evaluated a cell's ability to accurately detect a change in contrast using two independent measures—the discriminability index and the Jensen-Shannon distance. The discriminability index (d) is a relatively simple metric for determining the amount of overlap between signal and noise distributions:

$$d' = \frac{\mu_S - \mu_N}{\sqrt{\frac{1}{2}(\sigma_S^2 + \sigma_N^2)}} \tag{4.2}$$

where μ_S and μ_N are the mean of the signal and noise distributions and σ_S^2 and σ_N^2 are the variances of those distributions, respectively.

The Jensen-Shannon distance was calculated from the Kullback-Leibler divergence (D_{KL}) between the spike count probability distributions for the signal (P) and noise (Q).

$$JS(P,Q) = \sqrt{\frac{1}{2}\left[D_{KL}\left(P\middle|\frac{P+Q}{2}\right) + D_{KL}\left(Q\middle|\frac{P+Q}{2}\right)\right]} \tag{4.3}$$

The Kullback-Leibler divergence between the spike count distributions was calculated as:

$$D_{KL}(P||Q) = \sum_n p_n log_2\left(\frac{p_n}{q_n}\right) \tag{4.4}$$

where p_n is the probability of observing n spikes in the sample window and q_n is the probability of observing n spikes in the sample window during presentation of a uniform mean background.

4.5.4 Temporal noise analysis

To directly measure how changes in stimulus variance affected temporal filtering and sensitivity, we presented a Gaussian flicker stimulus. Equivalent periods of high and low variance were

presented on each trial, and separate temporal filters were calculated for these periods by cross-correlating the contrast trajectory (S) with the cell's spike output (R)4.

$$F(t) = \int R(\tau)S(t+\tau)d\tau \tag{4.5}$$

The resulting filters were fit with a function commonly used to model time-domain filtering of retinal cells55,56:

$$(t) = A\frac{(t/\tau_{rise})^n}{1+(t/\tau_{rise})^n}e^{-(t/\tau_{decay})}\cos\left(\frac{2\pi t}{\tau_{period}}+\varphi\right) \tag{4.6}$$

where A is a scaling factor, τ_{rise} is the rising-phase time constant, τ_{decay} is the damping time constant, τ_{period} is the oscillator period, and φ is the phase (in degrees).

The input–output nonlinearity was calculated by convolving the temporal filter and stimulus to generate the linear prediction. The prediction (x-axis) and response (y-axis) were modeled as a cumulative Gaussian distribution57.

$$N(x) = \varepsilon + \frac{\alpha}{2\pi}\int_{-\infty}^{x} e\frac{-(\beta t+\gamma)}{2}dt \tag{4.7}$$

where α indicates the maximal output value, ε is the vertical offset, β is the sensitivity of the output to the generator signal (input), and γ is the maintained input to the cell. Input–output nonlinearities were separately calculated for three distinct stimulus–response regions: (1) the period of high contrast stimulation, (2) the period of low-contrast stimulation immediately following the transition from high contrast (100–600ms; low early), and (3) the sustained period of low contrast (>1s following the high-to-low transition; low late).

Changes in sensitivity can result in changes in the maximal slope (i.e., gain) or horizontal shifts in this input–output nonlinearity. Thus, we simultaneously fit the high and low contrast filters such that the gain and horizontal offset were allowed to vary between the filters and the other parameters were shared [89, 233]. Fitting was performed via nonlinear least-squares curve fitting.

To evaluate model performance, we interleaved trials in which a unique contrast trajectory was presented to a cell with trials in which the contrast trajectory was not unique (noise seed=1). These non-unique trials were equally interspersed with the unique trials. Model performance was evaluated by averaging the responses from non-unique trials and calculating the Pearson correlation coefficient between the model prediction and this average response.

4.5.5 Sensitization and adaptation models

We modeled spatiotemporal integration in bipolar cells and amacrine cells as the product of a Gaussian spatial filter and a biphasic temporal filter which was then passed through an input–output nonlinearity. The output of this nonlinear stage of the amacrine cell model was then passed through an adaptation stage; adaptation in the amacrine cell provided inhibitory input to the bipolar cell model prior to the output nonlinearity (Figure 4.8A). Following the subunit output, model midget ganglion cells and amacrine cells pooled (summed) inputs from bipolar cell subunits and the weights of these inputs were normalized by the subunit location relative to the receptive-field center using a Gaussian weighting.

To estimate the excitatory and inhibitory circuit components for the computational model, we recorded excitatory and inhibitory synaptic currents from midget ganglion cells in response to a full-field Gaussian flicker stimulus. The contrast of each frame was drawn randomly from a Gaussian distribution and that value was multiplied by the average contrast. Average contrast was updated every 0.5s and drawn from a uniform distribution (0.05–0.35 RMS contrast). The linear temporal filters (F) were calculated by cross-correlating the stimulus sequence (S) and the leak-subtracted response (R) as described above.

The spatial component of the bipolar and amacrine cell receptive fields was modeled as a Gaussian function with a 2-SD width of 18 and 90μm, respectively. Each midget ganglion cell was modeled as receiving input from a single bipolar cell, as is typically the case in the central retina. Sensitization parameters were determined by fitting linear–nonlinear model predictions

relative to the excitatory currents recorded to the Gaussian flicker stimulus.

The amacrine cell providing direct inhibition to the midget ganglion cells is likely distinct from the cell providing presynaptic inhibition at the level of the midget bipolar cell (see Figure 4.7). Thus, our inhibitory synaptic recordings likely did not grant us direct access to the properties of the amacrine cell responsible for contrast sensitization. These recordings do, however, provide an estimate of the time course of signals passing through the presynaptic amacrine cell to midget bipolar cells. Signals passing through this amacrine cell proceed from cone photoreceptors to bipolar cells and then to the amacrine cell in question before providing input to the midget bipolar cell. In the same way, the amacrine cell providing direct inhibition to midget ganglion cells must pass through an extra synapse. Thus, our recordings of direct synaptic inhibition were useful in approximating the time course (i.e., temporal lag) of presynaptic inhibition at the midget bipolar terminal.

4.5.6 Evaluating model performance to naturalistic movies

We evaluated the performance of the adaptation and sensitization models in reconstructing the naturalistic movie sequences using linear and quadratic decoding paradigms. To estimate stimulus contrast, the linear decoder (f_{LINEAR}) summed the scaled outputs of the model On and Off midget ganglion cells:

$$f_{LINEAR}(t) = a_{ON} r_{ON}(t) = a_{OFF} r_{OFF}(t) + k \tag{4.8}$$

where a_{ON} and a_{OFF} are scaling constants and k is an offset constant. The quadratic model was similar in structure except that the response from each pathways was squared prior to summation:

$$f_{quadratic} = a_{on1} r_{on1} + a_{on2} r_{on2}^2 + a_{off1} r_{off1} + a_{off2} r_{off2}^2 \tag{4.9}$$

For each of the 161 movies in the database, the input stimulus was shifted to the peak of the

midget temporal filter (∼35ms) and then scaling and offset coefficients were determined using least-squares curve fitting. The Pearson correlation was then calculated between the temporal trajectories of the model and the movie.

We used the same technique to also evaluate model performance in reconstructing the change in contrast as a function of time. The change in contrast was calculated by taking the first derivative of the contrast trajectory and low-pass filtering the resulting vector with a Gaussian filter (s.d., 20 ms).

4.5.7 Quantification and statistical analysis

All statistical analyses were performed in MATLAB (R2018b, Mathworks). Reported p values in this study were either determined using the Wilcoxon signed rank test for paired data and the Wilcoxon rank sum test (i.e., Mann–Whitney U test) for unpaired data. Final figures were created in MATLAB, Igor Pro, and Adobe Illustrator.

Chapter 5

Conclusions and Future Directions

In the preceding chapters of this thesis, we investigated motion sensitivity in the receptive field center and surround across primate RGC types from three perspectives. First, by probing sensitivity of the receptive field center to expanding motion, a motion type generated when a primate moves through its environment or as objects move toward an observer (**Chapter 2**). Second, by investigating whether and how motion stimuli in the receptive field surround affects signal integration and encoding properties of non-motion stimuli in the receptive field center (**Chapters 3 and 4**). Third, by testing how motion drives interactions between the center and surround to alter stimulus selectivity (**Chapter 3**). A critical finding in this thesis includes the striking sensitivity to motion by the On smooth monostratified RGC across both its receptive field center and surround. The receptive field center of the On smooth monostratified RGC was more sensitive to approaching motion than receding motion (Figure 2.6). Motion in the receptive field surround of the On smooth monostratified RGC made its receptive field center more sensitive to non-motion inputs (Figure 3.4), a previously unreported phenomenon in any RGC type regardless of species. Sensitization of the receptive field center as a function of motion in the receptive field surround also extended to the midget ganglion cell (Figure 4.10), although whether the midget receptive field surround is sensitive to surround motion over other spatio-temporally varying stimulus inputs is not yet clear. In the following sections, I outline the significance of my findings in the larger context of primate visual perception, and consider future courses of research based on the results in this thesis.

5.1 Motion as a Driver of Adaptation

Chapters 3 and 4 outline two intriguing discoveries in the primate retina. One, that primate RGC surrounds contains mechanisms that sensitize their receptive field centers to visual input, opposite to the expected interaction of classical center-surround antagonism (Figures 3.4 and 4.1). Two, that this mechanism is only seen when stimuli vary their inputs over space and/or time, and center-surround antagonism prevails for static inputs (Figure 3.1). Importantly, this occurs on a cell-type basis, reflecting the functional needs of each cell type. In the midget RGC pathway, sensitization to contrast is important for encoding the wide spectrum of spatial contrasts encountered across a natural scene (Figure 4.9)

In non-primate retina, surround-facilitated sensitization has been well characterized [90, 92, 91, 93]. The mechanism of sensitization (adaptation of tonic amacrine cell inhibition to bipolar cells, Figure 4.8) that we found in the midget RGC is shared with sensitizing RGCs in non-primate [90, 93]. We did not find midget ganglion cells with surrounds that showed classical adaptation (of the cell output) to contrast-varying or motion inputs, indicating that, at least in the case of the midget RGC, an adapting and sensitizing pair of RGCs is unnecessary for visual encoding. Instead, sensitization seems specific to the function of midget RGCs, which is long thought to be part of the pathway involved in spatial detail and color [234, 111]. Indeed, we show that surround sensitization in the midget is achromatic, but can still sensitize to color inputs (Figure 4.6).

Because Midget RGC sensitization was elicited by both eye movements and simple temporal flicker, the sensitization mechanism is somewhat non-selective across non-static input types. This may suggest that there are many contexts over which the midget needs to sensitize. Tuning curves of the sensitization mechanism in the midget RGC surround to motion speeds or durations, or the size of any time-varying inputs, could further characterize the functional significance of surround sensitization.

5.2 On Smooth Monostratified RGCs

Sensitivity of the On smooth monostratified cell to motion in the surround was striking and unique (Figure 3.4). The functional consequences of a cell that has its output facilitated specifically by motion in its surround is not clear. Sensitization in the On smooth monostratified cell continued after motion cessation (Figure 3.6), suggesting that the functional implications of sensitization in this cell type may not be inherently motion based, similar to the midget RGC. Moreover, our surround motion stimulus paradigm uses non-motion inputs to the receptive field center to drive a spiking response. However, the On smooth monostratified cell clearly shows sensitization of its outputs for the duration of surround motion (Figure 3.4), and also shows increased output when motion is present in both the center and surround (Figure 3.2). **Chapter 2** also suggests a role for the On smooth monostratified cell in the encoding of visual motion.

Motion sensitivity between center and surround of the On smooth monostratified cell suggest it may be involved in perception of global motion. We show a spiking preference for coherent motion between the On smooth monostratified cell's center and surround (Figure 3.2). Because surround motion drives a facilitated output no matter the type of input in the center, the mechanisms driving motion sensitivity between center and surround are likely different. Abrupt change in center-surround motion sensitivity mechanisms may create discontinuous motion preferences, with consequences for the functional outputs of the cell unclear. Motion sensitivity mechanisms in the surround of the On smooth monostratified cell, and the mechanism for facilitation of the center's output, could reveal the functional consequence of motion sensitivity in the cell.

The receptive field center of smooth monostratified RGCs is spatially heterogeneous. Local regions of bipolar cell input produce distinct spike waveforms along the cell's dendrites, the functional significance of which is not known [140, 49]. A clear area for further study is to associate these spatially distinct inputs with the On smooth monostratified cell's affinity for motion in its receptive field center and surround (**Chapters 2 and 3**). Given unique generation of spike wave-

forms at each site of local input in the smooth monostratified cell center receptive field, it may be that the modulation dynamics of surround motion are also unique across each input site. Temporal correlations across input sites may play a role in integration of spiking waveforms, possibly molding sensitivity to motion in the receptive field center.

5.3 Broad Thorny RGCs

The broad thorny RGC showed a preference for differential motion between its center and surround (Figure 3.2). This type of selectivity has been well documented across non-primate RGCs [66, 67, 201, 141]. The mechanism driving a preference for differential motion has been attributed to the speed of signaling between center and surround [66], as well as the spread of inhibitory input by gap junctioned amacrine cells during coherent motion between center and surround [67]. The circuit mechanisms driving differential motion selectivity in the broad thorny pathway are of great interest, and a clear direction for future work.

The broad thorny's preference for differential motion could have multiple functional implications. Responding preferentially to motion in the center that is discontinuous with the surround could be used as a tracking mechanism during smooth pursuit. Smooth pursuit occurs when the eye is actively fixating on a moving object [235]. Corrective eye movements are used to follow an object being tracked by the eye. Differential motion could be used as an error signal for when the eye needs to initiate a movement to keep the object within the fixation point. Experiments designed to test the tracking of an object, particularly across populations of broad thorny RGCs, could elucidate a role for the cell in smooth pursuit tracking.

Broad thorny RGCs project to the superior colliculus [149]. The superior colliculus has been implicated in the detection of relative motion [104, 105]. Relative motion-sensitive neurons of the superior colliculus respond best when motion between the background and the center moves differentially (often in opposite directions) and with different speeds [104]. Superior colliculus

cells that are most sensitive to relative motion are located in the lower superficial layers (i.e. further from the retinotectal input layers) [104]. When inputs from cortex to the superior colliculus are severed, most relative motion sensitivity in the superior colliculus is removed, but differential motion selectivity remains. It may be that the broad thorny confers some of its differential motion sensitivity to the superior colliculus.

We show that broad thorny RGCs are selective for differential motion between center and surround, but we did not measure dependency on speed or direction. In our recordings, the broad thorny RGCs are not direction selective, and their speed tuning relative to differential motion preference was not tested. Moreover, relative direction of motion between center and surround has not been tested in the broad thorny. Testing the broad thorny's sensitivity to relative speeds and directions of motion between center and surround may give more specific characterization of motion selectivity within the cell.

5.4 Primate RGCs and Naturalistic Motion

Optic flow is generated during self motion, where the visual world travels towards and around the observer. The importance of optic flow to the primate visual system is reflected in the gamut of neurons across brain areas that are selective for optic flow patterns [148, 132, 133]. Our investigations indicate that multiple primate RGC types are sensitive to approaching motion, a motion type with similarities to optic flow ([236], **Chapter 2**). Approaching motion is a more rudimentary version of the complex optic flow fields that drive outputs of visual neurons in the cortex. Optic flow during primate locomotion and navigation involves combinations of expansion, contraction, rotation, and translation [127].

We show that a pair of Off and On primate RGCs is enough for a decoder downstream of the retina to know whether approaching motion or receding motion is being encoded Figure 2.4. That information does not tell the brain whether an optic flow field is vortexing or shearing, rotating

or dilating. It also does not necessarily describe the content of the objects that are approaching (i.e. their size, relative contrast, color, or depth), although object expansion can be used to extract motion information [146]. As of now, the characterization is simply: is something coming toward an area of the retina?

Optic flow dynamics also change the flow patterns across the eye. During walking, the rate of motion flow changes as a function of location in the retina. Upper visual fields tend to experience faster motion than lower visual fields [237]. The visual system also encodes optic flow information on a location-basis for perturbations like rotation and expansion [133]. Testing motion sensitivity within an RGC type across retinal locations could yield interesting insights into whether some RGC types are tuned for the differences in motion generated during naturalistic behaviors like walking or swinging through trees.

Another useful investigation would be to test whether certain RGC populations are specialized for extracting specific features from optic flow that are especially relevant for primate behavior and survival. For example, some RGCs may be tuned to detect sudden looming objects signaling impending collision, while others may preferentially encode global motion patterns indicative of self-motion speed or heading direction. Relative motion between objects and the observer is critical for an animal's survival [129], indicating a need to measure self motion speed and heading relative to motion of a moving object. What aspects of global motion does the retina encode, and how might single RGC types and RGC populations play a role in complex optic flow percepts? These are questions that may guide future work.

5.5 Computational complexity in the primate retina

The primate retina is sometimes viewed as a collection of spatial, temporal, and spectral filters, largely designed to compress visual inputs so more complex cortical circuits can do the work of constructing the primate's rich visual experience. This tilted view of computational power be-

tween primate visual cortex and primate retina may stem from the growth of the visual cortices during evolutionary divergence of the primate. For example, as social structures and ecological interaction evolved in primates, so did the parvocellular visual system [238]. The magnocellular pathways (and their related dorsal pathway brain regions) are also expanded in primate visual cortex compared to non-primate, likely related to the primate's need to visually guide movements for reaching, self defense, and manipulation of tools [239]. This combination of evolutionary expansion and complex computation in primate visual cortex may have put the primate retina on the back foot in terms of presumed computational power. On the other hand, the same evolutionary pressures that expanded the visual cortices may also have influenced the creation of complex visual pathways in the retina, or even necessitated it. Indeed, the motion sensitivities of primate RGCs presented in this thesis, along with the recent discovery of a direction selective primate RGC [210], suggest that the primate retina has the capacity for at least some of the visual computations previously assigned only to the cortex. With so many RGC types yet to be characteriezed physiologically, it is tempting to believe that we have only scratched the surface of computational complexity in the primate retina.

Bibliography

[1] King Wai Yau and Roger C. Hardie. 2009. Phototransduction Motifs and Variations. *Cell*, 139(2):246–264.

[2] Marcos L. Aranda and Tiffany M. Schmidt. 2021. Diversity of intrinsically photosensitive retinal ganglion cells: circuits and functions.

[3] Felice A. Dunn and Rachel O.L. Wong. 2014. Wiring patterns in the mouse retina: Collecting evidence across the connectome, physiology and light microscopy.

[4] Kenneth C Wikler and Robert W Williams. 1990. Photoreceptor Mosaic: Number and Distribution of Rods and Cones in the Rhesus Monkey Retina. *THE JOURNAL OF COMPARATIVE NEUROLOGY*, pages 292499–508.

[5] Julie H Sandell and Alan Peters. 2001. Effects of Age on Nerve Fibers in the Rhesus Monkey Optic Nerve. *J. Comp. Neurol*, 429:541–553.

[6] Heinz Wässle and Brian B Boycott. 1991. Functional Architecture of the Mammalian Retina. *Physiological Reviews*, 71(2).

[7] Rania A. Masri, Kumiko A. Percival, Amane Koizumi, Paul R. Martin, and Ulrike Grünert. 2019. Survey of retinal ganglion cell morphology in marmoset. *Journal of Comparative Neurology*, 527(1):236–258.

[8] Yi Rong Peng, Karthik Shekhar, Wenjun Yan, Dustin Herrmann, Anna Sappington, Gregory S. Bryman, Tavé van Zyl, Michael Tri H. Do, Aviv Regev, and Joshua R. Sanes. 2019. Molecular Classification and Comparative Taxonomics of Foveal and Peripheral Cells in Primate Retina. *Cell*, 176(5):1222–1237.

[9] C. S. Sherrington. 1906. Observations on the scratch-reflex in the spinal dog. *The Journal of Physiology*, 34(1-2):1–50.

[10] D. H. Hubel and T. N. Wiesel. 1960. Receptive fields of optic nerve fibres in the spider monkey. *The Journal of Physiology*, 154(3):572–580.

[11] F M De Monasterio. 1978. Properties of Concentrically Organized X and Y Ganglion Cells of Macaque Retina. *JOURNALOF NEUROPHYSIOLOGY*, 41(6).

[12] F M De Monasterio. 1978. Properties of Ganglion Cells With Atypical Receptive-Field Organization in Retina of Macaques. *JOURNALOF NEUROPHYSIOLOGY*, 41(6).

[13] KUFFLER SW. 1953. Discharge patterns and functional organization of mammalian retina. *J. Neurophysiol*, 16(1):37–68.

[14] W R Levick. 1967. Receptive fields and trigger features of ganglion cells in the visual streak of the rabbit's retina. *J. Physiol*, 188:285–307.

[15] Y D Marr A N and D E Hildreth. 1980. Theory of edge detection. *Proc. R. Boc. Lond. B*, 207:187–217.

[16] Jon Cafaro and Fred Rieke. 2013. Regulation of spatial selectivity by crossover inhibition. *Journal of Neuroscience*, 33(15):6310–6320.

[17] Maxwell H. Turner and Fred Rieke. 2016. Synaptic rectification controls nonlinear spatial integration of natural visual inputs. *Neuron*, 90(6):1257–1271.

[18] Maxwell H. Turner, Gregory W. Schwartz, and Fred Rieke. 2018. Receptive field center-surround interactions mediate context-dependent spatial contrast encoding in the retina. *Elife*, 7:e38841.

[19] F. M. De Monasterio and P. Gouras. 1975. Functional properties of ganglion cells of the rhesus monkey retina. *J. Physiol.*, 251(1):167–195.

[20] Joanna D. Crook, Michael B. Manookin, Orin S. Packer, and Dennis M. Dacey. 2011. Horizontal cell feedback without cone type-selective inhibition mediates "red-green" color opponency in midget ganglion cells of the primate retina. *J. Neurosci.*, 31(5):1762–1772.

[21] Peter H Schiller and Joseph G Malpeli. 1978. Functional Specificity of Lateral Geniculate Nucleus Laminae of the Rhesus Monkey. *Journal of Neurophysiology*, 41(3).

[22] Schiller Peter H. and Logothetis Nikos K. 1990. The color-opponent and broad-band channels of the primate visual system. *Trends in Neuroscience*, 13(10):392–398.

[23] William H Merigan, Carey E Byrne, and Maunsel John H R. 1991. Does Primate Motion Perception Depend on the Magnocellular Pathway? *The Journal of Neuroscience*, 11(11):3422–3429.

[24] Audie G Leventhal, R W Rodieck, and B Dreher. 1981. Retinal ganglion cell classes in the Old World monkey: morphology and central projections. *New Series*, 213(4512):1139–1142.

[25] Michael B. Manookin, Sara S. Patterson, and Conor M. Linehan. 2018. Neural mechanisms mediating motion sensitivity in parasol ganglion cells of the primate retina. *Neuron*, 97(6):1327–1340.

[26] E. J. Chichilnisky and R. S. Kalmar. 2003. Temporal resolution of ensemble visual motion signals in primate retina. *J. Neurosci.*, 23(17):6681–6689.

[27] E. S. Frechette, A. Sher, M. I. Grivich, D. Petrusca, A. M. Litke, and E. J. Chichilnisky. 2005. Fidelity of the ensemble code for visual motion in primate retina. *Journal of Neurophysiology*, 94(1):119–135.

[28] Joanna D. Crook, Beth B. Peterson, Orin S. Packer, Farrel R. Robinson, Paul D. Gamlin, John B. Troy, and Dennis M. Dacey. 2008. The smooth monostratified ganglion cell: Evidence for spatial diversity in the Y-cell pathway to the lateral geniculate nucleus and superior colliculus in the macaque monkey. *Journal of Neuroscience*, 28(48):12654–12671.

[29] Kumiko A. Percival, Paul R. Martin, and Ulrike Grünert. 2013. Organisation of koniocellular-projecting ganglion cells and diffuse bipolar cells in the primate fovea. *European Journal of Neuroscience*, 37(7):1072–1089.

[30] Christian Puller, Michael B. Manookin, Jay Neitz, Fred Rieke, and Maureen Neitz. 2015. Broad thorny ganglion cells: a candidate for visual pursuit error signaling in the primate retina. *J. Neurosci.*, 35(13):5397–5408.

[31] R. F. Dacheux and E. Raviola. 1990. Physiology of HI horizontal cells in the primate retina. *Proceedings of the Royal Society B: Biological Sciences*, 239(1295):213–230.

[32] Richard H. Masland. 2012. The Neuronal Organization of the Retina. *Neuron*, 76(2):266–280.

[33] Jeffrey S Diamond. 2017. Inhibitory Interneurons in the Retina: Types, Circuitry, and Function *.

[34] Andreas Bringmann, Steffen Syrbe, Katja Görner, Johannes Kacza, Mike Francke, Peter Wiedemann, and Andreas Reichenbach. 2018. The primate fovea: Structure, function and development.

[35] Rebecca L Rockhill, Thomas Euler, Richard H Masland, and Denis Baylor. 2000. Spatial order within but not between types of retinal neurons. *Proc Natl Acad Sci U S A*, 97(5):2303–7.

[36] Paul A. Weber, Hou Chien Chang, Kris E. Spaeth, Johannes M. Nitsche, and Bruce J. Nicholson. 2004. The permeability of gap junction channels to probes of different size is dependent on connexin composition and permeant-pore affinities. *Biophysical Journal*, 87(2):958–973.

[37] Béla Völgyi, Tamás Kovács-öller, Tamás Atlasz, Márta Wilhelm, and Róbert Gábriel. 2013. Gap junctional coupling in the vertebrate retina: Variations on one theme?

[38] Xuegang Luo, Krishna K Ghosh, Paul R Martin, and Ulrike Grünert. 1999. Analysis of two types of cone bipolar cells in the retina of a New World monkey, the marmoset, Callithrix jacchus. *Visual Neuroscience*, 16:707–719.

[39] Roy A Jacoby, Allan F Wiechmann, Susan G Amara, Barbara H Leighton, and David W Marshak. 2000. Diffuse Bipolar Cells Provide Input to OFF Parasol Ganglion Cells in the Macaque Retina. *Journal of Comparative Neurology*, 416(1):6–18.

[40] Orsolya Kántor, Alexandra Varga, Roland Nitschke, Angela Naumann, Anna Énzsöly, Ákos Lukáts, Arnold Szabó, János Németh, and Béla Völgyi. 2017. Bipolar cell gap junctions serve major signaling pathways in the human retina. *Brain Structure and Function*, 222(6):2603–2624.

[41] Dennis Dacey, Orin S Packer, Lisa Diller, David Brainard, Beth Peterson, and Barry Lee. 2000. Center surround receptive field structure of cone bipolar cells in primate retina. *Vision Research*, 40:1801–1811.

[42] Sidney P. Kuo, Gregory W. Schwartz, and Fred Rieke. 2016. Nonlinear Spatiotemporal Integration by Electrical and Chemical Synapses in the Retina. *Neuron*, 90(2):320–332.

[43] Jonathon Shlens, Greg D. Field, Jeffrey L. Gauthier, Matthew I. Grivich, Dumitru Petrusca, Alexander Sher, Alan M. Litke, and E. J. Chichilnisky. 2006. The structure of multi-neuron firing patterns in primate retina. *Journal of Neuroscience*, 26(32):8254–8266.

[44] Martin Greschner, Jonathon Shlens, Constantina Bakolitsa, Greg D. Field, Jeffrey L. Gauthier, Lauren H. Jepson, Alexander Sher, Alan M. Litke, and E. J. Chichilnisky. 2011. Correlated firing among major ganglion cell types in primate retina. *Journal of Physiology*, 589(1):75–86.

[45] Yoshihiko Tsukamoto and Naoko Omi. 2015. OFF bipolar cells in macaque retina: Type-specific connectivity in the outer and inner synaptic layers. *Frontiers in Neuroanatomy*, 9(OCT).

[46] Yoshihiko Tsukamoto and Naoko Omi. 2016. ON bipolar cells in macaque retina: Type-specific synaptic connectivity with special reference to OFF counterparts. *Frontiers in Neuroanatomy*, 10.

[47] Steven H Devries. 2000. Bipolar Cells Use Kainate and AMPA Receptors to Filter Visual Information into Separate Channels. *Neuron*, 28:847–856.

[48] Thomas Euler, Silke Haverkamp, Timm Schubert, and Tom Baden. 2014. Retinal bipolar cells: Elementary building blocks of vision.

[49] Sara S. Patterson, Rebecca J. Girresch, Marcus A. Mazzaferri, Andrea S. Bordt, Wendy L. Piñon-Teal, Brett D. Jesse, Dinukie Chantal W. Perera, Melanie A. Schlepphorst, James A. Kuchenbecker, Alice Z. Chuang, Jay Neitz, David W. Marshak, and Judith Mosinger Ogilvie. 2024. Synaptic Origins of the Complex Receptive Field Structure in Primate Smooth Monostratified Retinal Ganglion Cells. *eNeuro*, 11(1).

[50] Jonathan B. Demb, Loren Haarsma, Michael A. Freed, and Peter Sterling. 1999. Functional circuitry of the retinal ganglion cell's nonlinear receptive field. *Journal of Neuroscience*, 19(22):9756–9767.

[51] Jonathan B Demb, Kareem Zaghloul, Loren Haarsma, and Peter Sterling. 2001. Bipolar

Cells Contribute to Nonlinear Spatial Summation in the Brisk-Transient (Y) Ganglion Cell in Mammalian Retina. *The Journal of Neuroscience*, 19(21):7447–7454.

[52] Greg Schwartz and Fred Rieke. 2011. Nonlinear spatial encoding by retinal ganglion cells: When 1 + 1 2.

[53] Christina Enroth-Cugell and J. G. Robson. 1966. The contrast sensitivity of retinal ganglion cells of the cat. *The Journal of Physiology*, 187(3):517–552.

[54] S Hochstein and R.M. Shapely. 1976. Linear and Nonlinear Spatial Subunits in Y Cat Retinal Ganglion Cells. *The Journal of Physiology*, 262:265–284.

[55] Dumitru Petrusca, Matthew I. Grivich, Alexander Sher, Greg D. Field, Jeffrey L. Gauthier, Martin Greschner, Jonathon Shlens, E. J. Chichilnisky, and Alan M. Litke. 2007. Identification and characterization of a Y-like primate retinal ganglion cell type. *Journal of Neuroscience*, 27(41):11019–11027.

[56] Dennis M Dacey. 1989. Axon-Bearing Amacrine Cells of the Macaque Monkey Retina. *The Journal of Comparative Neurology*, pages 284275–293.

[57] Christopher M Davenport, Peter B Detwiler, and Dennis M Dacey. 2007. Functional polarity of dendrites and axons of primate A1 amacrine cells. *Visual Neuroscience*, 24:449–457.

[58] Andrew P. Mariani. 1990. Amacrine cells of the rhesus monkey retina. *The Journal of Comparative Neurology*, 301(3):382–400.

[59] Sara S Patterson, Andrea S Bordt, Rebecca J Girresch, | Conor, M Linehan, Jacob Bauss, Eunice Yeo, Diego Perez, | Luke Tseng, Sriram Navuluri, Nicole B Harris, Chaiss Matthews, James R Anderson, James A Kuchenbecker, Michael B Manookin, Judith M Ogilvie, | Jay Neitz, | David, W Marshak, and David W Marshak. 2019. Wide-field amacrine cell inputs to ON parasol ganglion cells in macaque retina.

[60] Andrea S Bordt, Sara S Patterson, Rebecca J Girresch, Diego Perez, | Luke Tseng, James R Anderson, Marcus A Mazzaferri, James A Kuchenbecker, Rodrigo Gonzales-Rojas, | Ashley Roland, Charis Tang, | Christian Puller, Alice Z Chuang, | Judith, Mosinger Ogilvie, | Jay Neitz, | David, W Marshak, and S Bordt. 2021. Synaptic inputs to broad thorny ganglion cells in macaque retina.

[61] Andrea S Bordt, Sara S Patterson, James A Kuchenbecker, Marcus A Mazzaferri, Joel N Yearick, Emma R Yang, Judith Mosinger Ogilvie, Jay Neitz, and David W Marshak. 123. Synaptic inputs to displaced intrinsically-photosensitive ganglion cells in macaque retina.

[62] Martin Greschner, Greg D. Field, Peter H. Li, Max L. Schiff, Jeffrey L. Gauthier, Daniel Ahn, Alexander Sher, Alan M. Litke, and E. J. Chichilnisky. 2014. A polyaxonal amacrine cell population in the primate retina. *Journal of Neuroscience*, 34(10):3597–3606.

[63] Michael B. Manookin, Christian Puller, Fred Rieke, Jay Neitz, and Maureen Neitz. 2015. Distinctive receptive field and physiological properties of a wide-field amacrine cell in the macaque monkey retina. *J. Neurophysiol.*, 114(3):1606–1616.

[64] Paul B. Cook and John S. McReynolds. 1998. Lateral inhibition in the inner retina is important for spatial tuning of ganglion cells. *Nature Neuroscience*, 1(8):714–719.

[65] Paul B. Cook, Peter D. Lukasiewicz, and John S. McReynolds. 1998. Action potentials are required for the lateral transmission of glycinergic transient inhibition in the amphibian retina. *J. Neurosci.*, 18(6):2301–2308.

[66] Bence P. Ölveczky, Stephen A. Baccus, and Markus Meister. 2003. Segregation of object and background motion in the retina. *Nature*, 423(6938):401–408.

[67] Stephen A Baccus, Bence P Olveczky, Mihai Manu, and Markus Meister. 2008. A retinal circuit that computes object motion. *The Journal of neuroscience : the official journal of the Society for Neuroscience*, 28(27):6807–17.

[68] Thomas A. Münch, Rava Azeredo Da Silveira, Sandra Siegert, Tim James Viney, Gautam B. Awatramani, and Botond Roska. 2009. Approach sensitivity in the retina processed by a multifunctional neural circuit. *Nature Neuroscience*, 12(10):1308–1316.

[69] Jamie Johnston, Sofie Helene Seibel, Léa Simone Adele Darnet, Sabine Renninger, Michael Orger, and Leon Lagnado. 2019. A Retinal Circuit Generating a Dynamic Predictive Code for Oriented Features. *Neuron*, 102(6):1211–1222.

[70] William N Grimes, Jun Zhang, Hua Tian, Cole W Graydon, Mrinalini Hoon, Fred Rieke, and Jeffrey S Diamond. 2015. Complex inhibitory microcircuitry regulates retinal signaling near visual threshold. *J Neurophysiol*, 114:341–353.

[71] Heinz Wässle. 2004. Parallel processing in the mammalian retina. *Nature Reviews Neuroscience*, 5(10):747–757.

[72] Michael B. Manookin, Deborah Langrill Beaudoin, Zachary Raymond Ernst, Leigh J. Flagel, and Jonathan B. Demb. 2008. Disinhibition combines with excitation to extend the operating range of the off visual pathway in daylight. *Journal of Neuroscience*, 28(16):4136–4150.

[73] Qiang Chen, Robert G. Smith, Xiaolin Huang, and Wei Wei. 2020. Preserving inhibition with a disinhibitory microcircuit in the retina. *eLife*, 9:1–20.

[74] J T Woodward, K R Turpie, T C Stone, S A Gadsden, A Newton, S E Maxwell, S E Grantham, T C Larason, and S W Brown. 2022. Measurements of absolute, SI-traceable lunar irradiance with the Airborne LUnar Spectral Irradiance (air-LUSI) instrument. *Metrologia*, 59.

[75] A. L. Fairhall, G. D. Lewen, W. Bialek, and R. R. De Ruyter van Steveninck. 2001. Efficiency and ambiguity in an adaptive neural code. *Nature*, 412(6849):787–792.

[76] R. Angus Silver. 2010. Neuronal arithmetic. *Nature Reviews Neuroscience*, 11(7):474–489.

[77] Stelios M. Smirnakis, Michael J. Berry, David K. Warland, William Bialek, and Markus Meister. 1997. Adaptation of retinal processing to image contrast and spatial scale. *Nature*, 386(6620):69–73.

[78] Kerry J Kim and Fred Rieke. 2001. Temporal Contrast Adaptation in the Input and Output Signals of Salamander Retinal Ganglion Cells. *The Journal of Neuroscience*, 21(1):287–299.

[79] Stephen A. Baccus and Markus Meister. 2002. Fast and slow contrast adaptation in retinal circuitry. *Neuron*, 36(5):909–919.

[80] Michael B. Manookin and Jonathan B. Demb. 2006. Presynaptic mechanism for slow contrast adaptation in mammalian retinal ganglion cells. *Neuron*, 50(3):453–464.

[81] Fred Rieke and Michael E. Rudd. 2009. The Challenges Natural Images Pose for Visual Adaptation.

[82] Barry Wark, Adrienne Fairhall, and Fred Rieke. 2009. Timescales of inference in visual adaptation. *Neuron*, 61(5):750–761.

[83] Felice A. Dunn, Martin J. Lankheet, and Fred Rieke. 2007. Light adaptation in cone vision involves switching between receptor and post-receptor sites. *Nature*, 449(7162):603–606.

[84] Kerry J. Kim and Fred Rieke. 2001. Temporal contrast adaptation in the input and output signals of salamander retinal ganglion cells. *J. Neurosci.*, 21(1):287–299.

[85] Ethan A. Benardete, Ehud Kaplan, and Bruce W. Knight. 1992. Contrast gain control in the primate retina: P cells are not x-like, some M cells are. *Vis. Neurosci.*, 8(5):483–486.

[86] Ethan A. Benardete and Ehud Kaplan. 1999. The dynamics of primate M retinal ganglion cells. *Visual Neuroscience*, 16(2):355–368.

[87] Samuel G Solomon, Jonathan W Peirce, Neel T Dhruv, and Peter Lennie. 2004. Profound Contrast Adaptation Early in the Visual Pathway. *Neuron*, 42:155–162.

[88] Ehud Kaplan, Barry B Lee, and Robert M Shapley. 1990. New Views of Primate Retinal Function. *Progress in Retinal Research*, 9(C):273–336.

[89] Divya Chander and E. J. Chichilnisky. 2001. Adaptation to temporal contrast in primate and salamander retina. *J. Neurosci.*, 21(24):9904–9916.

[90] David B. Kastner and Stephen A. Baccus. 2011. Coordinated dynamic encoding in the retina using opposing forms of plasticity. *Nat. Neurosci.*, 14(10):1317–1322.

[91] Anton Nikolaev, Kin Mei Leung, Benjamin Odermatt, and Leon Lagnado. 2013. Synaptic mechanisms of adaptation and sensitization in the retina. *Nat. Neurosci.*, 16(7):934–941.

[92] David B. Kastner and Stephen A. Baccus. 2013. Spatial segregation of adaptation and predictive sensitization in retinal ganglion cells. *Neuron*, 79(3):541–554.

[93] David B. Kastner, Yusuf Ozuysal, Georgia Panagiotakos, and Stephen A. Baccus. 2019. Adaptation of Inhibition Mediates Retinal Sensitization. *Current Biology*, 29(16):2640–2651.

[94] Jacob Richter and Shimon Ullman. 1982. A model for the temporal organization of X- and Y-type receptive fields in the primate retina. *Biol. Cybern*, 43:127–145.

[95] R A Linsenmeier, L J Frishman, H G Jakrfut, and C Enroth-Cugell. 1982. Receptive field properties of X and Y cells in the cat retina derived from contrast sensitivity measurements. *Vision Res*, 22:173–1183.

[96] James J Dicarlo, Kenneth O Johnson, and Steven S Hsiao. 1998. Structure of Receptive Fields in Area 3b of Primary Somatosensory Cortex in the Alert Monkey.

[97] R W Rodieck and J Stone. 1965. ANALYSIS OF RECEPTIVE FIELDS OF CAT RETINAL GANGLION CELLS. *J. Neurophysiol.*, 28(5):833–849.

[98] Francesco Trapani, Giulia Spampinato, Pierre Yger, and Olivier Marre. 2022. Differences in non-linearities determine retinal cell types.

[99] E. J. Chichilnisky. 2001. A simple white noise analysis of neuronal light responses. *Network*, 12(2):199–213.

[100] Kareem A Zaghloul, Kwabena Boahen, and Jonathan B Demb. 2003. Different Circuits for ON and OFF Retinal Ganglion Cells Cause Different Contrast Sensitivities. *The Journal of Neuroscience*, 21(1):287–299.

[101] Alexander Heitman, Nora Brackbill, Martin Greschner, Alexander Sher, Alan M Litke, and E J Chichilnisky. 2016. Testing pseudo-linear models of responses to natural scenes in primate retina. *bioRxiv*.

[102] Tim Gollisch. 2013. Features and functions of nonlinear spatial integration by retinal ganglion cells.

[103] D B Bender and R M Davidson. 1986. Global visual processing in the monkey superior colliculus. *Brain Research*, 381:372–375.

[104] R M Davidson and D B Bender. 1991. Selectivity for Relative Motion in the Monkey Superior Colliculus. *Journal of Neurophysiology*, 65(5):1115–1133.

[105] TJ Joly and DB Bender. 1997. Loss of relative-motion sensitivity in the monkey superior colliculus after lesions of cortical area MT. *Experimental Brain Research*, 117:43–58.

[106] Richard T. Born and David C. Bradley. 2005. Structure and function of visual area MT.

[107] Karen K De Valois, Russell L De, E William Yund, K K De Valois, R L De, and E W Yund. 1979. Responses of striate cortex cells to grating and checkerboard patterns. *Journal of Physiology*, 291:483–505.

[108] Margaret Livingstone. 1998. Mechanisms of Direction Selectivity in Macaque V1. *Neuron*, 20:509–526.

[109] Cheng Wang and Haishan Yao. 2011. Sensitivity of V1 neurons to direction of spectral motion. *Cerebral Cortex*, 21(4):964–973.

[110] Martin Y. Villeneuve, Ron Kupers, Albert Gjedde, Maurice Ptito, and Christian Casanova. 2005. Pattern-motion selectivity in the human pulvinar. *NeuroImage*, 28(2):474–480.

[111] Mortimer Mishkin, Leslie G Ungerleider, and Kathleen A Macko. 1983. Object vision and spatial vision:two cortical pathways. *Trends in Neuroscience*, 6:414–417.

[112] Margaret Livingstone and David Hubel. 1988. Segregation of Form, Color, Movement, and Depth: Anatomy, Physiology, and Perception. *Science*, 240(4853):740–749.

[113] J. L. Schnapf, B. J. Nunn, M. Meister, and D. A. Baylor. 1990. Visual transduction in cones of the monkey macaca fascicularis. *J. Physiol.*, 427(1):681–713.

[114] Melvyn A. Goodale and A. David Milner. 1992. Separate visual pathways for perception and action. *Trends in Neurosciences*, 15(1):20–25.

[115] Ulrike Grünert and Paul R. Martin. 2020. Cell types and cell circuits in human and non-human primate retina.

[116] V H Perry, R Oehler, and A Cowey. 1984. Retinal ganglion cells that project to the dorsal lateral geniculate nucleus in the macaque monkey. *The Journal of Neuroscience*, I(4):1101.

[117] Dennis Dacey, Beth Peterson, Farrell Robinson, and Paul Gamlin. 2003. Neurotechnique Fireworks in the Primate Retina: In Vitro Photodynamics Reveals Diverse LGN-Projecting Ganglion Cell Types. *Neuron*, 37:15–37.

[118] Daniel Hillier, Michele Fiscella, Antonia Drinnenberg, Stuart Trenholm, Santiago B. Rompani, Zoltan Raics, Gergely Katona, Josephine Juettner, Andreas Hierlemann, Balazs Rozsa, and Botond Roska. 2017. Causal evidence for retina-dependent and -independent visual motion computations in mouse cortex. *Nature Neuroscience*, 20(7):960–968.

[119] Michele Rucci and Jonathan D. Victor. 2015. The unsteady eye: An information-processing stage, not a bug. *Trends in Neurosciences*, 38(4):195–206.

[120] Xutao Kuang, Martina Poletti, Jonathan D. Victor, and Michele Rucci. 2012. Temporal encoding of spatial information during active visual fixation. *Current Biology*, 22(6):510–514.

[121] Lorrin A Riggs, Floyd Ratliff, Janet C Cornsweet, and Tom N Cornsweet. 1953. The Disappearance of Steadily Fixated Visual Test Objects. *Journal of the Optical Society of America*, 43(6):495–500.

[122] John K Stevens, Robert C Emerson, George L Gerstein, Tamas Kallos, Gordon Neufeld, Charles W Nichols, and Alan C Rosexquist. 1976. Paralysis of the awake human: visual perceptions. *Vision Research*, 16:93–98.

[123] Michele Rucci, Ramon Iovin, Martina Poletti, and Fabrizio Santini. 2007. Miniature eye movements enhance fine spatial detail. *Nature*, 447(7146):851–854.

[124] Martin Greschner, Markus Bongard, Pal Rujan, and Josef Ammermüller. 2002. Retinal ganglion cell synchronization by fixational eye movements improves feature estimation. *Nature Neuroscience*, 5(4):341–347.

[125] Jeffrey D Schall and Kirk G Thompson. 1998. Neural selection and control of visually guided eye movements.

[126] David Solomon and Bernard Cohen. 1992. Stabilization of Gaze During Circular Locomotion in Light I. Compensatory Head and Eye Nystagmus in the Running Monkey. *Journal of Neurophysiology*, 67(5).

[127] H.C. Longuet-Higgins. 1980. The interpretation of a moving retinal image. Technical report.

[128] Jonathan Samir Matthis, Karl S. Muller, Kathryn L. Bonnen, and Mary M. Hayhoe. 2022. Retinal optic flow during natural locomotion. *PLoS Computational Biology*, 18(2).

[129] Constance S. Royden and Erin M. Connors. 2010. The detection of moving objects by moving observers. *Vision Research*, 50(11):1014–1024.

[130] Brett R Fajen and Jonathan S Matthis. 2013. Visual and Non-Visual Contributions to the Perception of Object Motion during Self-Motion.

[131] Richard Born and Roger Tootell. 1992. Segregation of global and local motion processing in primate middle temporal visual area. *Nature*, 357:497–499.

[132] Charles J Duffy and Robert H Wurtz. 1995. Response of Monkey MST Neurons to Optic Flow Stimuli with Shifted Centers of Motion. *The Journal of Neuroscience*, 15(7):5192–5208.

[133] Nardin Nakhla, Yavar Korkian, Matthew R. Krause, and Christopher C. Pack. 2021. Neural selectivity for visual motion in macaque area v3a. *eNeuro*, 8(1):1–14.

[134] D. H. Hubel and T. N. Wiesel. 1968. Receptive fields and functional architecture of monkey striate cortex. *The Journal of Physiology*, 195(1):215–243.

[135] Keiji Tanaka, Yoichi Sugita, Madoka Moriya, and And Hide-Ak1. 1993. Analysis of Object Motion in the Ventral Part of the Medial Superior Temporal Area of the Macaque Visual Cortex. 69(1):128–142.

[136] Satoshi Eifuku and Robert H Wurtz. 1998. Response to Motion in Extrastriate Area MSTl: Center-Surround Interactions. *Journal of Physiology*, pages 282–295.

[137] Ungsoo Samuel Kim, Omar A. Mahroo, John D. Mollon, and Patrick Yu-Wai-Man. 2021. Retinal Ganglion Cells—Diversity of Cell Types and Clinical Relevance.

[138] Samuel G Solomon, Paul R Martin, Andrew J R White, Lukas R€ U Uttiger B, and Barry B Lee. 2002. Modulation sensitivity of ganglion cells in peripheral retina of macaque. *Vision Research*, 42:2893–2898.

[139] Greg D. Field, Jeffrey L. Gauthier, Alexander Sher, Martin Greschner, Timothy A. MacHado, Lauren H. Jepson, Jonathon Shlens, Deborah E. Gunning, Keith Mathieson, Wladyslaw Dabrowski, Liam Paninski, Alan M. Litke, and E. J. Chichilnisky. 2010. Functional connectivity in the retina at the resolution of photoreceptors. *Nature*, 467(7316):673–677.

[140] Colleen E. Rhoades, Nishal P. Shah, Michael B. Manookin, Nora Brackbill, Alexandra Kling, Georges Goetz, Alexander Sher, Alan M. Litke, and E. J. Chichilnisky. 2019. Unusual Physiological Properties of Smooth Monostratified Ganglion Cell Types in Primate Retina. *Neuron*, 103(4):658–672.

[141] Jason Jacoby and Gregory W. Schwartz. 2017. Three small-receptive-field ganglion cells in the mouse retina are distinctly tuned to size, speed, and object motion. *Journal of Neuroscience*, 37(3):610–625.

[142] W. Schiff and M. L. Detwiler. 1979. Information used in judging impending collision. *Perception*, 8(6):647–658.

[143] D. N. Lee. 1976. A theory of visual control of braking based on information about time to collision. *Perception*, 5(4):437–459.

[144] Mary K. Kaiser and Heiko Hecht. 1995. Time-to-passage judgments in nonconstant optical flow fields. *Perception & Psychophysics*, 57(6):817–825.

[145] Colin W.G. Clifford, Scott A. Beardsley, and Lucia M. Vaina. 1999. The perception and discrimination of speed in complex motion. *Vision Research*, 39(13):2213–2227.

[146] Paul R. Schrater, David C. Knill, and Eero P. Simoncelli. 2001. Perceiving visual expansion without optic flow. *Nature*, 410(6830):816–819.

[147] G. A. Orban, L. Lagae, A. Verri, S. Raiguel, D. Xiao, H. Maes, and V. Torre. 1992. First-order analysis of optical flow in monkey brain. *Proceedings of the National Academy of Sciences of the United States of America*, 89(7):2595–2599.

[148] C. J. Duffy and R. H. Wurtz. 1991. Sensitivity of MST neurons to optic flow stimuli. I. A continuum of response selectivity to large-field stimuli. *Journal of Neurophysiology*, 65(6):1329–1345.

[149] R. W. Rodieck and M. Watanabe. 1993. Survey of the morphology of macaque retinal ganglion cells that project to the pretectum, superior colliculus, and parvicellular laminae of the lateral geniculate nucleus. *J. Comp. Neurol.*, 338(2):289–303.

[150] Ehud Kaplan and Robert M Shapley. 1986. The primate retina contains two types of ganglion cells, with high and low contrast sensitivity (spatial vison/visual neurons/macaque monkey). *Proc. Natl. Acad. Sci*, 83:2755–2757.

[151] Barry B. Lee, Christian Wehrhahn, Gerald Westheimer, and Jan Kremers. 1995. The spatial precision of macaque ganglion cell responses in relation to vernier acuity of human observers. *Vision Research*, 35(19):2743–2758.

[152] M. Watanabe and R. W. Rodieck. 1989. Parasol and midget ganglion cells of the primate retina. *Journal of Comparative Neurology*, 289(3):434–454.

[153] Dennis Dacey, Orin S. Packer, Lisa Diller, David Brainard, Beth Peterson, and Barry Lee. 2000. Center surround receptive field structure of cone bipolar cells in primate retina. *Vision Research*, 40(14):1801–1811.

[154] B. B. Boycott and H. Wässle. 1991. Morphological Classification of Bipolar Cells of the Primate Retina. *European Journal of Neuroscience*, 3(11):1069–1088.

[155] David J. Field. 1987. Relations between the statistics of natural images and the response properties of cortical cells. *Journal of the Optical Society of America A*, 4(12):2379.

[156] Dawei Dong and Joseph Atick. 1995. Statistics of natural time-varying images. *Network: Computation in Neural Systems*, 6(3):345–358.

[157] Gregory W. Schwartz, Haruhisa Okawa, Felice A. Dunn, Josh L. Morgan, Daniel Kerschensteiner, Rachel O. Wong, and Fred Rieke. 2012. The spatial structure of a nonlinear receptive field. *Nature Neuroscience*, 15(11):1572–1580.

[158] Dominik M. Endres and Johannes E. Schindelin. 2003. A new metric for probability distributions. *IEEE Transactions on Information Theory*, 49(7):1858–1860.

[159] Ferdinand Österreicher and Igor Vajda. 2003. A new class of metric divergences on probability spaces and its applicability in statistics. *Annals of the Institute of Statistical Mathematics*, 55(3):639–653.

[160] T. Kujiraoka and T. Saito. 1986. Electrical coupling between bipolar cells in carp retina. *Proceedings of the National Academy of Sciences of the United States of America*, 83(11):4063–4066.

[161] Takehik Saito and Toru Kujiraoka. 1988. Characteristics of bipolar-bipolar coupling in the carp retina. *Journal of General Physiology*, 91(2):275–287.

[162] Amy Berntson and W. Rowland Taylor. 2000. Response characteristics and receptive field widths of on-bipolar cells in the mouse retina. *Journal of Physiology*, 524(3):879–889.

[163] Jon Cafaro and Fred Rieke. 2010. Noise correlations improve response fidelity and stimulus encoding. *Nature*, 468(7326):964–967.

[164] Zhiyin Liang and Michael A. Freed. 2010. The ON pathway rectifies the off pathway of the mammalian retina. *Journal of Neuroscience*, 30(16):5533–5543.

[165] Malcolm M. Slaughter and Robert F. Miller. 1981. 2-Amino-4-phosphonobutyric acid: A new pharmacological tool for retina research. *Science*, 211(4478):182–185.

[166] Petri Ala-Laurila, Martin Greschner, E. J. Chichilnisky, and Fred Rieke. 2011. Cone photoreceptor contributions to noise and correlations in the retinal output. *Nature Neuroscience*, 14(10):1309–1316.

[167] Gabe J. Murphy and Fred Rieke. 2008. Signals and noise in an inhibitory interneuron diverge to control activity in nearby retinal ganglion cells. *Nature Neuroscience*, 11(3):318–326.

[168] Ji Jie Pang, Fan Gao, and Samuel M. Wu. 2007. Cross-talk between ON and OFF channels in the salamander retina: Indirect bipolar cell inputs to ON-OFF ganglion cells. *Vision Research*, 47(3):384–392.

[169] Michiel Van Wyk, Heinz Wässle, and W. Rowland Taylor. 2009. Receptive field properties of ON- and OFF-ganglion cells in the mouse retina. *Visual Neuroscience*, 26(3):297–308.

[170] Alyosha Molnar, Hain Ann Hsueh, Botond Roska, and Frank S. Werblin. 2009. Crossover inhibition in the retina: Circuitry that compensates for nonlinear rectifying synaptic transmission. *Journal of Computational Neuroscience*, 27(3):569–590.

[171] E. J. Chichilnisky and Rachel S. Kalmar. 2002. Functional Asymmetries in ON and OFF Ganglion Cells of Primate Retina. *Journal of Neuroscience*, 22(7):2737–2747.

[172] Stuart Trenholm, David J. Schwab, Vijay Balasubramanian, and Gautam B. Awatramani. 2013. Lag normalization in an electrically coupled neural network. *Nature Neuroscience*, 16(2):154–156.

[173] Alex Hoggarth, Amanda J. McLaughlin, Kara Ronellenfitch, Stuart Trenholm, Rishi Vasandani, Santhosh Sethuramanujam, David Schwab, Kevin L. Briggman, and Gautam B. Awatramani. 2015. Specific wiring of distinct amacrine cells in the directionally selective retinal circuit permits independent coding of direction and size. *Neuron*, 86(1):276–291.

[174] Tahnbee Kim and Daniel Kerschensteiner. 2017. Inhibitory Control of Feature Selectivity in an Object Motion Sensitive Circuit of the Retina. *Cell Reports*, 19(7):1343–1350.

[175] Cun Jian Dong and Frank S. Werblin. 1998. Temporal contrast enhancement via GABA(c) feedback at bipolar terminals in the tiger salamander retina. *Journal of Neurophysiology*, 79(4):2171–2180.

[176] Saskia E.J. de Vries, Stephen A. Baccus, and Markus Meister. 2011. The projective field of a retinal amacrine cell. *Journal of Neuroscience*, 31(23):8595–8604.

[177] Hiroki Asari and Markus Meister. 2012. Divergence of visual channels in the inner retina. *Nature Neuroscience*, 15(11):1581–1589.

[178] Hiroki Asari and Markus Meister. 2014. The Projective Field of Retinal Bipolar Cells and Its Modulation by Visual Context. *Neuron*, 81(3):641–652.

[179] Heinz Wässle. 2004. Parallel processing in the mammalian retina. *Nat. Rev. Neurosci.*, 5(10):747–757.

[180] Martin Greschner, Alexander K. Heitman, Greg D. Field, Peter H. Li, Daniel Ahn, Alexander Sher, Alan M. Litke, and E. J. Chichilnisky. 2016. Identification of a Retinal Circuit for Recurrent Suppression Using Indirect Electrical Imaging. *Current Biology*, 26(15):1935–1942.

[181] W. Rowland Taylor. 1999. TTX attenuates surround inhibition in rabbit retinal ganglion cells. *Visual Neuroscience*, 16(2):285–290.

[182] Nicolas Flores-Herr, Dario A. Protti, and Heinz Wässle. 2001. Synaptic currents generating the inhibitory surround of ganglion cells in the mammalian retina. *Journal of Neuroscience*, 21(13):4852–4863.

[183] Benjamin N Naecker and Stephen A Baccus. 2018. Long-range sensitization in the vertebrate retina and human perception. *BbioRxiv*.

[184] Todd R. Appleby and Michael B. Manookin. 2019. Neural sensitization improves encoding fidelity in the primate retina. *Nature Communications 2019 10:1*, 10(1):1–15.

[185] Juliana M. Rosa, Sabine Ruehle, Huayu Ding, and Leon Lagnado. 2016. Crossover Inhibition Generates Sustained Visual Responses in the Inner Retina. *Neuron*, 90(2):308–319.

[186] Frank S. Werblin. 2010. Six different roles for crossover inhibition in the retina: Correcting the nonlinearities of synaptic transmission.

[187] Yifeng Zhang, In Jung Kim, Joshua R. Sanes, and Markus Meister. 2012. The most numerous ganglion cell type of the mouse retina is a selective feature detector. *Proceedings of the National Academy of Sciences of the United States of America*, 109(36):E2391–E2398.

[188] Hongjin Sun and Barrie J. Frost. 1998. Computation of different optical variables of looming objects in pigeon nucleus rotundus neurons. *Nature Neuroscience*, 1(4):296–303.

[189] Alexander B. Wiltschko, Gregory J. Gage, and Joshua D. Berke. 2008. Wavelet filtering before spike detection preserves waveform shape and enhances single-unit discrimination. *J. Neurosci. Methods*, 173(1):34–40.

[190] C. Enroth-Cugell, J. G. Robson, D. E. Schweitzer-Tong, and A. B. Watson. 1983. Spatio-temporal interactions in cat retinal ganglion cells showing linear spatial summation. *The Journal of Physiology*, 341(1):279–307.

[191] J. B. Troy, D. L. Bohnsack, and L. C. Diller. 1999. Spatial properties of the cat X-cell receptive field as a function of mean light level. *Visual Neuroscience*, 16(6):1089–1104.

[192] Juan M. Angueyra and Fred Rieke. 2013. Origin and effect of phototransduction noise in primate cone photoreceptors. *Nat. Neurosci.*, 16(11):1692–1700.

[193] HK Hartline. 1938. The Response of Single Optic Nerve Fibers of the Vertebrate Eye to Illumination of the Retina. *American Journal of Physiology*, 121:400–415.

[194] Clay Reid and Robert Shapley. 1992. Spatial structure of cone inputs to receptive fields in primate lateral geniculate nucleus. *Nature*, 356:716–718.

[195] Joseph J Atick and A Norman Redlich. 1992. What Does the Retina Know about Natural Scenes? *Neural Computation*, 4:196–210.

[196] Yang Dan, Joseph J Atick, and R Clay Reid. 1996. Efficient Coding of Natural Scenes in the Lateral Geniculate Nucleus: Experimental Test of a Computational Theory. *The Journal of Neuroscience*, 16(10):3351–3362.

[197] Karl Farrow, Miguel Teixeira, Tamas Szikra, Tim J. Viney, Kamill Balint, Keisuke Yonehara, and Botond Roska. 2013. Ambient illumination toggles a neuronal circuit switch in the retina and visual perception at cone threshold. *Neuron*, 78(2):325–338.

[198] Roska Botond and Werblin Frank. 2003. Rapid global shifts in natural scenes block spiking in specific ganglion cell types. *Nature Neuroscience*, 6(6):600–608.

[199] Nai Wen Tien, James T. Pearson, Charles R. Heller, Jay Demas, and Daniel Kerschensteiner. 2015. Genetically identified suppressed-by-contrast retinal ganglion cells reliably signal self-generated visual stimuli. *Journal of Neuroscience*, 35(30):10815–10820.

[200] Benjamin Sivyer, X Alexander Tomlinson, and X W Rowland Taylor. 2019. Systems/Circuits Simulated Saccadic Stimuli Suppress ON-Type Direction-Selective Retinal Ganglion Cells via Glycinergic Inhibition. *The Journal of Neuroscience*, 39(22):4312–4322.

[201] Tahnbee Kim, Florentina Soto, and Daniel Kerschensteiner. 2015. An excitatory amacrine cell detects object motion and provides feature-selective input to ganglion cells in the mouse retina. *eLife*, 4(MAY).

[202] Christian Puller, Michael B Manookin, Maureen Neitz, and Jay Neitz. 2014. Specialized synaptic pathway for chromatic signals beneath S-cone photoreceptors is common to human, Old and New World primates. *J Opt Soc Am A Opt Image Sci Vis.*, 31(4).

[203] Joanna D. Crook, Beth B. Peterson, Orin S. Packer, Farrel R. Robinson, John B. Troy, and Dennis M. Dacey. 2008. Y-cell receptive field and collicular projection of parasol ganglion cells in macaque monkey retina. *J. Neurosci.*, 28(44):11277–11291.

[204] Ethan A. Benardete and Ehud Kaplan. 1997. The receptive field of the primate P retinal ganglion cell, I: Lineardynamics. *Visual Neuroscience*, 14(1):169–185.

[205] Jennifer M. Ichida, Lars Schwabe, Paul C. Bressloff, and Alessandra Angelucci. 2007. Response facilitation from the "suppressive" receptive field surround of macaque V1 neurons. *Journal of Neurophysiology*, 98(4):2168–2181.

[206] H B Barlow. 1953. Summation and Inhibition in the Frog's Retina. *J. Physiol*, 119(1):69–69.

[207] R. J. Nelson, M. Sur, D. J. Felleman, and J. H. Kaas. 1980. Representations of the body surface in postcentral parietal cortex ofMacaca fascicularis. *The Journal of Comparative Neurology*, 192(4):611–643.

[208] John Allman, Francis Miezin, and Evelynn Mcguinness. 1985. Stimulus specific responses from beyond the classical receptive field: neurophysiological mechanisms for local-global comparisons in visual neurons. *Journal of Neuroscience*, 16(10):3351–3362.

[209] Keiji Tanaka, Kazuo Hikosaka, Hide-Aki Saito, Masao Yukie, Yoshiro Fukada, and Eiichi Lwai. 1986. Analysis of Local and Wide-Field Movements in the Superior Temporal Visual Areas of the Macaque Monkey. *The Journal of Neuroscience*, 6(i):134–144.

[210] Anna Y.M. Wang, Manoj M. Kulkarni, Amanda J. McLaughlin, Jacqueline Gayet, Benjamin E. Smith, Max Hauptschein, Cyrus F. McHugh, Yvette Y. Yao, and Teresa Puthussery. 2023. An ON-type direction-selective ganglion cell in primate retina. *Nature*, 623(7986):381–386.

[211] M. V. Srinivasan, S. B. Laughlin, and A. Dubs. 1982. Predictive coding: a fresh view of inhibition in the retina. *Proc. R. Soc. Lond. B Biol. Sci.*, 216(1205):427–459.

[212] Simon Laughlin. 1981. A simple coding procedure enhances a neuron's information capacity. *Z. Naturforsch. C.*, 36(9-10):910–912.

[213] Matteo Carandini and David Ferster. 1997. A tonic hyperpolarization underlying contrast adaptation in cat visual cortex. *Science*, 276(5314):949–952.

[214] Vijay Balasubramanian, Don Kimber, and Michael J. Berry. 2001. Metabolically efficient information processing. *Neural Comput.*, 13(4):799–815.

[215] Wiktor F. Młynarski and Ann M. Hermundstad. 2018. Adaptive coding for dynamic sensory inference. *Elife*, 7:e32055.

[216] Anthony Zador, William B Levy, and Robert A Baxter. 1996. Energy efficient neural codes. *Neural Computation*, 8:531–543.

[217] Katayun Cohen-Kashi Malina, Muna Jubran, Yonatan Katz, and Ilan Lampl. 2013. Imbalance between excitation and inhibition in the somatosensory cortex produces postadaptation facilitation. *J. Neurosci.*, 33(19):8463–8471.

[218] Solange P. Brown and Richard H. Masland. 2001. Spatial scale and cellular substrate of contrast adaptation by retinal ganglion cells. *Nat. Neurosci.*, 4(1):44–51.

[219] A. M. Derrington, J. Krauskopf, and P. Lennie. 1984. Chromatic mechanisms in lateral geniculate nucleus of macaque. *J. Physiol.*, 357(1):241–265.

[220] F. Rieke. 2001. Temporal contrast adaptation in salamander bipolar cells. *J. Neurosci.*, 21(23):9445–9454.

[221] Hiroko M. Sakai, J. L. Wang, and Ken Ichi Naka. 1995. Contrast gain control in the lower vertebrate retinas. *J. Gen. Physiol.*, 105(6):815–835.

[222] Ian Van Der Linde, Umesh Rajashekar, Alan C. Bovik, and Lawrence K. Cormack. 2009. DOVES: a database of visual eye movements. *Spat. Vis.*, 22(2):161–177.

[223] A M Derrington, P Lenniet, and P Lennie. 1984. Spatial and Temporal Contrast Sensitivities of Neurones in Lateral Geniculate Nucleus of Macaque. *J. Phyiol*, 357:219–240.

[224] Lauren E. Wool, Joanna D. Crook, John B. Troy, Orin S. Packer, Qasim Zaidi, and Dennis M. Dacey. 2018. Nonselective wiring accounts for Red-Green opponency in midget ganglion cells of the primate retina. *J. Neurosci.*, 38(6):1520–1540.

[225] Keith Rayner. 1998. Eye movements in reading and information processing: 20 years of research. *Psychol. Bull.*, 124(3):372–422.

[226] B. J. Frost, D. R. Wylie, and Y. C. Wang. 1990. The processing of object and self-motion in the tectofugal and accessory optic pathways of birds. *Vis. Res.*, 30(11):1677–1688.

[227] J. Y. Lettvin, H. R. Maturana, H. R. Maturana, W. S. Mcculloch, and W. H. Pitts. 1959. What the frog's eye tells the frog's brain. *Proc. IRE*, 47(11):1940–1951.

[228] William C. Kwan, Inaki Carril Mundinano, Mitchell J. de Souza, Sammy C.S. Lee, Paul R. Martin, Ulrike Grünert, and James A. Bourne. 2018. Unravelling the subcortical and retinal circuitry of the primate inferior pulvinar. *J. Comp. Neurol.*, 527(3):558–576.

[229] Susana Martinez-Conde, Stephen L. Macknik, and David H. Hubel. 2004. The role of fixational eye movements in visual perception. *Nat. Rev. Neurosci.*, 5(3):229–240.

[230] Alexander C. Schütz, Doris I. Braun, Dirk Kerzel, and Karl R. Gegenfurtner. 2008. Improved visual sensitivity during smooth pursuit eye movements. *Nat. Neurosci.*, 11(10):1211–1216.

[231] Susana Martinez-Conde, Stephen L. Macknik, and David H. Hubel. 2000. Microsaccadic eye movements and firing of single cells in the striate cortex of macaque monkeys. *Nat. Neurosci.*, 3(3):251–258.

[232] Susana Martinez-Conde, Stephen L. Macknik, Xoana G. Troncoso, and Thomas A. Dyar. 2006. Microsaccades counteract visual fading during fixation. *Neuron*, 49(2):297–305.

[233] Deborah Langrill Beaudoin, Michael B. Manookin, and Jonathan B. Demb. 2008. Distinct expressions of contrast gain control in parallel synaptic pathways converging on a retinal ganglion cell. *J. Physiol.*, 586(22):5487–5502.

[234] Peter H. Schiller. 2010. Parallel information processing channels created in the retina.

[235] Stephen G. Lisberger. 2010. Visual guidance of smooth-pursuit eye movements: Sensation, action, and what happens in between.

[236] Lappe Markus, Bremmer Frank, and van den Berg AV. 1999. Perception of self-motion from visual flow. *Trends in Cognitive Sciences*, 3(9):329–336.

[237] Karl S Muller, Jonathan Matthis, Kathryn Bonnen, Lawrence K Cormack, Alex C Huk, and Mary Hayhoe. 2023. Retinal motion statistics during natural locomotion. 12:82410.

[238] R A Barton. 1998. Visual specialization and brain evolution in primates. *Proc. R. Soc. Lond.*, 265:1933–1937.

[239] Jon H. Kaas. 2013. The evolution of brains from early mammals to humans.